FORSVARSBYGG
Vi bygger forsvarsevne hver dag

NTNU
Norwegian University of Science and Technology

LWAG 2026

Extended Abstracts

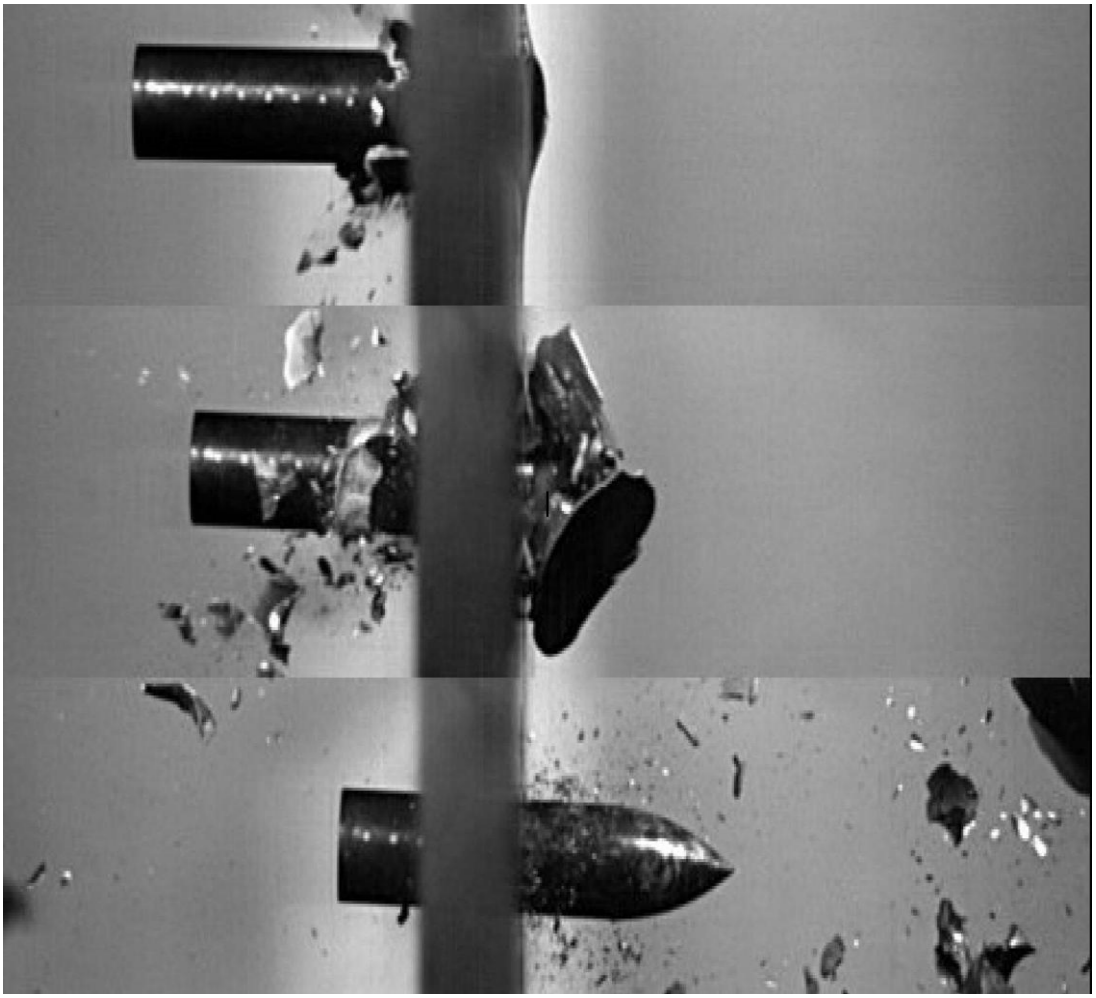

Light-Weight Armour for Defence & Security
LWAG 2026

Influence of Under-Vest Fabric Type on Back-Face Deflection

Ana Azevedo[a]*, Angel Miranda-Vicario[a], Frederik Coghe[a]

[a] *Department of Weapon Systems & Ballistics, Royal Military Academy, Brussels, Belgium*

Abstract

Soft ballistic vests are typically worn over regular clothing, yet the influence of under-vest fabrics on Behind-Armour Blunt Trauma (BABT) remains insufficiently characterized. This study investigates how different under-vest fabrics affect back-face deflection in a modelling clay backing under 12-gauge shotgun projectile. Four fabrics representative of under-vest garments were evaluated: 100% Dyneema with a fibre diameter of 0.2 mm (Fabric 1), a Dyneema (90%)–Elasthan (10%) blend with a fibre diameter of 0.25 mm (Fabric 2), an aramid fabric with 52% aramid fibres and a fibre diameter of 0.3 mm (Fabric 3), and an aramid fabric with 49% aramid fibres and a fibre diameter of 0.4 mm (Fabric 4). Each fabric was placed between a soft ballistic vest (Dyneema material) and a Roma Plastilina modelling clay used as a soft-tissue surrogate. Back-face deflection in the clay was measured after 12-gauge impacts under controlled laboratory conditions and compared across fabric types. A baseline series without any under-vest fabric (vest only) was also performed. Across all impacts, maximum back-face deflection ranged from about 57 mm to 65 mm, with the vest-only baseline exhibiting the largest deflection and the aramid fabrics (Fabrics 3 and 4) showing a modest reduction in clay deformation relative to the Dyneema-based fabrics and to the baseline. The results demonstrate measurable differences in back-face deflection as a function of under vest fabric type, even when the ballistic vest remains unchanged. Rather than prescribing specific clothing configurations, this study aims to provide quantitative data that can support informed decisions by end users, procurement agencies regarding under vest garment selection and test conditions.

Introduction

Body armour serves as a critical component of personal protection for military and law enforcement personnel, designed to mitigate ballistic threats and reduce fatal injuries in combat and high-risk operations. Modern body armour systems primarily consist of soft armour (made from high-performance fibres such as polyaramid and ultra-high-molecular-weight polyethylene) and hard armour (ceramic, steel or composite plates). Standardized testing procedures, such as those defined by the National Institute of Justice (NIJ) [1] and the STANAG 2920 standard [2], provide a controlled framework for evaluating the ballistic resistance of protective vests. These protocols typically measure factors like penetration resistance and backface deformation (BFD) using specific ammunition types and impact conditions. While these tests ensure a baseline level of protection, they often do not fully replicate the dynamic conditions experienced in operational environments. Real-world use of body armour introduces numerous variables, including environmental exposure, multi-hit scenarios, user movement, and the presence of everyday objects carried under the vest. These factors may significantly alter the actual performance of armour in ways that are not currently captured by standardized laboratory assessments. Several studies have highlighted that body armour performance is influenced by factors such as temperature, humidity, and mechanical wear over time [3], [4], [5].

Soft ballistic vests are routinely worn over everyday garments, yet most ballistic blunt trauma assessments are performed under simplified laboratory configurations that do not explicitly consider the effect of intermediate clothing layers on measured back-face deformation. In standards-based body armour evaluation, Roma Plastilina No. 1 [1] is commonly used as a ballistic witness material, and the residual indentation in the clay is treated as a

* Corresponding author. Tel.: +3224414131
E-mail address: ana.ferreira@mil.be

backface signature related to energy transfer through the armour system. The mechanical response of this backing system is known to depend not only on the armour package itself but also on the backing material condition, including temperature sensitivity and work-history effects of the clay. This broader sensitivity motivates the present study, which examines whether an under-vest textile layer placed between a soft ballistic vest and the clay backing can measurably alter the resulting deformation pattern under impact. The objective of this work is to quantify the influence of four representative under-vest fabrics on back-face deflection under 12-gauge shotgun projectile impact. Rather than prescribing a specific garment solution, the study aim to provide experimental evidence that can inform both end-user clothing selection and the interpretation of ballistic test outcomes when intermediate textile layers are present.

Experimental setup

An experimental campaign was conducted using a soft ballistic vest composed of Ultra-high-molecular-weight polyethylene (UHMWPE) material impacted by 12-gauge shotgun projectiles under controlled laboratory conditions. All the experimental ballistic tests were carried out in the firing range of the Department of Weapon Systems and Ballistics at the Royal Military Academy (Belgium). A Roma Plastilina No. 1 modelling clay backing was employed as a soft-tissue surrogate in accordance with established ballistic testing practices, where the permanent indentation left in the clay is used to characterize back-face signature. Figure 1 shows the experimental setup.

Figure 1 – Experimental setup used to evaluate the influence of under-vest fabric type on back-face deflection in a soft ballistic vest system.

Five configurations were investigated. Four included an under-vest fabric inserted between the vest and the clay backing, while one baseline configuration consisted of the vest only with no intermediate layer. The fabrics were selected to represent plausible under-vest garment types with differing fibre composition and fibre diameter:

- Fabric 1: 100% Dyneema, fibre diameter 0.2 mm.
- Fabric 2: 90% Dyneema and 10% elastane, fibre diameter 0.25 mm.
- Fabric 3: aramid-based fabric containing 52% aramid fibres, fibre diameter 0.3 mm.
- Fabric 4: aramid-based fabric containing 49% aramid fibres, fibre diameter 0.4 mm.

After impact, the maximum back-face deflection in the clay was measured for each shot and compared across the five configurations. *Figure 2* shows the experimental setup for the body armour vest wit the fabric against the witness material.

a) b) c)

Figure 2 - Experimental tests for different fabrics: a) body armour vest with the fabric against the witness material; b) complete set after the impact; c) BFS results on the witness material after the test

Results and Discussion

Across all tested configurations (see Figure 3), the maximum back-face deflection ranged from about 57 mm to 65 mm. The vest-only baseline produced the largest deformation (first column), indicating that the absence of an intermediate textile layer led to the highest measured indentation in the clay under the present impact conditions. The introduction of an under-vest fabric produced measurable changes in deformation depth. The aramid-based fabrics, Fabrics 3 and 4 (last 2 column), showed a modest reduction in back-face deflection relative to both the vest-only baseline and the Dyneema-based underlayers. By contrast, the Dyneema-rich fabrics, Fabrics 1 and 2 (2nd and 3rd columns), provided either a smaller reduction or only limited improvement relative to the baseline condition.

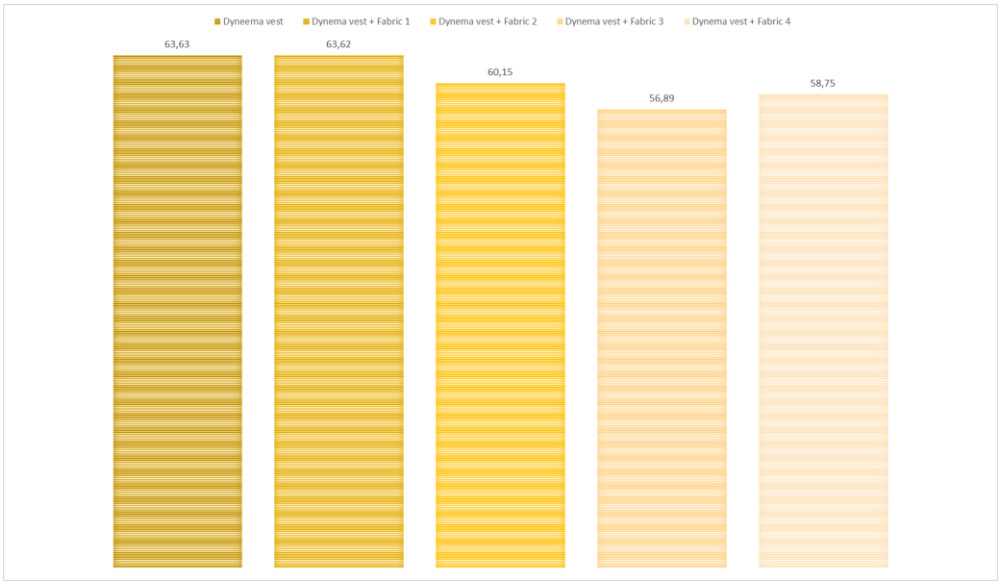

Figure 3: Maximum BFS as a function of th body armour with the different fabrics

These observations suggest that the under-vest layer is not mechanically neutral. Even though the ballistic vest remained unchanged, changing the textile immediately behind the vest altered the final clay indentation. This is consistent with the general understanding that back-face signature depends on the coupled response of armour, interfaces, and backing support rather than on the armour panel alone. A plausible explanation is that the fabrics differ in compressibility, local stiffness, frictional behaviour, and their ability to spread load over a wider area before the deformation is transmitted into the clay. Aramid-based fabrics may have promoted a more favourable redistribution of contact pressure at the vest–fabric–clay interface, thereby reducing peak indentation. In contrast, the more compliant or more elastic Dyneema-based underlayers may have allowed a greater localized deformation before significant load redistribution occurred. The magnitude of the observed reduction remained moderate, so the findings should be interpreted carefully. Nevertheless, the differences are large enough to indicate that clothing configuration can influence comparative outcomes, especially in tests where performance margins are small. From a practical perspective, the results support two implications. First, end users and procurement agencies should recognize that under-vest garments can influence blunt-trauma-related response even when ballistic penetration

resistance is unchanged. Second, researchers and test laboratories should consider whether the absence or presence of an intermediate textile layer may affect the realism and reproducibility of BABT-oriented assessments, particularly when comparing systems intended for operational wear.

Conclusion

This study shows that under-vest fabric type can measurably influence back-face deflection in a Roma Plastilina No.1 clay backing during 12-gauge impact on a soft ballistic vest. Within the tested set of materials, the aramid-based fabrics yielded the lowest deformation levels, while the vest-only baseline produced the highest deflection. The effect observed is modest but consistent with the view that behind-armour blunt trauma metrics are governed by the response of the full vest–interlayer–backing system rather than by the armour panel in isolation.

References

[1] National Institute of Justice, “NIJ Standard-0101.04 Ballistic Resistance of Body Armor,” Law Enforcement Standards Laboratory of the National Bureau of Standards, Sep. 2000, Accessed: Sep. 20, 2017. [Online]. Available: http://www.aashield.com/nij-standard-0101-06-ballistic-resistance-of-body- armor/
[2] NATO Standardization Agency, “STANAG 2920 - Ballistic test method for personal armour materials and combat clothing,” North Atlantic Treaty Organization (NATO), Jul. 2003.
[3] M. Wilhelm and C. Bir, “Injuries to law enforcement officers: The backface signature injury,” Forensic Science International, vol. 174, no. 1, pp. 6–11, Jan. 2008, doi: 10.1016/j.forsciint.2007.02.028.
[4] K. A. Rafaels et al., “Injuries of the head from backface deformation of ballistic protective helmets under ballistic impact,” Journal of Forensic Sciences, vol. 60, no. 1, pp. 219–225, Jan. 2015, doi: 10.1111/1556-4029.12570.
[5] Y. K. Wen, H. Zheng, J. B. Zhang, W. M. Yan, G. Y. Cui, and C. Xu, “Analysis of dynamic back face deformation of a body armor impact by a rifle bullet using 3D-DIC,” J. Phys.: Conf. Ser., vol. 1507, no. 3, p. 032051, Mar. 2020, doi: 10.1088/1742-6596/1507/3/032051.

Light-Weight Armour for Defence & Security
LWAG 2026

Application of the SHIELD-FEM thorax model for assessing thoracic protective equipment in blast scenarios

Boutillier Johanna[a]*, De Mezzo Sébastien[a], Gardère Pierre[a], Hengy Sébastien[a]

[a] *French-German Research Institute of Saint-Louis, 5 rue du Général Cassagnou, BP 70034, 68301 Saint Louis CEDEX, France*

Abstract

When designing protective equipment for soldiers and law enforcement officers, blast threats are rarely considered, with development efforts primarily focused on protection against ballistic impacts, knives, and fragments. However, primary blast injuries predominantly affect air-filled organs such as the lungs and gastrointestinal tract, and previous studies have shown that certain thoracic protective equipment (TPE) may actually exacerbate injury severity under blast loading, although findings are inconsistent.

In this study, a finite element model (FEM) of the human torso, SHIELD-FEM for "Simplified Human thorax for Injury EvaLuation in Defense – Finite Element Model", is employed to investigate thoracic response to blast exposure. The model has been previously validated under impact tests using non-lethal projectile impacts. The first objective was to validate the FEM under blast loading using data from a dummy called SurHUByx exposed to various blast intensities, with and without a soft body armor vest. Replications of those scenarios were performed on SHIED-FEM.

A parametric study is then conducted to evaluate the influence of pads rigidity and vest tightness on thoracic wall kinematics and internal organ pressures. The results provide insight into the mechanisms by which soft body armor may alter blast transmission to the thorax and contribute to injury risk.

I. INTRODUCTION

The rapid progress of computer-science techniques has made high-fidelity numerical methods, most notably finite-element (FE) modelling, central to the analysis of complex biomechanical phenomena. Computational simulations complement and, in many cases, surpass experimental approaches that are limited by high cost, limited accessibility, and ethical constraints. Consequently, numerical tools have become indispensable for investigating injuries that are difficult to replicate experimentally, such as ballistic and blast loading of the thorax and abdomen.

Over the past two decades, numerous numerical models of the thorax and abdomen have been developed, with varying complexity based on their intended applications and computational capabilities. Most FE models focus on automotive engineering, examining thoracic forces and deflection under various loading scenarios. Early work addressing blast-induced injuries have been explored by Stuhmiller [1999] and subsequent advancements by Przekwas [2014], who documented diverse models of varying detail for thoracic and brain injuries. More recent efforts include Tan et al.'s articulated human body model [2012a, 2012b], which simulates kinematic and brain responses to blasts, and Kannan et al.'s [2012] high-fidelity 2D and 3D simulations for precise prediction of organ injuries like brain and lung trauma, integrating non-invasive methods to assess injury severity. Chaufer et al. [2024] proposed an overview of physical and numerical surrogates developed specifically for blunt ballistic impacts, with a focus on their ability to accurately represent the human body in the context of blunt ballistic impact. In parallel,

* Corresponding author. Tel.: +33 89 69 51 97
E-mail address: johanna.boutillier@isl.eu

animal studies involving sheep, rats, and pigs have yielded valuable insight into blast pathology [Sundaramurthy et al., 2012; Zhu et al., 2010, 2012].

Blast waves pose unique modelling challenges. Their extreme velocities and steep pressure gradients generate severe mesh distortion and nonlinear material responses, making blast loading considerably more demanding than conventional automotive impact simulations.

Despite the growing body of knowledge on blast physics, the protective performance of personal protective equipment (PPE) against thoracic blast injury remains poorly understood. Some investigations report that low-impedance thoracic protective equipment (TPE) can aggravate blast-induced damage [Phillips et al., 1988; Cooper et al., 1991, 1996; Gibson, 1994; Prat et al., 2019], while others find no detrimental effect (Long et al., 2009; Wood et al., 2013). Incorporating high-density materials like ceramic plates may help reduce lung injuries and mortality rates [Cooper et al., 1991, 1996; Sekine et al., 2021].

To address these gaps, the present work seeks to enhance the evaluation and effectiveness of blast protection systems through advanced numerical modeling and injury risk assessment. This includes the numerical replication of blast scenarios involving protective vests, with a focus on accurately modeling full vest configurations and integrating them into the SHIELD-FEM (Simplified Human thorax for Injury EvaLuation in Defense – Finite Element Model). Simulations will replicate SurHubyx-based scenarios for comparative metric analysis [Gardere et al., 2026]. The study will investigate potential amplification of blast effects behind protective vest relative to unprotected cases, and assess the biomechanical influence of air gaps between the vest and thorax and evaluate the influence of pads rigidity.

II. MATERIALS AND METHODS

2.1. SHIELD-FEM presentation

To address the unique variations in thorax geometry and material properties among individuals due to factors such as sex, age, and health, a standardized model representing an average male (50th percentile) has been developed. The SHIELD-FEM (Simplified Human thorax for Injury EvaLuation in Defense – Finite Element Model) is designed to serve as a producible mannequin with materials commonly used in laboratory settings, ensuring its global response aligns with existing data on Post-Mortem Human Surrogates (PMHS) or other validated dummies.

The SHIED-FEM thorax model is a simplified finite element version of the biofidelic thoracic FE model THUMBS, representing a 50th percentile human thorax. The SHIELD-FEM thorax model simplifies and optimizes the complex anatomy to facilitate use and analysis in our studies, as illustrated in Figure 1.

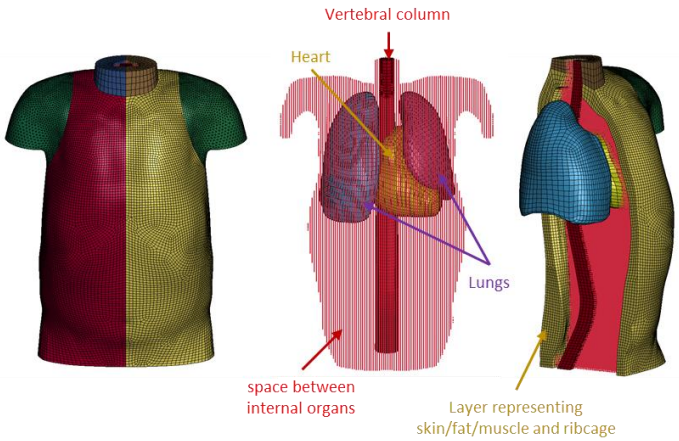

Figure 1: Simplified thorax FEM of a 50th percentile male, called SHIELD-FEM “Simplified Human thorax for Injury EvaLuation in Defense – Finite Element Model”

Key features of the SHIELD-FEM include:

- Simplified Anatomy: The skin, fat, muscle, and ribcage are represented as a single membrane layer approximately 2 to 3 cm in width, a simplification previously used in other studies on blunt impact and blast loading [Ouellet et al., 2008; Magnan et al., 2011; Boutillier et al., 2020].
- Organs of Interest: The model focuses on the lungs and heart, with a simplified CAD (Computer-Aided Design) of the thorax imported into LS-DYNA to generate a hexahedral mesh.

- Mesh Quality: To ensure high-quality numerical responses, the model primarily uses 8-node brick elements for solid parts, with tetrahedral elements for the shoulder and SPH (Smooth Particles Hydrodynamics) method for complex spaces between internal organs. The model comprises 148,018 solid elements and 241,791 SPH nodes, with a mesh size of approximately 8 mm. The inter-particle distance was set to a minimum of half the size of the hexahedral elements, with a selected value of 0.3 mm. This choice ensured an adequate number of particles between the muscle and organ layers, facilitating accurate simulation of interactions within these regions.

The constitutive laws and material parameters used for each anatomical part of SHIELD-FEM are summarized in Table 1. In our FEM, two types of contact definitions are employed to model interactions between different anatomical parts:

- Two *Contact_Automatic_nodes_to_surface are used for the interface between: (1) mediatinum and muscle; and (2) mediastinum, internal organs and spinal column. This definition uses a soft constraint approach (SOFT=1) with a scaling factor (SOFSCL = 0.1) and considers both sliding and friction (SBOPT = 2). Very low stiffness values (SFSA = SFSB = 1e-9) ensure that SOFT=1 is selected.
- *Contact_Single_surface is applied for internal contacts within internal organs and the spinal column. This definition employs a penalty formulation (SOFT=2) with a unit stiffness (SFSA = SFSB = 1) and includes sliding and friction considerations (SBOPT = 2). The scaling factor is set to SOFSCL = 0.1.

Table 1: Material parameters used in SHIELD-FEM

Tissues	External membrane layer	Internal organs	Mediastinum	Spinal column
Manufacturable material	PMC 770	SEBS 30/70	SEBS 20/80	ABS
Material model	simplified rubber foam *MAT_181	simplified rubber foam *MAT_181	Elastic *MAT_001	Elastic
Density (kg/m^3)	1040	880	1000	1330
Young's modulus (MPa)	-	-	10	2900
Poisson's ratio (-)	0,495	0,495	0,45	0,42
Stress-strain	time-dependant	time-dependant	-	-
Unloading phase	HU = 0,8 Shape = 8	HU = 1 Shape = 0	-	-
Remark	Optimized with LS-OPT	Optimized with LS-OPT	From chaufer et al. 2023	From datasheet

These contact definitions help capture the complex interactions within the thorax, ensuring accurate simulation of deformations and stresses under various loading conditions.

2.2. Blast wave generation

The Prescribed Inflow ALE (PIF-ALE) method generates a blast wave by imposing prescribed pressure histories on a thin “ambient layer” of ALE air mesh, eliminating the need to model an explosive charge. The user defines two time-history curves for this layer:

- Volume change – kept constant (relative volume = 1).
- Internal energy per unit reference volume change obtained from the ideal-gas relation

$$E(t) = \frac{P_{LOC}(t)}{\gamma - 1}$$

Where $P_{LOC}(t) = P_{atm} + P_{INC}(t)$. The incident overpressure P_{INC} is here obtained from experimental data.

A previous study already compare LS-DYNA methods to generate a blast wave with validation regarding experimental data [Boutillier et al., 2017]. The LBE, MM-ALE and ALE-LBE methods were evaluated and results shows better agreement using the MM-ALE approach despite a higher computational calculation time. This was because LBE estimation through ConWep program was not accurate regarding data from our experimental campaign with C-4 explosive charge. Nevertheless, the PIF-ALE method has the advantage that the user defines the desire pressure profile, limiting the errors with experimental measurement. For that reason, and because this approach reduces computational cost, it was chosen for the interaction with SHIELD-FEM.

Because the blast attenuates while passing from the ambient layer into the main air domain. Hence, when using the PIF-ALE method, the blast wave overpressure needs to be adjust. This can be achieved by scaling the internal energy per unit reference volume curves with a factor derived from the predicted pressure loss and or the one for the positive phase duration. For some cases, pre-treatment on the pressure-profile exponential decay should be applied. All these iteration to get the correct threat at the location of the thorax FEM can be time-consuming depending on the initial threat.

2.3. Scenarios

Tested configurations were taken for scenarios performed on SurHUByx dymmy [Gardère et al., 2026]. Four scenarios were reproduced on SHIELD-FEM. Blast wave characteristics (red circles) are illustrated in Figure 2, together with the Bowen curves (standing position). The smallest explosive charge corresponds to a scenarios slightly below the lung injury threshold, while the largest explosive charge simulated is closest to the 1% lethality curve according to Bowen.

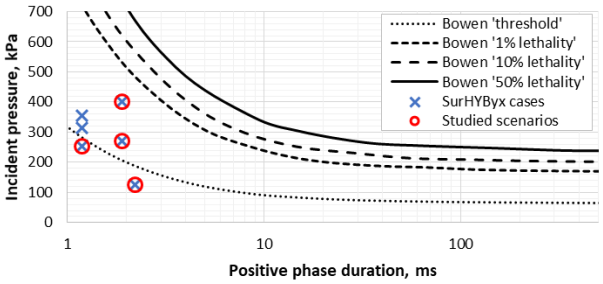

Figure 2: Characteristics (Incident overpressure, duration) of the SurHUByx cases and the studied scenarios, together with the Bowen curves

III. RESULTS AND DISCUSSIONS

Filtering was applied on both experimental and numerical signals. The pressure signals were filtered using a sixth-order Bessel filter, with a cut-off frequency of 10 kHz. The same filter with a cut-off frequency of 40 kHz was applied on the acceleration signals.

3.1. Replication of bare scenarios

A comparison is made between the physical SurHUByx response and the SHIELD-FEM response, even in the absence of proof regarding the validity of SurHUByx with regard to blast loading. The results were evaluated based on two key metrics: peak pressure in the internal organs of the human body and chest motion. During the course of the experiments, SurHUByx was equipped with a hydrophone that was inserted by the back in the right lung (~4 cm), enabling a comparison to be made on this organ, in addition to the chest motion.

The numerical blast incident characteristics for each scenario were comparable with the experimental data measured with a pencil probe near the unprotected mannequin. The pressure profile has been calculated numerically using LS-DYNA, and the results show that the incident overpressure and positive phase duration are both correct (with an error of less than 7%). However, due to less pronounced exponential decay, the incident impulse is slightly overestimated, with errors of 20-25%.

When the shock wave interacts with the thorax FEM, it then propagates within the biomechanics model, and peak static pressure was calculated inside the lungs and heart. The results of overpressure in the right lung resulted from the wave propagation is presented in Figure 3 (Right), while the sternum acceleration and velocity are illustrated in Figure 3, Left and Middle, respectively. A comparison with SurHUByx dummy response is shown in this Figure. The baseline thorax model reproduces chest kinematics reasonably well.

The results nevertheless revealed discrepancies between the two models, especially for the pressure measurement. For information, numerical pressure into organs was measured by taking the mean value of several adjacent elements, corresponding approximately to the size of the physical sensor. Firstly, the exact position of the sensor was estimated rather than obtained through imaging, introducing uncertainty into the measurements. Even a small deviation of 1 cm in sensor placement could either improve or worsen the correlation with data from the SurHUByx biofidelic dummy. This underscores the need for precise sensor positioning in future studies. Secondly,

no negative phase was observed on the FEM organ pressure. The reason is that the *MAT_SIMPLIFIED_RUBBER model is not well suited to handle significant tensions or negative pressures. For applications where these aspects are critical, it is recommended to use a more advanced material model such as Mooney-Rivlin (*MAT_077), Viscoelastic (*MAT_VISCOELASTIC), or Ogden (*MAT_077). The influence of mesh size should also be investigated. For the current FEM, the mesh size is around 8mm.

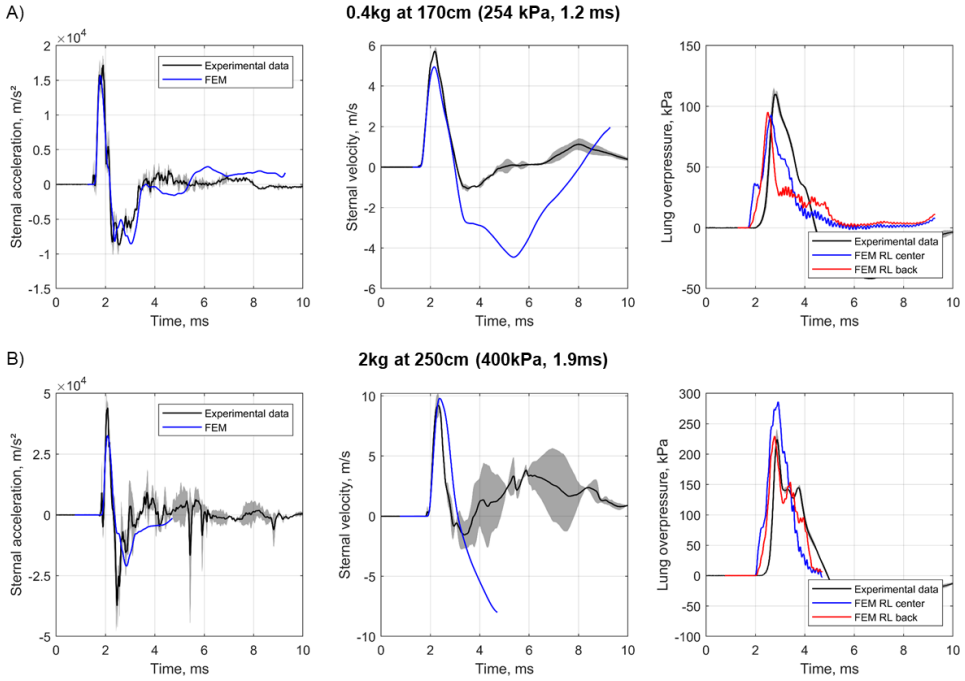

Figure 3: SHIELD-FEM response to blast loading and comparison with data from the SurHUByx physical dummy. Left) Chest acceleration; Middle) Chest velocity and Right) Lung overpressure; (A) Scenario 0.4 kg at 170 cm; (B) Scenario 2 kg at 250 cm.

3.2. Simplified soft ballistic vest: influence of air gap

The first modelling step considered only the soft ballistic pack (SBP, 8 mm thick) obtained by extruding the external torso geometry. Three finite-element models were generated, each incorporating a different air gap between the chest wall and the SBP (see Fig. 4). It enables investigating how the inter-space air gap modulates stress distribution and energy absorption in the vest under realistic blast conditions. The constitutive behaviour of the SBP was described using the material law derived from Gardère et al. [2025].

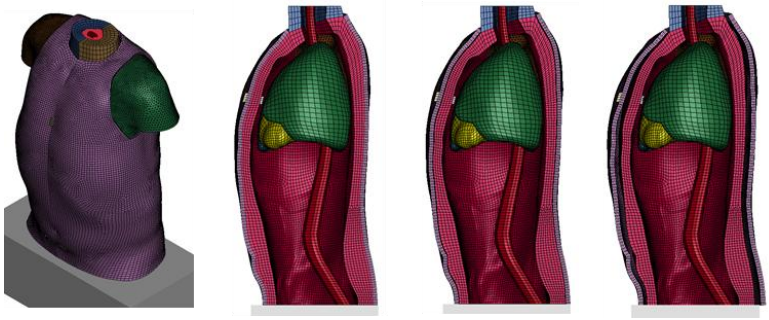

Figure 4: First version of the SBP FE model. From left to right: vest on SHIELD-FEM, vest with no air-gap, vest with a small air-gap and finally vest with a 15mm air-gap.

To evaluate the protective performance, a blast loading was reproduced by detonating a 400 g charge at a standoff distance of 170 cm, producing a peak over-pressure of 254 kPa with a duration of 1.2 ms.

Simulations reveal a clear balance associated with the inter-space air gap as illustrated in Fig. 5. With no gap or a very thin gap (1–2 mm), the chest kinematics (displacement and velocity) are similar, indicating that the torso moves almost as if the vest were rigidly attached. However, under these conditions the vest itself exhibits poor correlation with the experimental data (vest acceleration and velocity). Introducing an air gap progressively mitigates this issue;

a gap of 15 mm yields the most favorable vest response, even if the correlation with the experimental data is not yet acceptable. Chest acceleration for a large air-gap rises by ≈ 461 % compared with the no-gap case, while chest velocity rises by 748%, nevertheless, error with experimental data are around 75% for the former and 43% for the latte metric. This slight improvement in the vest motion response led to a slight degradation of the chest acceleration.

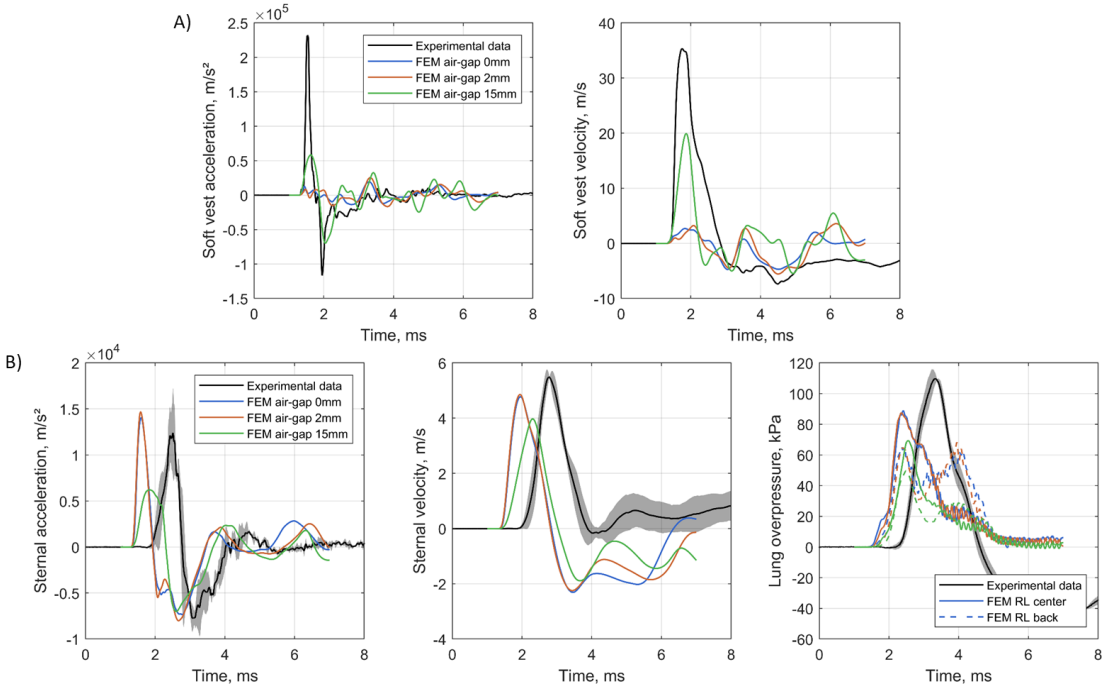

Figure 5: SHIELD-FEM response to blast loading and comparison with data from the SurHUByx physical dummy (Scenario 0.4 kg at 170 cm). Influence of air-gap on model response. A) Vest response; B Chest response: Left) Chest acceleration; Middle) Chest velocity and Right) Lung overpressure.

These findings indicate that representing the soft-ballistic vest solely by the soft-ballistic pack is inadequate for capturing the coupled vest-torso dynamics.

3.3. Replication of blast scenario with a more realistic vest

Building on the first model, the second finite-element representation retains the 8 mm soft-ballistic pack (SBP) and adds foam pads positioned between the torso and the SBP. The pads are made of NRB foam fabricated from an acrylonitrile copolymer, and are arranged to cover the anterior chest and back area. The pads were arranged in the same manner than the soft ballistic vest tested experimentally (Fig 6). Air-gap between pads on the torso front face and the torso external shape was below 2mm.

For the initial material description, the foam is assigned the generic isotropic elastic-plastic constitutive model Mat_012 under LS-DYNA, which captures its initial linear elasticity, yielding, and subsequent hardening behavior. Hereafter are the parameters used for the “standard” version of the pads: Rho = 130 kg/m^3; v = 0.38; G = 0.87 MPa; K = 3.33 MPa; $\sigma\gamma$ = 160 kPa ; E_{TAN} = 60 kPa.

Figure 6: Second version of the SBP FE model with the insertion of pads (blue part on the left image).

The two refined vest models (MEF-v1 (15 mm air gap) and MEF-v2 (foam-pad configuration)) were subjected to the identical blast loading (400 g charge, 170 cm standoff). The comparison highlights three key performance metrics (Fig 7):

- Lung pressure appears insensitive to the presence of pads, indicating that neither the 15 mm air gap nor the foam-pad insertions substantially alter the pressure wave transmitted to the thoracic cavity.
- Chest motion shows a slightly higher discrepancy when foam pads are introduced: the peak chest velocity drops by 17 % (4.8 to 4.0 m/s¹) and the associated acceleration is reduced by about 45 % (11 370 to 6 215 m/s²). These values remain below the experimentally measured chest acceleration and velocity (17 200 m/s² and 5.7 m/s);
- Vest acceleration decreases by 9 % and velocity by 36 % when comparing MEF-v2 with MEF-v1. Nevertheless, the simulated vest dynamics are still far lower than the experimental peak values.

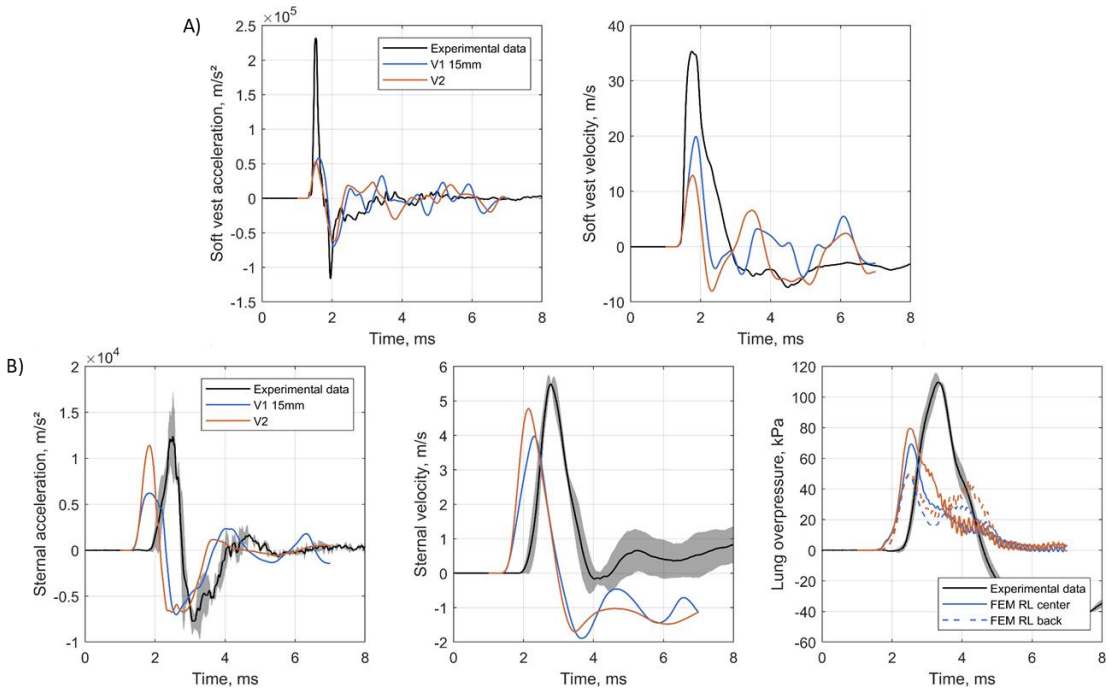

Figure 7: SHIELD-FEM response to blast loading and comparison with data from the SurHUByx physical dummy (Scenario 0.4 kg at 170 cm). Comparison of two refined vest models (MEF-v1 (15 mm air gap) and MEF-v2 (foam-pad configuration)). A) Vest response; B Chest response: Left) Chest acceleration; Middle) Chest velocity and Right) Lung overpressure.

To assess whether the mechanical properties of the inserts could further improve the agreement with experimental data, three material configurations were explored for the foam pads positioned between the torso and the soft-ballistic pack (Fig 8):

- Standard – the baseline set of parameters previously employed.
- Softer – a reduced elastic modulus and lower yield stress, representing a more compliant acrylonitrile-copolymer foam.
- Stiffer – an increased modulus and higher yield stress, simulating a denser, less compressible foam.

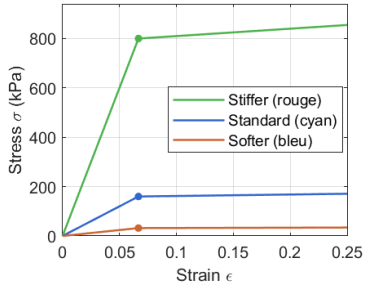

Figure 8: Stress-Strain curve for the three set of material parameters used for the vest pad inserts.

All three configurations were subjected to the same blast loading (400 g charge at 170 cm, generating a peak over-pressure of 254 kPa with a duration of 1.2 ms). Contrary to expectations, the variations in pad stiffness produced no discernible effect on either the chest kinematics (velocity and acceleration) or the vest-segment response (peak acceleration and velocity), as illustrated in Fig 9. Moreover, the simulated lung pressure remained unchanged across the three material sets.

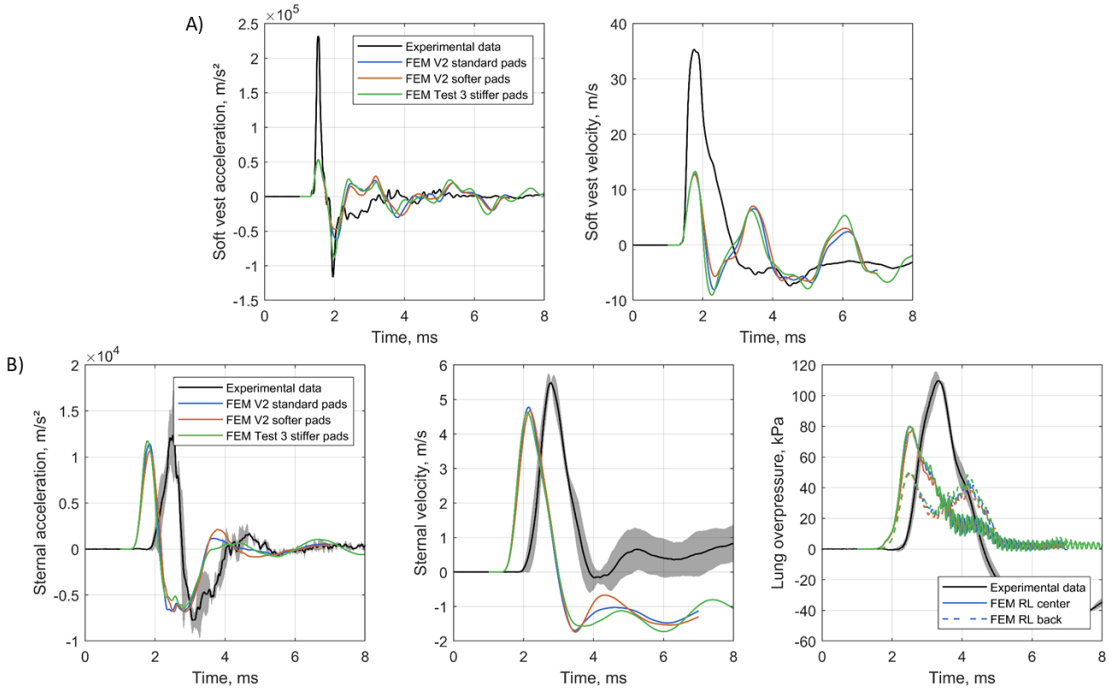

Figure 9: SHIELD-FEM response to blast loading and comparison with data from the SurHUByx physical dummy (Scenario 0.4 kg at 170 cm). Influence of pads material parameters. A) Vest response; B Chest response: Left) Chest acceleration; Middle) Chest velocity and Right) Lung overpressure.

Despite this parametric study, the finite-element predictions still underestimate the experimental response for the vest dynamics. These results indicate that, within the current modeling framework, the stiffness of the foam pads is not the dominant factor governing the mismatch. Additional aspects, such as more accurate representation of the vest's shape, improved contact definition, or improved constitutive laws for the soft-ballistic pack, must be addressed to achieve a reliable correlation with the experimental blast response.

IV. CONCLUSION

In summary, FE model reproduces the incident blast overpressure and positive-phase duration with an error below 7 %, confirming a good replication of the pressure that reaches the mannequin.

Although the chest kinematics are captured reasonably well in the bare configuration, some discrepancies remain in the predicted lung-pressure response, indicating that further refinements are required.

Introducing an air gap between the chest and the 8 mm soft-ballistic pack revealed a clear tendency: a 15 mm gap improved vest acceleration and velocity (bringing them closer to experimental values, but still far from it). Adding NRB foam pads does not affect lung pressure, yet the predicted vest dynamics remained far below measured peaks, and variations in pad stiffness produced no discernible effect. These findings demonstrate that representing the vest solely by the soft-ballistic pack or by simple foam inserts is insufficient; future work must focus on more accurate vest geometry, refined contact algorithms, and advanced constitutive models for the ballistic fabric to achieve a reliable correlation with experimental blast responses.

V. REFERENCES

[1] Boutillier J. Contribution à la compréhension et à la modélisation des effets lésionnels sur le thorax des ondes de choc aériennes. Thèse de doctorat, université de Strasbourg, Janvier 2017

[2] Boutillier J., De Mezzo S., Heck S., Boehrer Y., et al. (2020). Protection of the soldier against the blast threat: experimental & numerical development of a torso surrogate. ISL report R-04/17/01/888/2/00-01/CT-270/2020

[3] Chaufer M., Delille R., Bourel B., Maréchal C., Lauro F., Mauzac O. and Roth S. (2024). Review of non-penetrating ballistic testing techniques for protection assessment: From biological data to numerical and physical surrogates. Proc Mech E Part H: J Engineering in Medicine 00(0).
[4] Cooper, G.J., Townend, D.J., Cater, S.R., and Pearce, B.P., 1991. The Role of Stress Waves in Thoracic Visceral Injury from Blast Loading: Modification of Stress Transmission by Foams and High-Density Materials. J. Biomech, 24 (5), 273–285.
[5] Cooper, G.J., 1996. Protection of the Lung from Blast Overpressure by Thoracic Stress Wave Decouplers. J. Trauma, 40 (3): S105–S110.
[6] Gardère, P., De Mezzo, S., Boutillier, J., et al. 2025. On the modeling of a soft protection under shock tube test. Proceeding of the 27th International Symposium on Military Aspects of Blast and Shock MABS27, France, 2025
[7] Gardère, P., De Mezzo, S., Boutillier, J., et al. 2025. Flexible protection and blast injury: experimental and numerical study using biofidelic thorax dummy. Proceeding of the Light-Weight Armour for Defence & Security LWAG 2026, Norway, 2026
[8] Gibson, P.W., 1994. Amplification of Air Shock Waves by Textile Materials. J. Text Inst., 86 (1): 119–128.
[9] Kannan R, Prezekwas A.J. (2012). A near-infrared spectroscopy computational model for cerebral hemodynamics. International Journal for Numerical Methods in Biomedical Engineering; 28(11):1093–1106.
[10] Long, J.B. Bentley, T.L. Wessner, K.A. Cerone, C. Sweeney, S. and Bauman, R.A., 2009. Blast Overpressure in Rats: Recreating a Battlefield Injury in the Laboratory. J. Neurotrauma, 26 (6): 827–840.
[11] Magnan P, De Mezzo S, Heck S, Boehrer Y. (2011). Approche métrologique du chargement d'une membrane exposée au blast. Rapport S-R 123/2011 de l'Institut Franco-Allemand de Recherches de Saint-Louis, France.
[12] Ouellet S., Williams K. (2008). Characterisation of defence research and development Canada's mannequin for the assessment of blast incapacitation and lethality (DRDC MABIL). Proceeding of the Personal Armour Systems Symposium, Brussels.
[13] Phillips, Y.Y., Mundie, T.G., Yelverton, J.T. and Richmond, D.R., 1988. Cloth Ballistic Vest Alters Response to Blast. J. Trauma, 28 (1): S149–S152.
[14] Prat, N.J. Boutillier, J. Cardona, V. Monterspan, F. Menini, W. Mosnier, J. et al., 2019. Injury and Biomarkers from Pigs Following Isolated Open-Field Blast Exposure Depend on Ballistic protection Level, in Poster from the Military Health System Reseach Symposium, Kissimmee, Florida.
[15] Przekwas A. (2008). Multiscale computational modeling if lung blast injuries. In Explosion and blast-related injuries, Elsayed NM, Atkins JL (ed). Elsevier Academic Press: London; 163–260.
[16] Sekine, Y. Saitoh, D. Yoshimura, Y. Fujita, M. Araki, Y. Kobayashi, Y. et al., 2021. Efficacy of Body Armor in protection against Blast Injuries Using a Swine Model in a Confined Space with a Blast Tube. Ann. Biomed. Eng., 49(10): 2944–2956.
[17] Stuhmiller J.H., Masiello P.J., Ho K.H., Mayorga M.A., Lawless N., Argyros G. (1999) Biomechanical Modeling of Injury from Blast Overpressure. NATO Rep. RTO-MP-20, Aug. 1999 (Available from FTIC).
[18] Sundaramurthy A., Alai A., Ganpule S., Holmberg A., Plougonven E., Chandra N. (2012). Blast-Induced Biomechanical Loading of the Rat: An Experimental and Anatomically Accurate Computational Blast Injury Model. Journal of Neurotrauma; 29(13):2352–2364.
[19] Tan X.G., Kannan R., Przekwas A.J. (2012a). A Comparative Study of the Human Body Finite Element Model Under Blast Loadings, ASME International Mechanical Engineering Congress and Exposition, Paper No. IMECE2012-89072, 829–836.
[20] Tan X.G., Kannan R., Przekwas A.J., Ott K., Harrigan T., Roberts J., Merkle A. (2012b). An Enhanced Articulated Human Body Model under C4 Blast Loadings, ASME international Mechanical Engineering Congress and Exposition, Paper No. IMECE2012-89067, 821–828.
[21] Wood, G.W. Panzer, M.B. Shridharani, J.K. Matthews, K.A. Capehart, B.P. Myers, B.S. et al., 2013. Attenuation of Blast Pressure behind Ballistic Protective Vests. Inj. Prev., 19(1): 19–25.
[22] Zhu F., Mao H., Dal Cengio Leonardi A., Wagner C., Chou C., Jin X., Vandevord P., Yang K.H., King A.I. (2010). Development of an FE model of the rat head subjected to air shock loading. Stapp Car Crash Journal; 54:211–25.
[23] Zhu F., Skelton P., Chou C.C., Mao H., Yang K.H., King A.I. (2012). Biomechanical responses of a pig head under blast loading: a computational simulation. International Journal Numerical Methods Biomedical Engineering.

Light-Weight Armour for Defence & Security
LWAG 2026

Production of Large Homogeneous Delamination in Aeronautical CFRP Laminates from Smaller Laser Shocks

Bryan Better[a]*, Michel Arrigoni[b], Aboulghit El Malki Alaoui[b], Christine Espinosa[a], Serge Guetta[c]

[a]*Institut Clément Ader (ICA) ; Université de Toulouse ; CNRS, UPS, INSA, ISAE-SUPAERO, IMT Mines Albi, 3 rue Caroline Aigle, Toulouse, 31400, France*
[b]*ENSTA | Institut Polytechnique de Paris, UMR CNRS 6027, IRDL, 2 rue François Verny, Brest, 29806, France*
[c] *NUCLETUDES, 3 avenue du Hoggar, Les Ulis, 91940, France*

Extended Abstract

The growing use of composite materials in aeronautical structures has led to changes in lightning strike certification due to the low electric conductivity of polymer-based light-weight structures [1]. A metallic protective grid is placed between the external protective paint and the CFRP structure. It acts as a sacrificial layer to dissipate the high current impulsion. In some configurations, damage still appear in the core of the composite structure. The physical events behind these damage mechanisms are not yet fully understood but some authors link them to successive electric confined explosions of the protective layer creating thermomechanical shocks. While the total delaminated area can be reproduced with a mechanical impact of similar impulse on bare CFRP, the spatial distribution of lightning strike damage does not present the typical conical shape of mechanical impacts. A deeper analysis of lightning strike damage is thus necessary. Following previous works [2] which highlighted analogies between the damage of lightning strike and laser shocks on CFRP, this paper studies the possibility of creating a large homogeneous delamination from a series of laser shocks of smaller radius arranged in a grid pattern. After selecting the appropriate energy density level and grid size, the proposed protocol is conducted on a disk-shaped sample. The damage position variability is studied and the microtomographic analysis of the post-mortem sample is used to validate the methodology. Strategies to improve the homogeneity of the delamination are discussed.

The CFRP of interest was manufactured and is courtesy of Airbus [1]. The composite laminate is composed of 13 unidirectional plies lightweight carbon epoxy with a quasi-isotropic stacking sequence $[45/-45/90/45/-45/0/90_{0.5}]_s$ for a total thickness of 1.651 mm. This structure is subjected to successive impacts of few mm of diameter resulting from laser shocks produced by the BELENOS laser hosted at the IRDL lab (UMR CNRS 6027). The BELENOS laser is a high energy pulsed Nd-YAG laser able to deliver up to 3 Joules in a pulse duration of 7.5 ns at half maximum at a rate of 10 Hz on a diameter of a few mm. Single pulse is enabled with a shutter. The experimental setup is visible in [3]. As the sample is not in a vacuum chamber, the energy density is limited by the laser breakdown threshold in air which is around 4 $GW.cm^{-2}$ at 1064 nm in air and $10\ GW.cm^{-2}$ in water [4]. The front face was polished to create a planar surface, and a 20 µm thin aluminium layer was glued on the composite as the laser-aluminium interaction is more studied in the literature than the laser-carbon-epoxy composite laminate interaction. Eventually, a water confinement is used, during the laser-matter interaction, to increase the amplitude and pulse duration of the laser shock produced in the CFRP [5]. The first ply on the impacted side is denoted ply 1. Previous experimental campaigns on the CFRP of interest were able to determine the damage threshold at an energy density of around 14 $J.cm^{-2}$ with a water confinement. To obtain a large and homogenous delamination in the CFRP using several laser shocks, two main features are analysed: the homogeneity of delamination produced by a single laser shock and the coalescence of the delamination when

* Corresponding author. Tel.: +33 561338814
E-mail address: Bryan.BETTER@isae-supaero.fr

subjecting the sample to several laser shocks. As the composite of interest has thin plies, laser shocks may produce unwanted branching intralaminar cracks from the delamination. To minimize this effect, three energy densities above the damage threshold and with a water confinement were selected to test the best candidate able to produce a homogenous delamination. The micrographs (Figure 1) depict a change in the damage observed with respect to the energy density. At a lower energy density (22.2 J.cm^{-2}), out of plane intralaminar damage is observed in the penultimate ply. At the intermediate energy density (24.9 J.cm^{-2}), this intralaminar damage is mixed with a homogeneous delamination while at the highest energy density (26.6 J.cm^{-2}) only a homogeneous delamination is visible. The extent of the crack depends on the intensity of the reflected release wave at the free surface of the sample, the position where it crosses the rarefaction wave and the local strength of the materials. As this CFRP includes thermoplastic nodules in the interlaminar resin, its local out-of-plane strength is increased compared to that having not nodules. Conversely, thinner plies may have a reduced out of plane strength. Increasing the energy density could enable the local out-of-plane stress to exceed the material strength closer to the rear surface, leading to a change from an intralaminar to interlaminar damage. As the energy density $26.6\,J.cm^{-2}$, obtained with a 22.5° polarising angle, seems to result in a single homogeneous delamination, this polarising angle was selected to study the coalescence of the delamination.

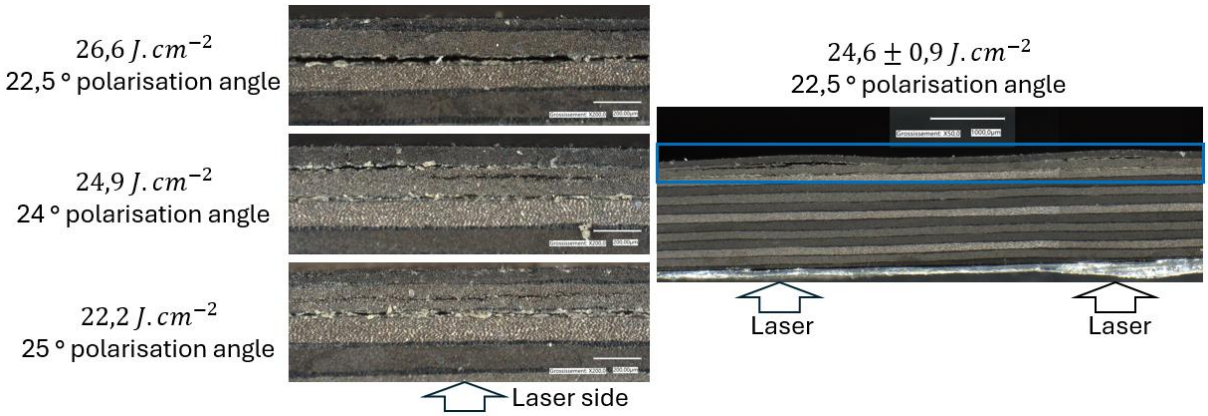

Figure 1: Micrographs of sample cross section of the preliminary tests with the corresponding energy density and angle for the polarizing glass. The laser impacts the sample on the bottom side. Left: x200 view near the rear face of the three tested energy density. With the increase in energy density, the intralaminar damage seems to shift to interlaminar damage. Right: Composition of two x50 view from two adjacent laser impacts from the coalescence test. The distance between the impacts seems too high to enable the coalescence of the delamination from one shot to its adjacent shot.

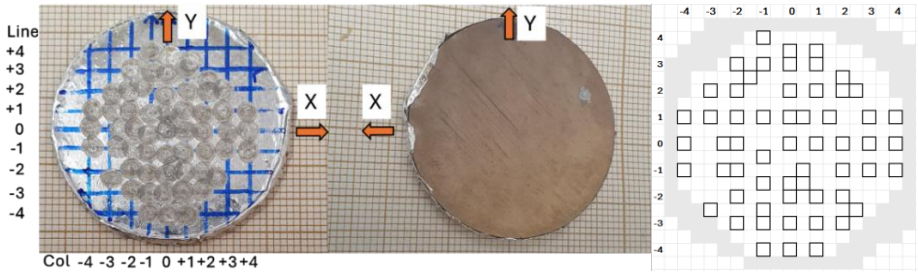

Figure 2: Post-mortem front (left) and rear (middle) views of the CFRP sample subjected to 57 laser shots arranged in a 3mm grid pattern at an energy density of $24.7 \pm 0.4\,J.cm^{-2}$ and effective impact positions relative to the grid with a 0.75 mm precision error (right).

This coalescence is analysed by shooting five adjacent impacts in a line spaced out by 5 mm. The characteristic distance between shots was chosen based on the diameter of the impacts of up to 4 mm as to not overlap the ablation crater. The angle of the line was chosen as 0° to reflect an intermediate case between a line in the fibre direction (45°) and in the transverse direction (-45°) of both the first and last ply of the laminate. Similarly, the dimensions and homogeneity of the delamination is analysed using micrographs (Figure 1). The mean energy density of the impacts is $24.6 \pm 0.9\,J.cm^{-2}$ which is closer to the intermediate tested energy density and could explain the multiple delamination. No interaction between the impacts is observed in this configuration. As the 5 mm characteristic distance was too long to enable the coalescence of delamination, it was reduced to 3 mm for the feasibility test. This introduces new parameters such as overlapping between the ablation diameters. This could create potential unwanted multiple delamination and raises the question of the order of the shots or more generally the choice of the pattern to follow. The feasibility test was conducted on a disk-shaped sample of 35 mm diameter. To facilitate the analysis with microtomography, a grid pattern was used with a characteristic length of 3 mm along

the 0° and 90° directions. Due to the number of shots required to produce one sample (57 shots), the repeatability was not evaluated. The post-mortem views are visible in Figure 2. Due to the spatial uncertainty of the laser spot, some shots are not aligned with the grid, creating additional overlap between shots. The approximate position of the centre of the shots relative to the grid is also depicted in Figure 2.

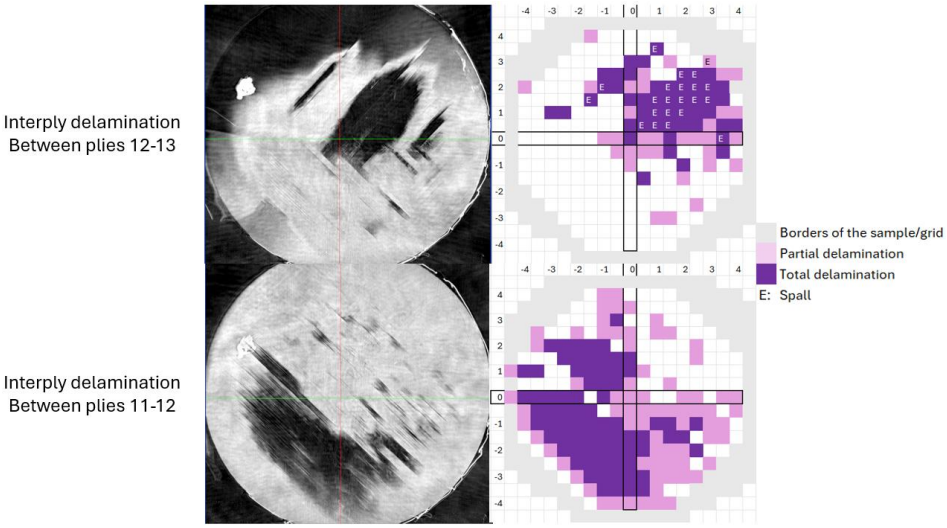

Figure 3: Left: Planar microtomographic view at the height of the interplay. The red and green lines cross at the centre. Right: Cartography of the delamination relative to the grid for the corresponding interface.

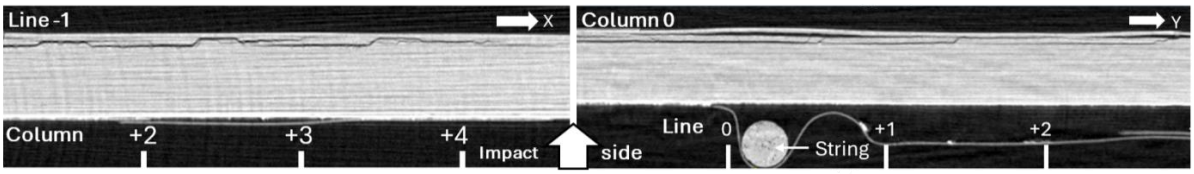

Figure 4: Through thickness microtomographic view of the CFRP sample. Left: Crenelated damage due to a grid pattern without overlap. Right: Multiple delamination due to a grid pattern with symmetrical overlap. The string was applied for the tomography as an axis reference.

The whole sample was subjected to a microtomographic analysis with a characteristic length of 18 µm (Figure 3) and the map of damage in the sample was analysed with a 1.5 mm resolution based on the reference columns and lines depicted in Figure 4. A large delamination was created near the rear face of the sample. Several areas seem to produce a variation on the homogeneity of the delamination. The impacts aligned with the grid and without overlap (for example at line -1 and columns +2/+4 in Figure 2 & 4) produce delamination behind the ablation crater but the coalescence of these delamination generate a cross-ply branching towards an interface closer to the rear face. This may be due to the edge effects around the impact, generating spherical rarefaction wave at the border of the loaded area. This progressively bows the initially planar shockwave as seen in Figure 5. These rarefaction waves propagate at the out-of-plane celerity of sound in the material. Due to the orthotropic behaviour

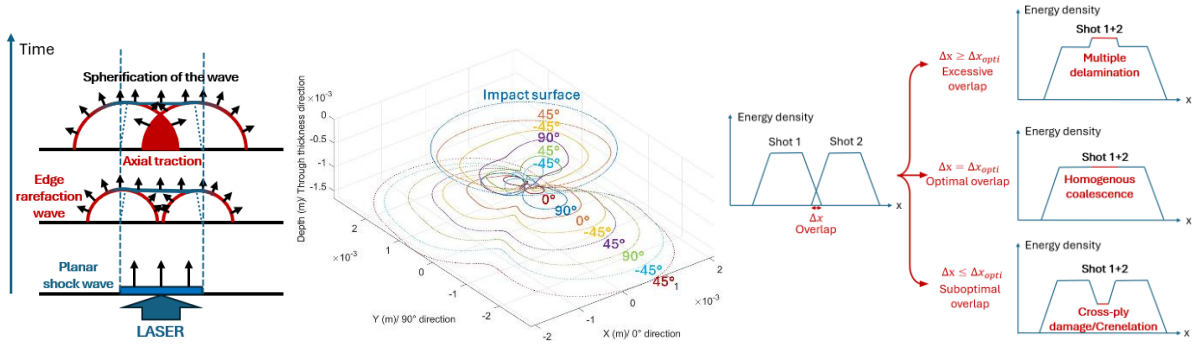

Figure 5: Possible explanations of the observed damage. Left: Bowing of the planar shock wave due to edge effects, adapted from [6]. Middle: Rough Matlab® modelling of the reduction of the planar shockwave surface area due to the orthotropic material. Each deeper surface up to the first 0° ply represents the planar area of the shockwave once it reaches the back of a ply. The later plies represent the corresponding bowed shock area. The longitudinal sound speeds were calculated according to Lukyanov's method [7] Right: Potential link between the coalescence of damage and the overlap between impacts.

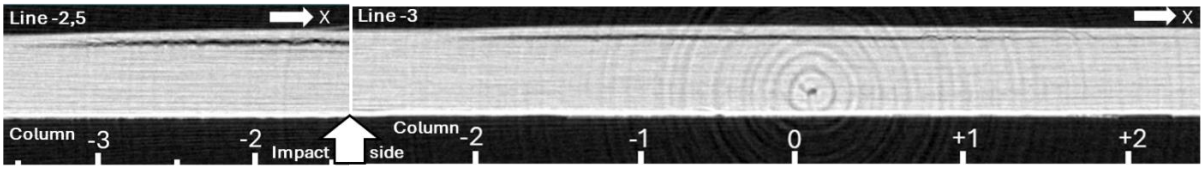

Figure 6: Through thickness microtomographic view of the CFRP sample. Left: Wavy homogeneous delamination produced by a staggered rows pattern. Right: Homogeneous delamination from a grid pattern with a unidirectional overlap.

of one ply, the celerity of sound in the fibre direction is higher than in the transverse direction [7]. Consequently, if one impact is assumed to be a disk surface at the front face, the planar shockwave becomes an ellipse after the first ply. Due to the stacking, the combination leads to a planar shockwave surface that is a combination of the transformation of each ply. A rough representation of this phenomenon was simulated with Matlab® (Figure 5). When the shock reflects as a release wave at the rear face, this change in shape modifies the radial position of the maximum stress. This shape, added to the decrease in local strength from previous shots may favour this crenelation shape in the observed damage.

A homogeneous delamination does not seem possible with a grid pattern without overlapping the impacts. A symmetrical overlap both in the 0° and 90° (column 0 line +1 of Figure 2 & 4) creates planar delamination, but the overlap causes the creation of two respective delamination in the thickness at different inter-plies. Due to the orthotropic behaviour of the plies, cracks in the border of a delamination will more easily propagate in the fibre direction of the ply underneath it, similarly to the butterfly-shaped delamination produced by mechanical impacts. As the last two plies are respectively in the -45° and 45° directions, a pattern in staggered rows as shown in line -2.5 column -3 results in a more homogeneous delamination (Figures 2 & 6). Some waving on the edges of the impacted area is visible suggesting the propagation took place in the cracks bordering the delamination. A more homogeneous delamination can be obtained in a grid pattern with an overlap along the 0° direction only as visible in line -3 columns -2 to 0 (Figures 2 & 6). A global hypothesis explaining the observed damage is tied to the overlap between impacts. Assuming the damage is cumulative, overlapping impacts enables coalescence through the summation of the local applied energy density (Figure 5), depending on the overlap the equivalent energy density mays lead to crenelation, homogeneous, or multiple delamination. The reason for the presence of waving is unknown.

To conclude, the ability to produce a large homogeneous delamination from several smaller laser shocks is demonstrated. The energy density is a key parameter as it directly changes the nature and position of the observed damage. Geometrical parameters such as overlap showed the alteration of the homogeneity of the delamination. Notably for the tested CFRP, an orthonormal grid pattern is not appropriate for samples much larger than the laser spot due to the crenelation of the damage while for smaller samples, inducing a symmetrical overlap, results in multiple delamination. Staggered rows or one direction overlap led to more homogeneous results. These preliminary results need to be consolidated as only one sample was analysed. Further work could also study the sensitivity of the damage to the path arrangement of the shots or analyse new patterns such as a checked pattern.

References

[1] Bigand A. et al. Destructive and Non-Destructive Analysis of Lightning-Induced Damage in Protected and Painted Composite Aircraft Laminates. Aerospace 2025;12;5.
[2] Better B. et al. Mechanical and Thermal Contributions to the Damage Suffered by an Aeronautical Structure Subjected to an Intense and Sudden Electrical Discharge. Aerospace 2025;12;5.
[3] Casapu, M. et al. Laser-Induced Shockwaves for Damage Assessment and Characterization at High Strain Rates in the Fiber Direction of Unidirectional Composites. Materials Letters 2024; 361, 136083.
[4] Sollier, A. et al. Numerical Modeling of the Transmission of Breakdown Plasma Generated in Water During Laser Shock Processing. The European Physical Journal-Applied Physics 2001;16;2, 131-139.
[5] Fabbro R. et al. Physical study of laser-produced plasma in confined geometry. Journal of Applied Physics 1990; 68, 775-784.
[6] Boustie M. et al. Study of Damage Phenomena Induced by Edge Effects into Materials Under Laser Driven Shocks. Journal of Physics D: Applied Physics 2007;40;7103
[7] Lukyanov A.A. An Equation of State of a Carbon-Fibre Epoxy Composite Under Shock Loading. The European Physical Journal B 2010;74;35-45

Light-Weight Armour for Defence & Security
LWAG 2026

Armox 440T plates subject to buried blast: a benchmark for appliqué systems

Sam Clarke[a,b]*, Andrew Barr [a], Andy Tyas[a,b], Ross Waddoups[a,b]

[a]*University of Sheffield, School of Mechanical, Aerospace and Civil Engineering, Sir Frederick Mappin Building, Sheffield, S1 3JD, UK*
[b]*Blastech Ltd., The Innovation Centre, 217 Portobello, S1 4DP, UK*

Extended Abstract

Loading of vehicle undercarriages from the detonation of shallow-buried explosives remains a serious threat. One method to protect lightly armoured vehicles is to retrofit them with appliqué armour. A key performance metric of this armour is its deformation under loading, which must be limited to avoid impact upon vehicle occupants. Armox 440T is commonly used due to its high load capacity, strength-to-weight ratio, ductility and low cost.

Here, we present the development of an appliqué system test apparatus. This is designed to provide both repeatable loading and boundary conditions to enable the comparison of newly produced armours against a developed Armox 440T benchmark. The work builds on the authors' previous work [1] to establish a methodology that produces very consistent loading from shallow-buried detonations. Tests were conducted with a range of explosive masses and plate thicknesses. Plate deformations have been captured by stereo high-speed digital image correlation and were compared to a commonly used low-cost peak deflection method (aluminium crush-block).

Since the benchmark trial series, a new reduced scale modification to the original apparatus has been developed to enable reduced cost testing of armour system prototypes (450 mm vs the original 955 mm). A proof-of-concept dataset is provided for Armox 440T for saturated soils showing a high repeatability in the test arrangement.

Test Methodology

One of the elements that has historically hampered the investigation of the output from buried charges is the repeatability between nominally identical tests. The authors have shown previously that this repeatability is not only a product of the preparation techniques used but also the soil type utilised [2,3]. The important element here is that the uniformity of the soil directly reflects the repeatability (even if the same average particle size is present). This has been quantified indirectly through looking at variations in overall impulse but also using discrete pressure measurements in a dedicated apparatus [4,5]. Hence, in the current testing careful consideration has been made to both the soil type used and preparation methodology (which will be outlined below).

The overall experimental setup was designed to enable half-scale testing (half-geometry scale version of STANAG threat level M2 as given in AEP-55 [6]), apart from the use of PE4 for all tests as recommended by UK MoD. Due to the physically smaller charges being used (1/2 scale by geometry, 1/8 scale by mass and energy), the size of the soil container has also been scaled down to emulate the boundary conditions stipulated in AEP-55 except for the boundary being cylindrical rather than rectangular. This arrangement is shown in Figure 1.

Armour targets, approximately half the thickness of those used on armoured vehicles, were mounted to a custom-designed rigid reaction frame to provide a consistent boundary condition for plate deformation measurements. Half-

* Corresponding author. Tel.: +44 114 222 5703
E-mail address: sam.clarke@sheffield.ac.uk

scale models were used to allow a future comparison of alternative material types, such as light-weight armours. The target plates in this arrangement are 995 mm square.

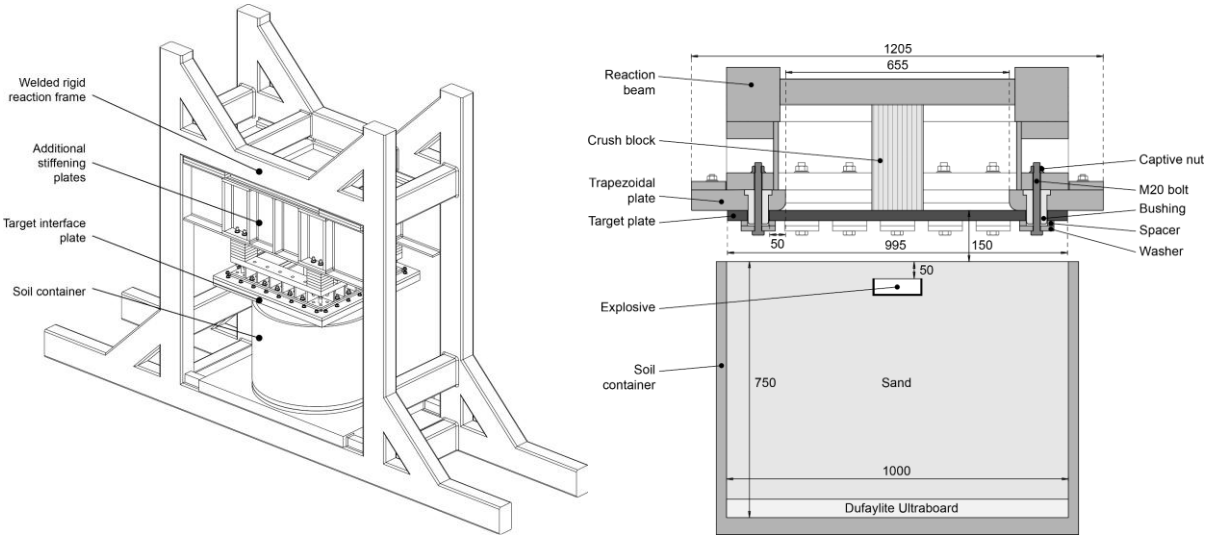

Figure 1: Overview of original test apparatus (left), soil arrangement (right) [1].

Controlling soil parameters has been shown to effectively reduce the variability of buried charge experiments and so the methods of filling the container with soil were replicated from previous studies [2-5,7]. Soil containers were constructed from 30 mm thick rolled mild steel plate formed into a 1000 mm internal diameter, 750 mm tall cylinder, with a 50 mm thick mild steel plate welded to the base. A layer of cardboard energy-dissipating material was added into the base of the soil bin; three layers of 18 mm thick Dufaylite Ultraboard were cut to size and placed in the base of the soil bin and then covered with plastic sheet to protect the cardboard from moisture. The reason for this addition was to protect the base of the soil bin from plastic deformation (which then constrains the ability to accurately ascertain the soil volume in future tests). The soil containers were filled with Leighton Buzzard 14/25 sand, as was used in previous studies [2-5,7]. Leighton Buzzard is a well-rounded uniform (0.58-1.12 mm) quartz 'filter' sand of which national equivalents are usually available (e.g. Ottawa, Hvidbjerg or Wessem Sands). The target density for the sand was 1.62 Mg/m^3 for all tests and was achieved to within 1.45%.

PE4 charges were buried in the sand. The charges were bottom-detonated 3:1 cylinders, packed into open-topped, 3D printed, PLA plastic cases with 4 mm thick walls and bases. Each charge was buried with an overburden of 50 mm of sand. To place the charge, a cavity was excavated approximately 5 mm wider than the charge geometry. Excavated material was placed into a sealed bag so that it remained at the correct moisture content. The stand-off distance was 150 mm for all initial tests, as measured from the soil surface to the rear (upper surface) of the target plate. A non-electric detonator was inserted into the top of the explosive charge, and the soil was replaced above the charge. The mass of soil remaining in the bag was then weighed to determine that the density of the replaced soil was the same as the excavated material. A sectional view through the test arrangement is shown in Figure 1.

Figure 2: Example of 3D point cloud generated from 16 plate photographs [8]

Data was captured with either an aluminium crush block or a stereo high-speed camera array, from which DIC was utilised to provide displacement-histories. Photogrammetry was also utilised to provide a full residual displacement profile for each of the tests, as shown in Figures 2 and 3.

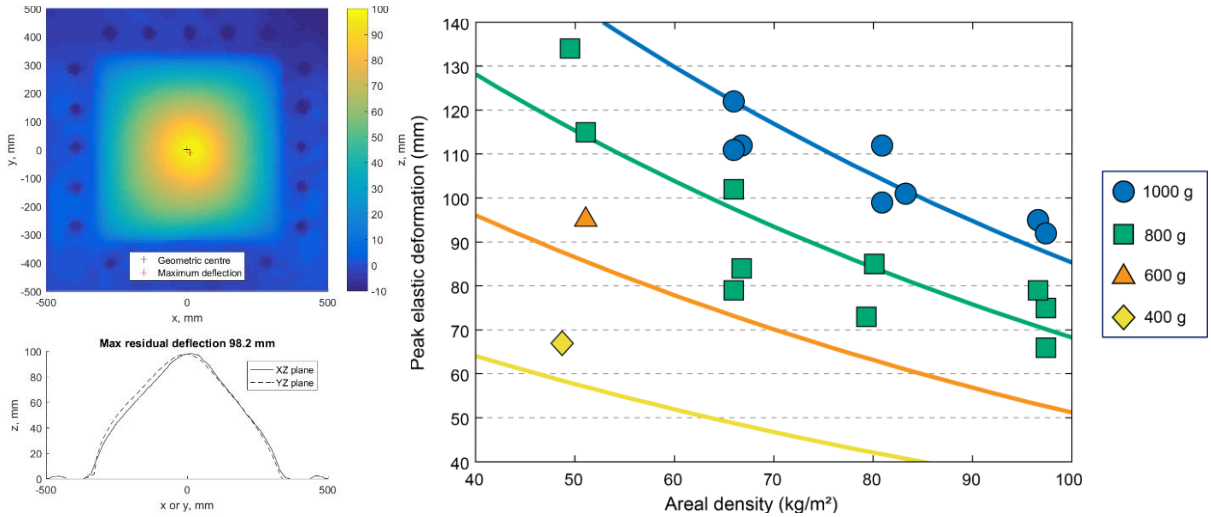

Figure 3: Residual profile obtained from photogrammetry (left). Peak deformation (measured from crush block compression) of Armox 440T as a function of target areal density for different explosive masses. Contours of the curve fits to the data (Eq. (1)) for charge masses of 400 g, 600 g, 800 g, and 1000 g have also been superimposed. [1] (right).

Benchmark Development

Initial testing found that the results from DIC showed a systematically lower peak deflection (despite final residual deflections being nominally identical). Numerical modelling of test showed that despite the alumimium crush block having a relatively low mass, its initial impulse takeup (from being in contact with the reverse face of the target plate) led to an overcompaction of the crush block due to it's own inertia. Further testing has sought to ensure an initial air gap between the target plate and the crush block is allowed during setup.

For the geotechnical conditions considered in this paper, the peak deformation, D, as recorded from the aluminium honeycomb crush block, depends on the armour areal density, A, and the detonation of a charge mass, M, according to:

$$D = 0.24367 M e^{-0.0105A} \quad (1)$$

The result of this equation is plotted against the recorded data in Figure 3. This equation provides a benchmark by which the performance of new appliqué systems can be assessed, based on deflection performance and material areal density.

Reduced Scale Modifications

One of the limitations of the original work was the physical scale of the plates that need to be manufactured. At 995 mm wide this is a large plate and for novel materials likely beyond the manufacturing capabilities for small-scale batch production. This has led the authors more recently to scale down the benchmark to ¼ of full-scale, allowing smaller plates to be tested (as well as having advantages of reduced soil container size and charge mass). This replicates the setup used previously [5], consisting of a bottom-detonated 78g PE4 cylindrical charge with a depth of burial (DOB) of 28mm. A stand-off distance (SOD) of 105mm was used to generate loading which allows for the plate to experience sufficient plastic deformation as to assess its performance.

Plates within this new reduced scale system are only required to be 450 mm square. To ensure sufficient loading was applied to the plate from the burial conditions, the soil was saturated [2]. So that air was not trapped within the soil matrix the soil was saturated from the base, slowly, using a buried perforated hose. In the production of the reduced-scale system the opportunity was also taken to refine the crush block arrangement to ensure over-crushing did not occur. This was achieved by using a smaller section of crush block held within a retaining steel tube. The position of the tube relative to the rear of the target plate can be adjusted to ensure an initial gap exists. Numerical modelling was used to inform the exact position of the crush block to ensure that contact was made with the target plate during the test, but that the target plate would in turn not contact the supporting tube. This arrangement is shown in Figure 4. These modifications ensured that the DIC results aligned well with crush block data as shown in Table 1. As expected from testing done in the interim [5] the saturated soils provided both a more aggressive

and more repeatable loading condition, as the soil moisture content (and lack of air voids) govern the behaviour. However while the overall magnitude of loading is very consistent, the distribution of this loading is non-uniform in the case of the Stanag soil [7] where large individual gravel particles are present. For Armox 440T this localisation is of no consequence, however for lightweight armour systems the loading distribution may have a more detrimental effect – see Waddoups et al 2026 LWAG paper [9].

Figure 4: Crush block before and after testing

Table 1: Summary of reduced scale 4.5mm thick Armox 440T test condition and results.

Test	*Soil Type*	*Bulk Density (Mg/m^3)*	*Moisture Content (%)*	*Measurement Type*	*Peak Deformation (mm)*	*Residual Deformation (mm)*
1	LB	1.967	21.05	Crush block	45	38.0
2	Stanag	2.195	12.56	Crush block	47	34.8
3	LB	1.966	21.10	DIC	47.6	38.3
4	Stanag	2.198	12.45	DIC	47.5	37.3

Conclusions

The authors have shown a large-scale benchmark for Armox 440T armour systems (of varying thickness) proven against a range of charge sizes. The benchmark is provided to evaluate the relative performance of appliqué systems based on their areal density and peak dynamic deflection.

Initial results from a reduced, quarter-scale Armox 440T benchmark is also provided to allow the testing of pre-production samples of novel appliqué systems.

References

[1] Elgy, I.D., Clarke, S.D., Fuller, B.J., Barr, A.D., Armstrong, D.W., Gant, M.T.A., Keirl, J.J., Porter, G.C.E., Softly, I.D., & Tyas, A. (2021). Deformation of Armox 440T plates subject to buried explosive charge detonations: A benchmark for appliqué systems, International Journal of Impact Engineering, 150, https://doi.org/10.1016/j.ijimpeng.2021.103819

[2] Clarke, S. D., Fay, S. D., Warren, J. A., Tyas, A., Rigby, S. E., Reay, J. J., Livesey, R., & Elgy, I. (2015). Geotechnical causes for variations in output measured from shallow buried charges. International Journal of Impact Engineering, 86, 274–283. https://doi.org/10.1016/j.ijimpeng.2015.08.009

[3] Clarke, S. D., Fay, S. D., Warren, J. A., Tyas, A., Rigby, S. E., Reay, J. J., Livesey, R., & Elgy, I. (2017). Predicting the role of geotechnical parameters on the output from shallow buried explosives. International Journal of Impact Engineering, 102, 117–128. https://doi.org/10.1016/j.ijimpeng.2016.12.006

[4] Rigby, S. E., Fay, S. D., Tyas, A., Clarke, S. D., Reay, J. J., Warren, J. A., Gant, M., & Elgy, I. (2018). Influence of particle size distribution on the blast pressure profile from explosives buried in saturated soils. Shock Waves, 28(3), 613–626. https://doi.org/10.1007/s00193-017-0727-7

[5] Clarke, S., Rigby, S., Fay, S., Barr, A., Tyas, A., Gant, M., & Elgy, I. (2020). Characterisation of buried blast loading. Proceedings of the Royal Society A: Mathematical, Physical and Engineering Sciences, 476(2236). https://doi.org/10.1098/rspa.2019.0791

[6] NATO. Procedures for evaluating the protection level of armoured vehicles - mine threat. Allied Eng. Publication (AEP) 55, Vol.2, Edition C, Version 1, February, 2022.

[7] Waddoups, R., Clarke, S., Tyas, A., Rigby, S., Gant, M., & Elgy, I. (2023). An Approach to Quantifying the Influence of Particle Size Distribution on Buried Blast Loading. Eng, 4(1), 319–340. https://doi.org/10.3390/eng4010020

[8] Fuller, B (2018) Loading from Shallow Buried Blast Events and the Effect on Plate Deformations, PhD Thesis, University of Sheffield. https://eprints.whiterose.ac.uk/id/eprint/89987/

[9] Waddoups, R., Clarke, S. D., Curry, R. J., Lodge, T. J., & Hibbert, A. (2026). DIC determination of localised loading on blast loaded plates from coarse soils. In proceedings of: Light-Weight Armour for Defence & Security, LWAG 2026.

Light-Weight Armour for Defence & Security
LWAG 2026

Quantitative Experimental Assessment of Failure in Armour Materials under Ballistic-Relevant Loading

Luca Corallo[a]*, Patricia Verleysen[a]

[a] *Department of Electromechanical, Systems and Metal Engineering, Materials Science and Technology-DyMaLab, Ghent University, Technologiepark 46, Zwijnaarde, 9052, Belgium*

Extended Abstract

The development of ballistic materials and protection systems requires mechanical data obtained under loading conditions representative of in-service impact scenarios. However, conventional full-scale ballistic testing programmes are resource-intensive, and offer limited insight for efficient screening of multiple candidate materials and for supporting armour design. This contribution presents an in-service–driven framework for laboratory-scale ballistic testing to bridge the gap between full-scale experiments and conventional mechanical tests. In this study, we conducted finite element (FE) simulations replicating the ballistic tests reported by Børvik et al. [1] on a 12 mm-thick Weldox steel plate impacted by projectiles with different nose shapes with the aim of identifying the stress states governing the target deformation and failure. The elastoplastic and damage behaviour of the Weldox steel plate was modelled according to the modelling framework presented in Børvik et al. [2]. Particularly, the target response was described by the isotropic von Mises yield criterion coupled with the Johnson-Cook (JC) hardening model, while damage was accounted for using the JC damage initiation criterion, coupled with an energy-based fracture model accounting for the progressive degradation of material strength. Figure 1 shows the FE prediction of the ballistic limit, along with the results presented in [1,2].

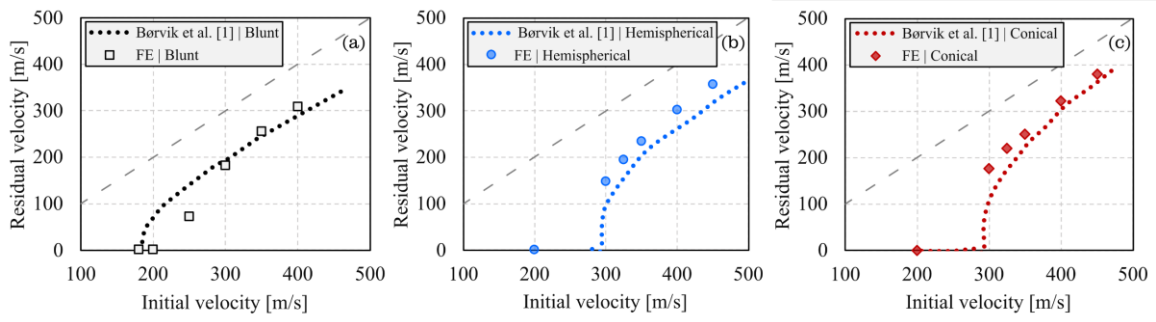

Figure 1: Ballistic limit Weldox 460 E steel from Børvik et al. [1] (dotted line) and FE prediction (discrete points). FE results for three different impactor geometries (a) blunt, (b) hemispherical and (c) conical.

In Figure 2, we provide full representation of the stress state in the target during penetration. In the deviatoric π-plane, the stress state is fully described by two polar coordinates $R = \sqrt{2J_2}$ and $\gamma = \text{asin}\left[-\frac{J_3}{2}\left(\frac{3}{J_2}\right)^{3/2}\right]/3$ expressed in terms of the second and third deviatoric invariants of the deviatoric stress tensor $\boldsymbol{\sigma}$. Additionally, the hydrostatic stress, proportional to the first invariant of the stress tensor, i.e., $\sigma_H = tr(\sigma)/3 = I_1/3$, is represented via a colour scale. Note that, this representation includes all the three invariants (I_1, J_2, J_3). J_2 and J_3, on the one hand, regulate the material's elastoplastic response. I_1, or σ_H, on the other, regulates the triaxiality factor, i.e., $TF = \sigma_H/\sigma_{Mises}$, which in the JC damage initiation criterion governs the onset and development of damage in target. FE results are

* Corresponding author. Tel.: +32 93310430
E-mail address: Luca.Corallo@UGent.be

reported at the projectile-target interface (Figure 2a-c) and at the target mid-thickness (d-f) for an initial projectile velocity of 300 m/s. The blue arrow indicates the stress path to damage initiation and the associated stress state, marked by the larger data point on the von Mises yield surface. In the case of the blunt projectile (Figure 2a,d), the deformation and failure processes were mainly dominated by combined compression-shear stresses. A larger degree of stress heterogeneity was found for the hemispherical projectile (Figure 2b,e), though it is also primarily dominated by compression and shear. For the conical projectile, the stress state near the impactor nose was dominated by almost pure compression (Figure 2c), whereas a more heterogeneous stress distribution developed at the target mid-thickness (Figure 2f). FE results at the onset of damage, including triaxiality, Lode angle γ, and Lode parameter L, are given in Table 1. Figure 2 highlights the predominance of extreme high-pressure, in the range -5 to 1 GPa, and combined compression-shear stresses $(0° \leq \gamma \leq 30°, 0 \leq L \leq 1)$, with only limited transitions to the tensile quadrant $(-30° \leq \gamma \leq 0°, -1 \leq L \leq 0)$.

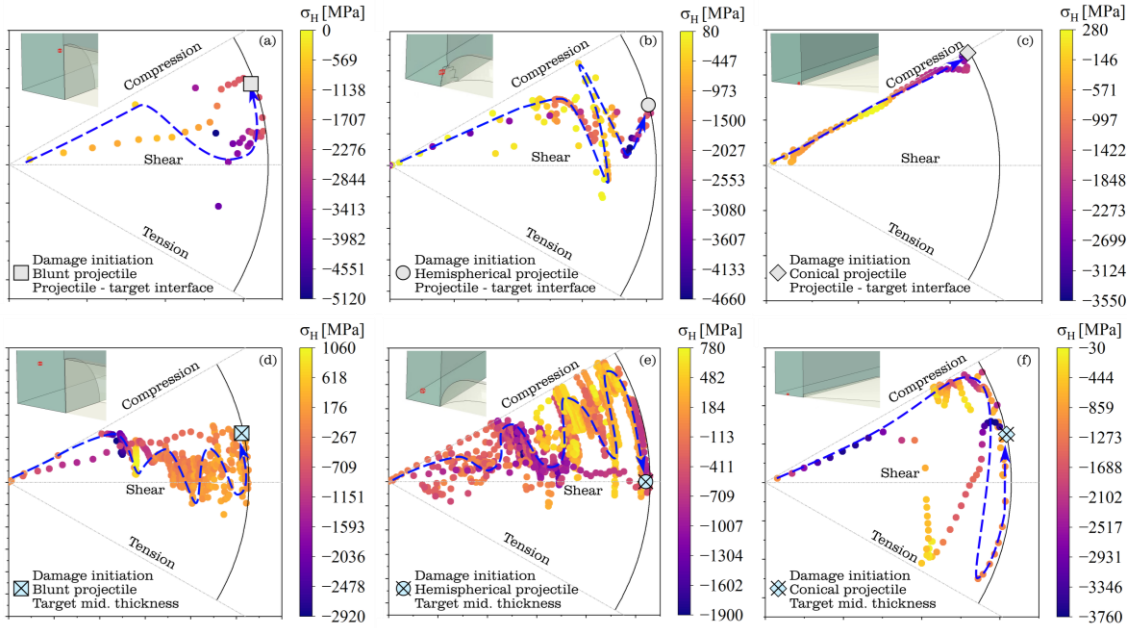

Figure 2: Stress state distribution in the π-plane: blunt (a,d), hemispherical (b,e), and conical (c,f). Results are extracted at the projectile–target interface (top) and at the target mid-thickness (bottom). The colour scale represents the hydrostatic stress, σ_H

Table 1: Overview stress state variables of Weldox plate penetration at the onset of damage.

		σ_{Mises} [MPa]	σ_H [GPa]	TF [-]	γ [°]	L [-]
□	Blunt, projectile-target int. (B, PT)	802	-2.2	-2.78	18.7	0.6
⊠	Blunt, target mid-thickness (B, MT)	1286	0.2	0.15	11.8	0.4
○	Hemispherical, projectile-target int (H, PT)	1016	-3.6	-3.6	13.2	0.4
⊗	Hemispherical, target mid-thickness (H, MT)	1267	-0.5	-0.42	-0.05	0.0
◇	Conical, projectile-target int (C, PT)	619	-3.1	-5	29.7	1.0
⊗	Conical, target mid-thickness (C, MT)	771	-2.8	-3.61	11.6	0.4

Over the past decades, considerable research efforts have been devoted to the development of specimen geometries capable of reproducing the extreme loading conditions arising in the target material during penetration tests as close as possible. These include specimen geometries that promote combined compression-shear stress states. Furthermore, given the key role of stress triaxiality in modelling and predicting ductile damage, sample geometries were specifically designed to investigate the material response in the negative stress triaxiality regime, namely under negative hydrostatic stress σ_H. We investigated the suitability of two existing laboratory-scale testing techniques for characterizing metals under combined compression-shear loading and negative stress triaxiality. First, we considered the cylindrical compression sample with spherical recess proposed by Kubík et al. [3]. In this specimen, the spherical notch promotes the onset of large, localized plastic deformation at the minimum cross-section, resulting in localized combined compression-shear stress and high hydrostatic pressures. Whereas compression tests on smooth cylindrical specimens typically result in triaxialities of about −0.33, this specimen geometry leads to triaxialities of about −0.55 for 2024-T351 aluminium alloy and −0.64 for AISI 1045 carbon steel. Next, we considered the combined shear-compression specimen presented by Dorogoy et al. [4]. This specimen was specifically designed to achieve a homogeneous stress state over the gauge length while imposing extreme

shear conditions that enable the study of adiabatic shear bands. In their study on 1020 steel, the authors reported an almost constant triaxiality of about -0.4 from yielding up to a plastic strain of 0.7. In our work, FE models were developed based on the geometrical information reported in [5] (see also Figure 3) and in [4], respectively. For both specimens, we adopted the material properties of the Weldox steel plate used in the penetration simulations.

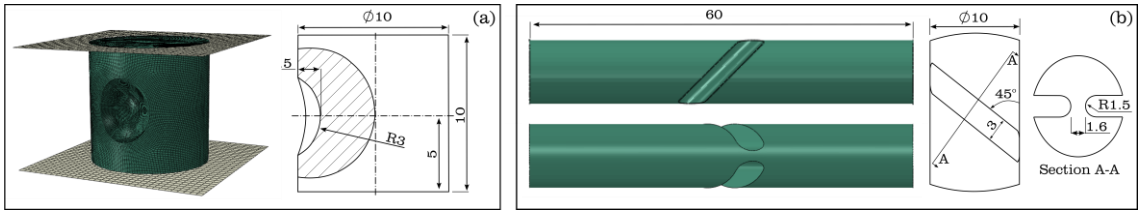

Figure 3: FE model and drawing of the (a) compression sample with recess [5] and (b) combined shear-compression sample [4].

Figure 4 shows the FE results for the notched compression sample at different stages of the simulation. The results are reported from the notch tip up to a distance of 3 mm along the path indicated in Figure 4a, as the extracted quantities converge towards nearly constant values at larger distances. As noted by Kubík et al. [3], the introduction of such recess into a smooth cylindrical specimen amplifies the stress state in the vicinity of the notch. Notably, this test configuration makes it possible to impose extremely high-pressure values at the notch tip, reaching about 1.4 GPa after a compression displacement of 3.5 mm (see Figure 4d). It is worth noting that the low triaxiality values extracted from the FE results (see Figure 4e) are directly related to the different rates of growth of the von Mises stress and of the hydrostatic pressure. Specifically, the rate of growth of the hydrostatic stress at the notch tip is between two and three times greater than that of the von Mises stress. As a result, the triaxiality reaches a value close to −1.2 at a displacement of 3.5 mm.

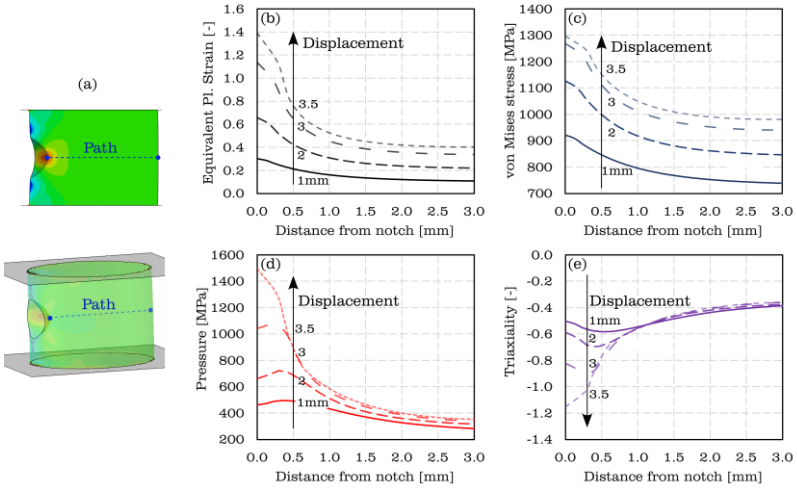

Figure 4: FE results compression sample with spherical recess at different values of displacement: (b) equivalent plastic strain, (c) von Mises stress, (d) pressure and (e) stress triaxiality. Results are extracted along the path indicated in (a).

The extreme conditions achieved through the introduction of a notch, however, come at the expense of the homogeneity of the stress state and plastic deformation across the specimen cross-section. At 2 mm of displacement, the plastic strain decreases from 0.6 to 0.3 over a short distance of 1 mm (see Figure 4b), while a variation of about 0.9 over a distance of 1 mm is observed after a compression of 3.5 mm. Similar observations can be made for the other reported quantities. While this test configuration can provide valuable insight into material behaviour under extreme loading conditions, for example through post-mortem microstructural analysis at the notch tip where failure is initiated, the strong heterogeneity of both the stress and strain fields constitutes its main limitation for material characterization and constitutive model identification. A possible solution to the heterogeneity of the stress and strain fields is provided by the combined shear-compression specimen proposed by Dorogoy et al. [4]. Figure 5 shows the FE results extracted at different stages of the simulation. The results are extracted along the 45° inclined gauge length, following the path indicated in Figure 5a. All data are reported as a function of the normalized path length. Despite the local effect of the notch ends, both the plastic strain (Figure 5b) and von Mises stress (Figure 5c) remain nearly uniform along the considered path. On the other hand, small variations along the gauge length are observed for both the pressure (Figure 5d) and triaxiality (Figure 5e), although these are negligible compared with those observed in the compression specimen. Despite the potential of this specimen geometry, its use is clearly limited by the level of pressure that can be imposed during testing, namely about 0.5 GPa at the centre of the gauge length for a plastic strain of approximately 1. Although this technique is suitable for

characterizing the fracture behaviour of metals at triaxialities below the uniaxial compression threshold of −1/3, it is important to acknowledge its limitation in reproducing the extreme high-pressure conditions shown in Figure 2.

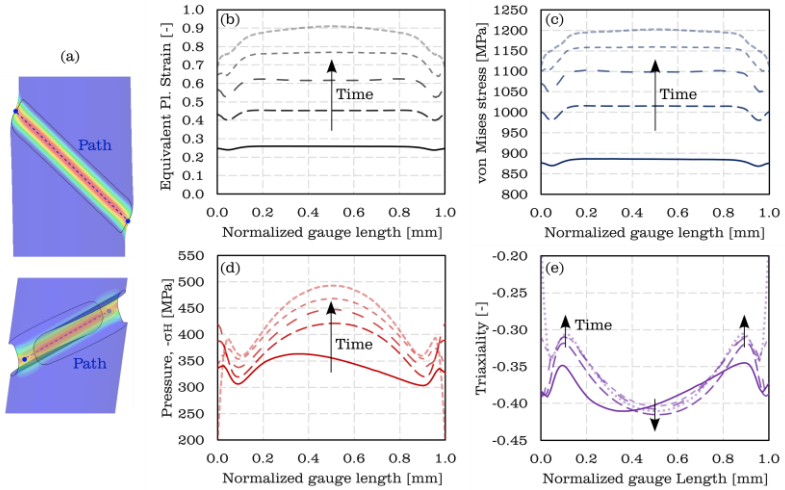

Figure 5: FE results combined shear-compression sample throughout the simulation: (b) Equivalent plastic strain, (c) von Mises stress, (d) Pressure and (e) Triaxiality. Results are extracted along the path indicated in (a).

For comparison with Figure 2, the FE results for both sample geometries are shown in Figure 6 in the π deviatoric plane. The locations of damage initiation for the three impactor configurations, at the projectile-target interface and target-mid thickness, are represented as larger data points (according to Figure 2) fictitiously placed on the same yield surface. Figure 6 clearly illustrates the differences in hydrostatic pressure and Lode angle reached during the penetration simulations and the two considered sample geometries.

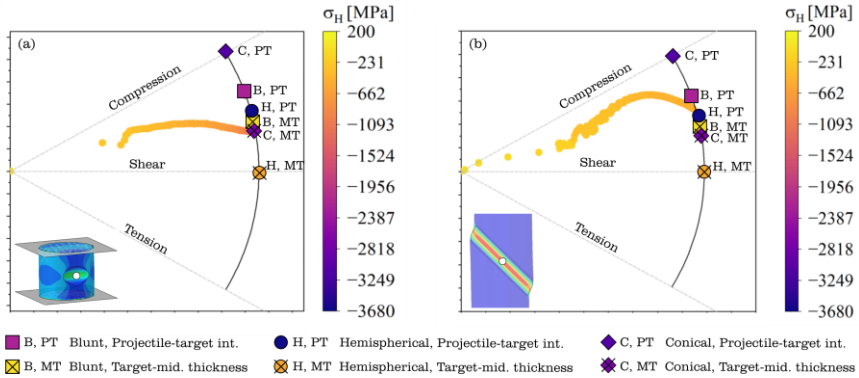

Figure 6. Stress state distribution in the π-plane (a) compression sample with spherical recess and (b) combined shear-compression sample. The colour scale represents the hydrostatic stress, σ_H

Given the limitation of currently available experimental techniques, further research efforts focus on a novel experimental methodology to test material samples under the extreme high-pressure and high-shear loading conditions encountered during ballistic impact events within a controlled laboratory-scale environment.

References

[1] Børvik T, Langseth M, Hopperstad OS, Malo KA. Perforation of 12 mm thick steel plates by 20 mm diameter projectiles with flat, hemispherical and conical noses Part I: Experimental study. International Journal of Impact Engineering 2002;27:19–35.

[2] Børvik T, Hopperstad OS, Berstad T, Langseth M. Perforation of 12 mm thick steel plates by 20 mm diameter projectiles with flat, hemispherical and conical noses Part II: numerical simulations. International Journal of Impact Engineering 2002;27:37–64.

[3] Kubík P, Šebek F, Hůlka J, Petruška J. Calibration of ductile fracture criteria at negative stress triaxiality. International Journal of Mechanical Sciences 2016;108–109:90–103.

[4] Dorogoy A, Rittel D, Godinger A. Modification of the Shear-Compression Specimen for Large Strain Testing. Exp Mech 2015;55:1627–39.

[5] Rajaraman D. Scratch abrasion modelling using continuum damage mechanics with experimental calibration at low stress triaxiality. dissertation. Ghent University, 2025.

Light-Weight Armour for Defence & Security
LWAG 2026

Experimental analysis of the effectiveness of a military helmet against blast threats

Dune STAMM[a,b], Natacha ELSTER[a], Sébastien DEMEZZO[a], Sébastien ROTH[b]

[a] *French-German Research Institute of Saint-Louis, 5 rue du Général Cassagnou, BP 70034, 68301 Saint Louis CEDEX, France*
[b] *Laboratoire Interdisciplinaire Carnot de Bourgogne, site UTBM, UMR 6303 CNRS / Université de Technologie de Belfort-Montbéliard, Belfort, France*

Abstract

These past years, the limits of traditional combat helmets against blast threats, which have become more prevalent due to the rise of Improvised Explosive Devices, have been highlighted. However, the ability of helmets to mitigate primary shock waves remains unclear. With the aim of improving protective helmets for soldiers in the future, it is important to first understand the phenomena that occur, particularly how the shock wave interacts with the helmet. For this reason, experiments were conducted on the Hybrid III head and neck, wearing a helmet and positioned at a height of 1.50m and at a distance of 1.80 m from the explosive charge. The whole head/helmet setup was mounted on a rigid support that securely held the head in a fixed position throughout the test, while allowing height adjustment and rotation. Regarding the instrumentation, a probe sensor was installed to measure the parameters of the incident wave and six pressure sensors were placed all over the head namely at eye level, on the forehead, on the top, on the ears, and on the back of the head (covered and uncovered by the helmet). The experiments were conducted in order to see the interaction of the helmeted head with the shock wave. Furthermore, angular velocity data were recorded at the center gravity of the Hybrid III head as well as linear acceleration for both head and helmet. Finally, influence of orientation (0°, 90° and 180°), loading (200g, 500g and 1200g C-4) and pads materials were also investigated during the experimental campaign. These experimental trials evidenced that tested helmet mitigate overpressure at the front but amplify it at the rear due to a phenomenon called, according to the literature, the "underwash effect". Depending on the orientation of the head, this phenomenon is also observed. In addition, increasing explosive charge raises surface pressure, impulse, and positive phase duration, thereby amplifying head injuries despite helmet use. Comparisons with unpadded tests also showed that padding effectively attenuates pressure and impulse, underscoring its necessity. Moreover, both load and padding significantly influence acceleration and angular velocities, which may be the cause of head injuries. Finally, this experimental campaign showed the limits of ballistic helmets against blast threats with a concordance of previous studies in the literature. It seems necessary to improve the efficiency of helmets against such threats, by trying to add new materials to the helmet or by modifying its geometry.

Keywords: Blast-induced Traumatic Brain Injury (bTBI), Hybrid III headform, Helmet

1. Introduction

Blast-induced Traumatic Brain Injury (bTBI) has become a significant health concern for soldiers, especially during the Iraq and Afghanistan conflicts, where Improvised Explosive Devices (IEDs) became a major threat [1, 2]. Studies on UK and U.S. soldiers revealed that head injuries were highly prevalent during such conflicts despite the use of helmets and this raised questions about helmet effectiveness against explosions [3, 4]. Indeed, data reported that 77% (Afghanistan) and 79% (Iraq) of U.S soldiers who sustained any type of TBI were wearing their helmets at the time of injury [5]. In order to understand and reduce TBI, numerous studies have investigated the effects of protective equipment particularly helmets, against blast [6-8]. However, these studies vary considerably in methodology by employing different headforms or by varying sensor placements and particularly headform positioning relative to the triple point trajectory. Discrepancies in the results were observed and were notably influenced by the positioning of the headform relative to the explosive charge, particularly whether it was placed at the same height as the charge or above it. A review has summarized and analyzed the existing studies involving helmeted headforms exposed to blasts, highlighting their respective limitations while noting that, despite methodological differences, consistent patterns emerge. As a matter of fact, studies conducted under the most appropriate and controlled conditions have consistently shown that helmets tend to reduce pressure at the front of

the head while increasing it at the rear, a phenomenon commonly attributed to the “underwash effect” [9-12]. The aim of the present study is to provide a detailed comparison between the signals recorded on a bare head and those obtained with a helmeted head under blast loading. In particular, the study compares the first peak and the maximum peak pressures observed in the signals to assess how the helmet and pads modify the mechanical responses. The results are then compared with findings reported in the literature to evaluate consistency with previous studies and to further clarify the helmet role in altering pressure distribution and head kinematics during blast-induced loading conditions.

2. Materials and methods

2.1 Headfrom, helmet and instrumentation

The experimental headform used in the campaign was the head and neck assembly of a Hybrid III anthropomorphic test device, mounted on a support that allowed height adjustment and rotation. A single standard military helmet was used throughout the entire experimental campaign to ensure consistency, with markers placed on the head to control and verify its positioning. In addition, tests were also conducted on a bare head to allow direct comparison between helmeted and unhelmeted conditions. To measure the pressure distribution around the head, six pressure sensors (Kulite LQ0808) were strategically positioned: one at eye level, one on the forehead, one on the top of the head, one at the rear under the pads, one at the rear not protected by the pads and one at the level of the ears, as illustrated in Figure 1. In addition to pressure measurements, acceleration data were collected. A triaxial accelerometer was installed at the center of gravity of the Hybrid III head, as well as in the helmet (Kistler 8766). The aim was to compare acceleration responses between the helmet and the head to determine whether significant differences were discernible. Furthermore, the head was equipped with angular velocity sensors located at its center of gravity to record rotational kinematics during each test. Finally, the raw data were processed using a fourth-order low-pass Bessel filter, selected for its minimal phase distortion properties. The signals were sampled at a frequency of 1 MHz. Different cutoff frequencies were applied depending on the type of signal: 90 kHz for pressure data and 60 kHz for acceleration and angular velocity measurements.

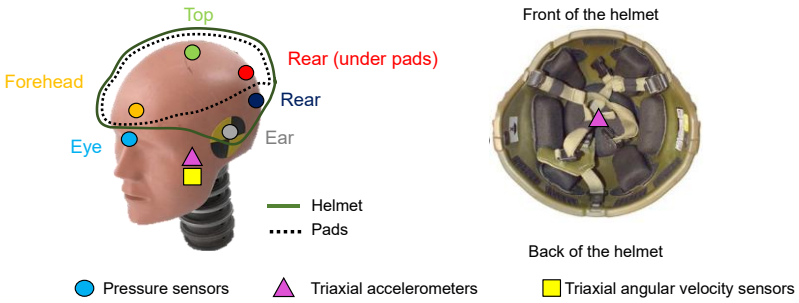

Figure 1: Instrumentation of the Hybrid III head and helmet

2.2 Blast setup

The blast loading was generated using C-4 explosive charges positioned at a fixed distance of 1.80 m from the head and neck assembly, as shown Figure 2. The charges were secured to ensure maximum stability during detonation and were placed at a height of 20 cm above the ground. To record the incident overpressure, a free-field pressure probe was situated 1 m from the headform at the same height as the eyes of the Hybrid III head, corresponding to 1.50 m above ground level, like illustrated Figure 2. This setup allowed the headform to be in the Mach stem region, just below the triple point, resulting in a single blast wave exposure. In addition, videos were recorded at 50 000 fps during 1s thanks to two high speed RGB cameras, one providing a wide-angle view of the entire setup and detonation, and the other focused on the headform to capture detailed head and helmet response during the interaction with the shock wave.

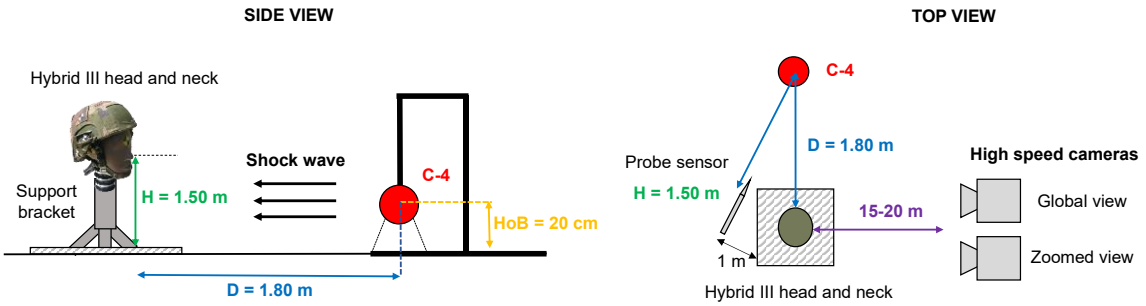

Figure 2: Experimental setup

In addition to evaluating the global effect of helmet wearing, the experimental campaign was designed to investigate the influence of several key parameters. Firstly, head orientation relative to the explosive charge was varied, with configurations at 0° (forehead facing the charge), 90° (left ear facing the charge), and 180° (occipital region facing the charge), in order to assess directional sensitivity to blast loading. Secondly, three explosive charge masses, 200 g, 500 g, and 1200 g, were selected to generate blast conditions representative of increasing injury severity levels. Finally, tests were conducted on a bare head, a helmeted head with pads, and a helmeted head without pads. Table 1 summarizes the complete test matrix of the experimental campaign with a total of 22 blast trials.

Configuration	Number of tests	Charge	Orientation	Helmeted head	Pads in the helmet	Incident pressure (kPa)	Positive phase duration (ms)	Impulse (kPa × ms)
1	3	500g	0°	Yes	Yes	156±13	1.74±0.06	82.5±2.2
2	3	500g	90°	Yes	Yes	156±13	1.74±0.06	82.5±2.2
3	3	500g	180°	Yes	Yes	156±13	1.74±0.06	82.5±2.2
4	3	200g	0°	Yes	Yes	84±7	1.61±0.15	46.6±2.0
5	3	1200g	0°	Yes	Yes	258±23	1.97±0.14	123.9±3.5
6	4	500g	0°	Yes	No	156±13	1.74±0.06	82.5±2.2
7	3	500g	0°	No	No	156±13	1.74±0.06	82.5±2.2

Table 1: Summary table of the different experimental trials, with incident pressure, positive phase duration and impulse obtained

3. Results

3.1 Surface pressure distribution across different head locations

The purpose was to investigate the pressure distribution at the head surface. Configuration 1 was selected for this analysis, corresponding to an average incident pressure of 156 ± 13 kPa, a positive phase duration of 1.74 ± 0.06 ms and an impulse of 82.5 ± 2.20 kPa×ms. The averaged surface pressure signals recorded by the six sensors under this configuration are presented in Figure 3. The highest maximum pressure is recorded at the eye region, followed by the rear of the head not protected by the pads, then the ears, the rear of the head protected by the pads, the forehead, and finally the top of the head. For the first four regions mentioned (eyes, unprotected rear, ears and padded rear), the maximum pressure corresponds to the first peak observed in the signal. In contrast, for the forehead and the top of the head, the maximum pressure does not coincide with the first peak. Instead, an initial pressure peak appears in the signal, followed by a second, higher peak that defines the maximum value.

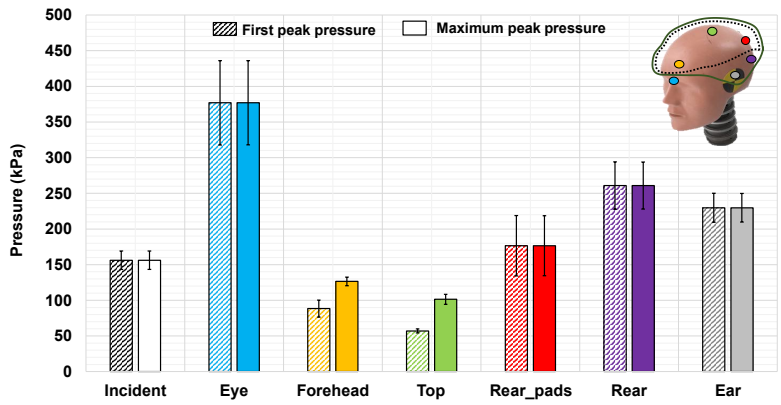

Figure 3: Maximum and first peak surface pressures measured at six distinct head locations

3. 2 The role of pads and shell in helmet performance

Under operational conditions, soldiers are wearing helmets equipped with padding systems. However, it is essential to determine whether these pads attenuate or, in some cases, contribute to pressure amplification during blast exposure. To investigate this effect, configurations 1, 6, and 7 were compared. Experimental observations indicate that the presence of pads reduces surface pressures compared to a helmet without pads, except for the eye sensor, better covered by the helmet without the pads. Therefore, beyond comfort and fit, helmet pads play a critical role in controlling load transfer, influencing both the magnitude and time evolution of blast-induced pressures on the head. Furthermore, comparison between helmeted and bare head have shown that helmet significantly modifies the time response at the top and forehead regions. To better elucidate the mechanisms governing these local responses, it is essential to distinguish the effect of the helmet shell alone and that of the complete helmet system including the internal padding. Figure 4 shows an exemple of pressure signals recorded at two sensor location for the three configurations:bare head, helmet with pads and helmet without pads. For most sensor locations (eye, ear, rear_pads, and rear), the time of occurrence of the maximum pressure remains nearly identical across the three configurations. However, noticeable differences are observed at the forehead and top locations, where the presence or absence of padding significantly affects the time history evolution of the signal. Indeed, although the pads appear to reduce the pressure amplitude compared with the unpadded helmet configuration, the occurrence of the maximum pressure is further delayed in time. A prominent feature of the helmet without pads is the presence of strong pressure reflections after the maximum, associated with wave interactions between the head and the rigid shell. These reflections are not observed in the bare head configuration and appear to be substantially attenuated when padding is included. The pads therefore play a critical role in mitigating wave reflections and reducing both the peak pressure and the positive impulse transmitted to the head. Overall, the results indicate that while the helmet shell alone can introduce additional wave interactions and local amplifications, the padding system contributes to damping these effects and limiting the transmitted loading. However, the combined shell and pad system leads to an important increase in surface pressure at the head compared with the bare head condition.

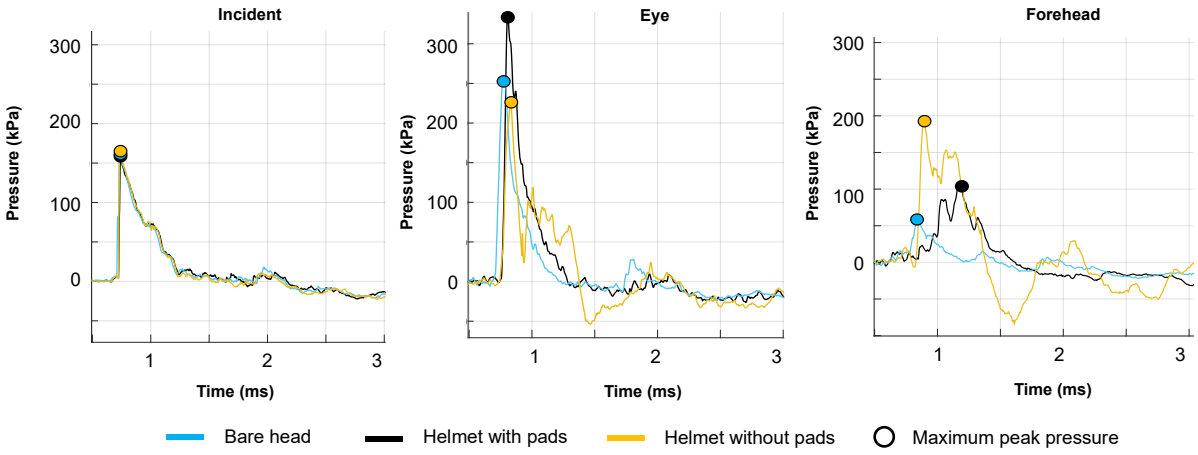

Figure 4: Comparison of order of appearance of maximum head surface pressures for the eye and forehead sensor

3.3 Head kinematic response: linear acceleration and angular velocity

The kinematic analysis showed that the resultant head acceleration remained of the same order of magnitude across configurations. In contrast, helmet acceleration was significantly higher than head acceleration, with helmet-to-head ratios ranging approximately from 1.5 to 8 depending on load level and orientation, confirming pronounced dynamic decoupling. Rotational kinematics were more strongly affected by helmet configuration. As a matter of fact, in the absence of pads, peak head angular velocity increased substantially compared to the padded condition, demonstrating the key role of the padding system in controlling rotational motion. Finally, for the head orientation, similar kinematic trends were identified for the 0° orientation (both bare and helmeted) and for the 90° orientation. In contrast, for the 180° orientation, both linear acceleration and angular velocity were reduced. This behavior is likely attributable to the higher effective neck stiffness of the Hybrid III dummy in this direction, which mechanically constrains and limits the linear and rotational motion of the head.

4. Discussion

Key findings on pressure distribution and head kinematics response were presented, the following discussion addresses the implications of these results and the limitations of the experimental setup. A direct comparison

between bare and helmeted configurations highlights notable differences in surface pressures. Superimposed signals reveal that, when the helmet is worn, interactions between the blast wave, helmet shell, and pads generate reflections within the confined space between the head and the helmet. These reflections contribute to local pressure amplification and modify wave propagation, leading to a delay in the occurrence of maximum pressures at specific locations. In particular, the maximum pressure at the top and forehead appears approximately 0.30 ms and 0.27 ms earlier for the bare head compared to the helmeted condition, whereas the timing at the eyes, ears, and rear of the head remains nearly identical, with differences below 0.06 ms. Furthermore, the presence of pads within the helmet attenuates some of these reflections, reducing peak pressures and impulse at the top and forehead while maintaining protection elsewhere.

In addition, comparison with studies from the literature employing a similar setup, namely with the explosive charge positioned beneath the headform [6, 13-18], allowed confirmation of key observations, including pressure amplification at the occipital region. Findings reported by McEntire et al. [19], Ford et al. [20] and in the present work consistently showed that helmet acceleration can exceed head acceleration, likely due to the dynamic response of the shell and the characteristics of the retention system under blast loading. Reported helmet-to-head acceleration ratios ranging from 1.4 to 10 emphasize the critical role of helmet–head coupling in the transmission and redistribution of inertial loads. However, this cross-study comparison also highlighted the sensitivity of experimental outcomes to subtle variations in setup conditions. In particular, helmet positioning and sensor placement on the head strongly influence measured pressures and kinematic responses. These aspects underline the difficulty of ensuring strict reproducibility in blast helmet testing and the importance of precise control of experimental parameters. Although standardized anthropomorphic test devices such as the Hybrid III dummy lack internal biofidelity and do not incorporate brain simulants, they have been extensively validated for impact testing through comparisons with PMHS data [21]. Their use therefore ensures consistent and reproducible external kinematic responses, which is advantageous for comparative studies. Nevertheless, their mechanical behavior is governed by the materials composing the head and neck assembly, which determine stiffness, damping, and wave transmission characteristics. One major limitation is the neck stiffness of the Hybrid III which likely influenced the measured kinematic response, particularly for the 180° orientation.

Finally, while our experiments provide valid and reproducible insights into helmet performance and head response under blast loading, establishing a detailed relationship between the influence of the charge, impulse and positive phase duration on head injuries remains challenging. To further enhance the interpretation of these results, integrating experimental data with validated finite element models and multi-parameter injury criteria would allow a more comprehensive assessment of injury mechanisms. Emerging surrogates, such as the BIPED model [22], offer promising opportunities to improve biofidelity in future studies but still remains nowadays challenging in order to mimic the human head.

5. Conclusion

This study provides a detailed characterization of helmet performance under primary blast loading, combining measurements of surface pressure, positive phase duration, impulse, linear acceleration and angular velocity. Regarding pressure results, helmet wearing was shown to significantly modify the surface pressures at different head locations. Amplification was particularly observed at the rear region, while notable changes were also identified at the top and forehead. Temporal analyses revealed that maximum pressures at the top and forehead were delayed when the helmet was worn, reflecting wave confinement and interactions between the blast wave, the helmet shell and the padding system. The presence of pads mitigated internal reflections and reduced pressure peaks and impulse, demonstrating their role in energy dissipation beneath the shell. Concerning kinematic results, helmet acceleration was consistently higher than head acceleration, highlighting dynamic decoupling. However, the resultant head acceleration remained relatively similar across configurations. Rotational kinematics were more sensitive to padding conditions, with pads effectively limiting angular velocity and thus reducing rotational motion. A comparison with data from the literature and limitations of the experimental setups were identified, including the use of a Hybrid III headform, its elevated neck stiffness and in particular the sensitivity to helmet positioning. Despite these constraints, the results are consistent with findings from the literature and contribute valuable insight into blast mitigation strategies. Future work should integrate validated numerical models and emerging biofidelic surrogates to better predict intracranial response. Overall, the study underscores the critical role of helmet design and padding in reducing blast-induced head injury risk.

6. Acknowlegments

The authors would like to thank Mr. Jonas WENDLING-BANDELIER and Dr. Pascal MAGNAN for their valuable assistance during the experiments as well as Prof. Dr.-Ing. Anne JUNG for their insightful advice and helpful discussions throughout this work.

References

1. Belmont, P.J., Goodman, G.P., Zacchilli, M., Posner, M., Evans, C., Owens, B.D.: Incidence and Epidemiology of Combat Injuries Sustained During “The Surge” Portion of Operation Iraqi Freedom by a U.S. Army Brigade Combat Team. Journal Of Trauma And Acute Care Surgery 68, 204 210 (2010). https://doi.org/10.1097/ta.0b013e3181bdcf95

2. Bird, S.M.: Fairweather CB Military fatality rates (by cause) in Afghanistan and Iraq: a measure of hostilities. International Journal Of Epidemiology 36, 841 846 (2007). https://doi.org/10.1093/ije/dym103

3. McGuire, R., Hepper, A., Harrison, K.: From Northern Ireland to Afghanistan: half a century of blast injuries. Journal Of The Royal Army Medical Corps 165, 27 32 (2018). https://doi.org/10.1136/jramc-2017-000892

4. ICasualties.org (2003) Iraq Coalition casualty count. http://icasualties.org/App/Fatalities. Accessed November 2024

5. Wojcik, B.E., Stein, C.R., Bagg, K., Humphrey, R.J., Orosco, J.: Traumatic Brain Injury Hospitalizations of U.S. Army Soldiers Deployed to Afghanistan and Iraq. American Journal Of Preventive Medicine 38, 108 S116 (2009). https://doi.org/10.1016/j.amepre.2009.10.006

6. Thomas, C.J.H., Johnson, C.E.: Investigation into helmet–head shock wave interactions at low overpressures through free-field blasts and schlieren imagery. Shock Waves 34, 399 412 (2024). https://doi.org/10.1007/s00193-024-01167-4

7. Sundar, S., Ponnalagu, A.: Biomechanical Analysis of Head Subjected to Blast Waves and the Role of Combat Protective Headgear Under Blast Loading: A Review. Journal of Biomechanical Engineering 143, 100801 (2021). https://doi.org/10.1115/1.4051047

8. Wallace D, Rayner S (2012) Combat helmets and blast traumatic brain injury. Journal Of Military And Veterans’ Health/Journal Of Military And Veterans’ Health 20:10. https://www.researchgate.net/publication/287947814_Combat_helmets_and_blast_traumatic_brain_injury

9. Rafaels, K.A., Shridharani, J.K., Bass, C.R., Salzar, R.S., Walilko, T.J., Wood, G.W., Panzer, M.B.: Blast wave attenuation: ballistic protective helmets and the head. Proceedings of the Personal Armour Systems Symposium (PASS), Quebec City, Canada, Sept. 13-17 (2010).

10. Zhang, J., Du, Z., Wang, X., Kang, Y., Ma, T., Zhuang, Z., Liu, Z.: Analyzing the contribution of helmet components to underwash effect under blast load. Acta Mechanica Sinica 40 (2024). https://doi.org/10.1007/s10409-024-24011-x

11. Li, J., Ma, T., Huang, C., Huang, X., Kang, Y., Long, Z., Liu, M.: Protective Mechanism of Helmet Under Far-field Shock Wave. International Journal Of Impact Engineering 143, 103617 (2020). https://doi.org/10.1016/j.ijimpeng.2020.103617

12. Santhanam, S.S., Alagappan, P.: Numerical and experimental study of underwash effect and its role in blast-induced traumatic brain injury. Shock Waves (2024). https://doi.org/10.1007/s00193-024-01183-4

13. Makris, A., Nerenberg, J., Dionne, J.P., Bass, C.R., Chichester, C.: Reduction of Blast Induced Head Acceleration in the Field of Anti-Personnel Mine Clearance. Engineering, Environmental Science (2006). https://doi.org/10.21236/ada458451

14. Bass, C.R., Davis, M., Rafaels, K., Rountree, M.S., Harris, R.M., Sanderson, E., Andrefsky, W., DiMarco, G., Zielinski, M.: A methodology for assessing blast protection in explosive ordnance disposal bomb suits. Int J Occup Saf Ergon. **11**(4), 347-61 (2005). https://doi.org/10.1080/10803548.2005.11076655

15. Thomas, C.J.H., Dogan, F., Johnson, C.E.: Experimental investigation of a viscoelastic liner to reduce under helmet overpressures and shock wave reflections. Frontiers In Bioengineering And Biotechnology **12** (2024). https://doi.org/10.3389/fbioe.2024.1455324

16. Baumer, T., Rapo, M.A., Wong, J.M., Powell, B.J., Juhas, B.D., Chan, P.C., MacKiewicz, J.F.: Blast Overpressure Measured on a Bare vs. Helmeted Rigid Headform. International Mechanical Engineering Congress And Exposition (2013). https://doi.org/10.1115/imece2013-63260

17. Rapo MA, Baumer T, Chan PC, MacKiewicz JF (2013) Reducing the Effects of Blast to the Head Through Load Partitioning. International Mechanical Engineering Congress And Exposition. https://doi.org/10.1115/imece2013-63257

18. Merkle, A., Carneal, C., Wing, I., Murphy, R.J., MacKiewicz, J.: Importance of Directionality on Helmet Performance During Blast Loading. Proceedings of the Personal Armour Systems Symposium (PASS), Cambridge, United Kingdom, September 8-12 (2014).

19. McEntire, B.J., Chancey, V.C., Walilko, T., Rule, G.T., Weiss, G., Bass, C., Shridharani, J.: Helmet Sensor - Transfer Function and Model Development. Technical Report US Army Medical Research And Materiel Command

20. Ford, M., Simmonds, K., Horner, D., Gauvin, J., Bagchi, A.: Blast Response Characteristics for an Instrumented Helmet on a Skull-Brain Surrogate. Volume **2**: Biomedical And Biotechnology Engineering; Nanoengineering For Medicine And Biology 105-110 (2011). https://doi.org/10.1115/imece2011-65699

21. Shin, J., Donlon, J., Richardson, R., Gepner, B., Forman, J., Östling, M., Kerrigan, J. Biofidelity Evaluation of the Hybrid-III 50th Male and the THOR-50M in Reclined Frontal Impact Sled Tests. Proceedings of the International Research Council on the Biomechanics of Impact Conference (IRCOBI), Porto, Portugal, September 2022.

22. Ouellet, S., Bir, C., Bouamoul, A. Direct comparison of the primary blast reponse of a physical head model with post-mortem humand subjects. Proceedings of the Personal Armour Systems Symposium (PASS), Cambridge, United Kingdom, September 8-12 (2014).

Light-Weight Armour for Defence & Security
LWAG 2026

Flexible protection and blast injury: experimental and numerical study using biofidelic thorax dummy

Gardère P [a,b], Boutillier J [b], Demezzo S [b], Delille R [c], Lauro F [c], Hirschler T [a], Roth S [a]

[a] *Laboratoire Interdisciplinaire Carnot de Bourgogne, site UTBM UMR 6303 CNRS/ Université de Technologie de Belfort-Montbéliard, 90010 Belfort, France*
[b] *French-German Research Institute of Saint-Louis, 5 rue du Général Cassagnou, BP 70034, 68301 Saint Louis CEDEX, France*
[c] *University Polytechnique Hauts de France, Laboratory LAMIH UMR CNRS 8201, 59313 Valenciennes, France.*

Abstract

Recent military conflicts and terrorist attacks have increased the exposure of personnel to explosive threats. Despite this growing risk, the effectiveness of flexible thoracic protection against blast waves remains insufficiently understood, with some studies suggesting that certain configurations may even aggravate injuries [1]. This study aims to characterize the interaction between blast waves and flexible protection systems using combined experimental and numerical approaches.

A blast test campaign was conducted using the SurHUByx surrogate [2], a biofidelic thoracic dummy reproducing human anatomical geometry. The mannequin was exposed to blast loading with and without flexible protection. Internal pressure, organ-level forces, and sternal acceleration were measured to assess biomechanical injury indicators. Comparison with the ISL biological database [3], which links blast exposure to injury severity, enabled correlations between measured physical quantities and injury risk. In parallel, a finite element model of the experimental configuration was developed and validated using the experimental measurements. The validated model provides a predictive framework to investigate the performance of different protective systems. The combined results highlight the complex interaction between blast loading and flexible protection and provide quantitative indicators for evaluating and improving thoracic protective equipment.

Introduction

The widespread use of explosive devices in modern conflicts has significantly increased the risk of blast exposure for both military personnel and civilians [4]. Blast waves generate complex injury mechanisms: primary blast injuries mainly affect air-filled organs, while secondary and tertiary effects arise from fragmentation and body acceleration [5,6]. Among these, thoracic blast exposure is particularly critical due to the vulnerability of pulmonary structures.

Experimental and numerical studies have improved the understanding of thoracic biomechanical response under blast loading [7–20]. However, the protective performance of thoracic protective equipment against blast overpressure remains poorly characterized. While some investigations report potential amplification of thoracic loading depending on protection configuration [21–23], others indicate beneficial protective effects [24,25]. This lack of consensus highlights the need for controlled studies linking biomechanical indicators—such as chest acceleration and internal pressure—to injury risk. A relevant approach consists in combining instrumented thoracic surrogates with validated numerical models. In this work, the SurHUByx mannequin [2,15], originally developed for non-penetrating projectile impacts, was used as an experimental platform for blast investigations.

This study presents a combined experimental and numerical investigation of the SurHUByx surrogate subjected to free-field blast loading with and without soft thoracic protection. Experimental measurements were used to correlate biomechanical indicators with injury thresholds and to validate a predictive numerical model capable of assessing the efficiency of thoracic protection systems.

Methods

Experimental methodology

A preliminary experimental campaign was conducted to verify measurement repeatability and ensure the structural and instrumental robustness of the SurHUByx surrogate prior to injury-level testing. The objective was to confirm that all embedded sensors (hydrophone, FlexiForce sensors, accelerometers, and strain gauges) could withstand blast loading without signal degradation or structural damage. Tests were performed under two configurations: no protection and, soft thoracic protection. Repeatability was assessed through analysis of measurement standard deviations. Following this validation phase, a second campaign investigated injury-level blast loading conditions. Target peak overpressures and positive phase durations were selected according to the classical Bowen curves and the refinements proposed by Boutillier et al [11] for pulmonary injury criteria.

The experimental setup consisted of a suspended C4 charge positioned at a prescribed stand-off distance from the mannequin to avoid ground-induced debris effects. A pencil probe, aligned with the surrogate at the same distance from the charge, measured the effective incident overpressure. A reference grid was placed behind the mannequin to enable visualization of the blast wave propagation, and the experiments were recorded using a high-speed camera operating at 50,000 frames per second fps. The mannequin was secured using 40 kg of ballast, resulting in a total mass of approximately 70 kg, representative of a nominal adult.

First campagne						
					number of repetitions	
Weight (g)	Lenght (cm)	P+ (bar)	T+(ms)	Impulse (bar.ms)	with TPE	without TPE
180	273	0,58	1,7	0,38	0	3
200	240	0,77	1,5	0,46	0	3
500	320	0,81	3,3	0,74	3	3
1000	330	1,22	2	0,92	4	2
Second campagne						
400	170	2,7	1,18	0,89	3	2
500	170	3,33	1,18	1	1	1
600	170	3,88	1,18	1,07	0	1
1000	330	1,22	2,06	0,92	2	1
2000	290	2,94	1,87	1,52	2	1
2000	250	4,4	1,87	1,85	1	2

Table 1 – Overview of the experimental blast configurations.

The SurHUByx mannequin is a biofidelic thoracic surrogate based on human body scan geometry (Roth et al. [26]) (Figure 1). Soft tissues and organs are modeled using tailored SEBS formulations to reproduce tissue-specific mechanical properties, while the skeletal structure (spine, ribs, sternum) is additively manufactured from polyurethane resin. Internal instrumentation includes FlexiForce sensors embedded within the organs (heart, lungs, liver, spleen), a hydrophone positioned posterior to the lung to record internal pressure during blast exposure, and strain gauges bonded to the ribs to monitor deformation and prevent fracture (5% strain threshold).

Figure 1: SurHUByx thoracic surrogate in two configurations: (a) witout thoracic protective equipment (TPE), and (b) equipped TPE.

Numerical methodology

The SurHUByxFEM finite element model was employed for the numerical analysis. Initially validated by Chaufer et al [2]. against non-penetrating projectile impacts and post-mortem human subject data reported by Bir et al [27], the model was originally developed in the Radioss solver. For consistency with the present study, it was transferred to LS-DYNA, and a revalidation was performed by replicating the projectile impact tests to ensure preservation of the mechanical response. Material parameters are detailed in Chaufer et al. [2].

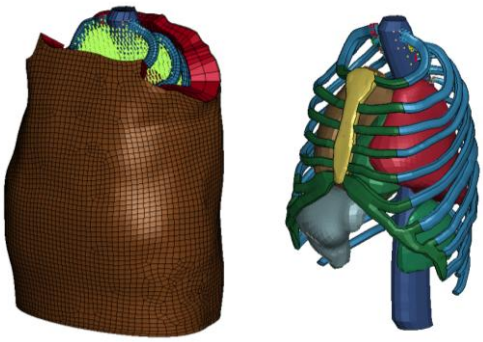

Figure 2 : Finite element model of the SurHUByx surrogate: configuration with (a) and without (b) mediastin, skin and muscle layers.

Blast loading was implemented using the Greer [28] method to reproduce experimental solicitation levels. Fluid–structure interaction was modeled using an ALE formulation coupling Eulerian air domains with the Lagrangian surrogate structure. All mannequin components were modeled as solid elements, except the mediastinum, represented using SPH particles. The simulations aimed to extract sternum acceleration and posterior lung pressure, corresponding respectively to accelerometer and hydrophone measurements, focusing on the replication of the unprotected experimental cases.

Resultats

Experimental

In the present study, VC_{max} is used as an injury indicator for blast loading, considering adapted injury thresholds relevant to blast-induced trauma. The viscous criterion is defined as the product of chest deformation velocity and normalized thoracic compression, and represents a biomechanical indicator of injury risk associated with rapid thoracic loading. Initially developed in the automotive safety field to assess thoracic injury during vehicle impacts, this criterion has been used to characterize injury related to high-rate chest deformation Lau et al [29]. Figure 3 presents the evolution of the maximum viscous criterion VC_{max} as a function of blast impulse for configurations with and without thoracic protection equipment (TPE).

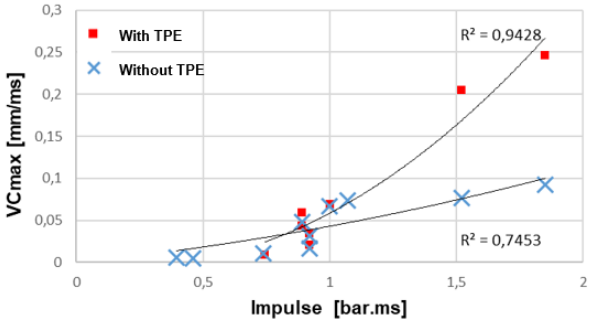

Figure 3: Maximum viscous criterion (VC_{max}) as a function of blast impulse for configurations with and without TPE.

However, the increase is more pronounced in the configuration equipped with soft thoracic protective equipment, resulting in higher VCmax values compared with the unprotected case at equivalent impulse levels. Below approximately 1 bar.ms, the difference between the protected and unprotected configurations appears negligible. At higher impulses, the presence of the protection leads to a systematic increase in VC_{max} suggesting an amplification of the thoracic deformation rate under these loading conditions. These results allow establishing a correspondence in injury risk between protected and unprotected scenarios as a function of impulse.

Kommentert [BJ(1)]: J'aurais mis ça dans les résultats car c'est directement ce que tu observes sur tes courbes.

Numerical Model

Figure 4 compares the experimental and numerical pressure–time histories obtained for the different blast scenarios. The numerical blast loading, implemented using the Greer [28] method, reproduces the main characteristics of the measured pressure profiles with good agreement. In particular, the predicted peak overpressure and the overall shape of the positive phase closely match the experimental probe measurements for each configuration.

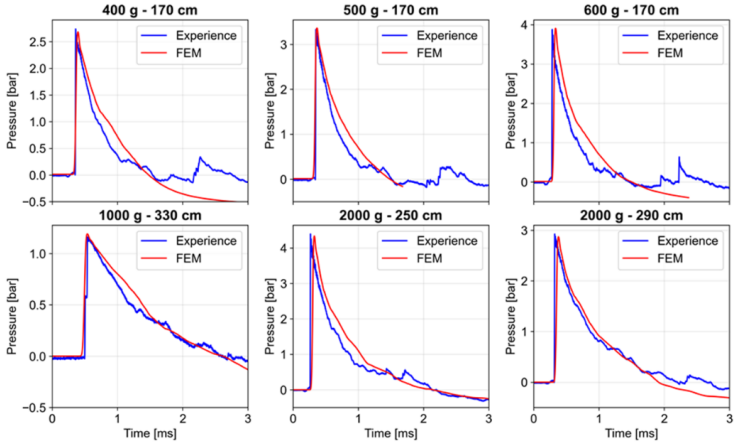

Figure 4: Comparison of experimental and numerical pressure–time profiles for the different blast scenarios.

The finite element model demonstrates an overall satisfactory agreement with the experimental measurements, particularly in terms of global response trends, as shown in Figure 5. A better agreement is observed for the acceleration signals, suggesting that the structural response of the surrogate is well captured. In contrast, larger discrepancies are observed for the pressure measurements, which may be attributed to limitations in the numerical representation of the blast loading and fluid–structure interaction. Despite these differences, the model is

considered sufficiently validated to reproduce the main features of the experimental response and can be used for qualitative analysis and comparative studies, although further refinements would be required for accurate pressure prediction.

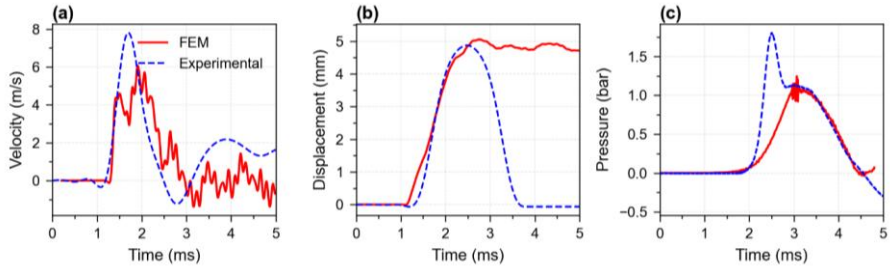

Figure 5 – Comparison of experimental and numerical responses: sternum velocity (a), sternum displacement (b), and right lung pressure (c), for a 2 kg C4 charge at a stand-off distance of 290 cm.

Discussion

Experimental

As shown in Figure 3, the observed increase in VC_{max} associated with the use of soft thoracic protection is consistent with observations reported in the literature [1,24,30,31], where certain protective configurations may increase thoracic loading under blast exposure. The innovative aspect of the present work lies in the ability to quantitatively characterize this amplification using the viscous criterion VCmax, thereby providing a biomechanical indicator linking blast impulse to injury risk. By using the unprotected configuration as a reference, VCmax-based injury thresholds were identified, with slight, moderate, and severe injury levels corresponding to approximately 0,051 ; 0,085 ; and 0,228 m/s, respectively.

Comparison with injury criteria derived from blunt ballistic impact studies shows that the VC thresholds identified for moderate and severe injury are approximately 0,8 and 2,8 m/s, respectively [32]. The values obtained under blast loading are lower than those typically reported for localized impacts. This difference can be attributed to the distributed nature of blast loading, which induces global thoracic deformation and may lead to injury at lower levels of viscous response. These results highlight the need for blast-specific injury criteria and support the relevance of VCmax as a unifying biomechanical metric across different loading conditions. Nevertheless, additional experiments would be required to increase the number of data points and fully confirm these preliminary observations.

Numerical model

As shown in Figure 4, minor discrepancies can be observed in the decay phase between the experimental and numerical pressure–time profiles. These differences may be attributed to simplifications inherent to the numerical blast representation as well as to local experimental effects. Nevertheless, the overall agreement demonstrates that the Greer approach provides a reliable reproduction of the blast loading conditions [28]. This validation ensures that the responses obtained from the numerical sensors, such as pressure and acceleration, are primarily governed by the mechanical behaviour of the SurHUByx FEM surrogate rather than by artefacts related to the blast generation method implemented in LS-DYNA.

Conclusion

This study presented a combined experimental and numerical investigation of blast-induced thoracic loading using the SurHUByx biofidelic surrogate. The results highlighted that soft thoracic protective equipment can increase the viscous criterion VC_{max} at higher impulse levels, suggesting a potential amplification of thoracic injury risk under certain blast conditions. The use of VC_{max} allowed a quantitative characterization of this effect and enabled the establishment of a correspondence between injury risk and blast impulse for protected and unprotected configurations. In parallel, the validated numerical model provides a reliable framework to further investigate blast–protection interactions and to support the optimization of thoracic protective systems

References

[1] Cooper GJ, Townend DJ, Cater SR, Pearce BP The role of stress waves in thoracic visceral injury from blast loading: Modification of stress transmission by foams and high-density materials in J Biomechanics 1991 Vol.24, No., pp.273-285

[2] Chaufer M, Delille R, Bourel B, Marechal C, Lauro F, Mauzac O and Roth S (2023), A new biomechanical FE model for blunt thoracic impact. Front. Bioeng. Biotechnol 2023;11:1152508.

[3] Boutillier J, Prat N, De Mezzo S, Magnan P, Naz P Blast-Related Lung Injury Risk Estimation Based on Chest Wall Velocity, Human Factors and Mechanical Engineering for Defense and Safety 2021

[4] Ramasamy A, Hill AM, Masouros S, Gibb I, Bull AM, Clasper JC. Blast-related fracture patterns: a forensic biomechanical approach. J R Soc Interface. 2011 May 6;8(58):689-98. doi: 10.1098/rsif.2010.0476. Epub 2010 Dec 1. PMID: 21123255; PMCID: PMC3061094

[5] De Palma R.G., Burris D.G., Champion H.R., and Hodgson M.J., Blast injuries, N. Engl. J. Med., vol. 352, pp. 1335–1342, 2005.

[6] Eftaxiopoulou T., Barnett-Vanes A., Arora H., Macdonald W., Nguyen T.-T. N., Itadani M., Sharrock A.E., Britzman D., Proud W. G., Bull A.M.J., Rankin S.M., Prolonged but not short duration blast waves elicit acute inflammation in a rodent model of primary blast limb trauma, Injury, Volume 47, Issue 3, 2016, Pages 625-632, ISSN 0020-1383,

[7] Axelsson H. Yelverton J.T., Chest wall velocity as a predictor of nonauditory blast injury in a complex wave environment, J. Trauma, vol. 40, no. 3, pp. S31–7, 1996.

[8] Merkle A. et al., Evaluation of the human surrogate torso model response to ideal and complex blast loading conditions, Proceedings of the Personal Armour Systems Symposium (PASS), pp. 678–687,2010.

[9] Yoganandan N., Pintar F. A., Schlick M., Humm J. R., Voo L., Merkle A., Kleinberger M., Vertical accelerator device to apply loads simulating blast environments in the military to human surrogates, Journal of Biomechanics, Volume 48, Issue 12, 2015, Pages 3534-3538,

[10] Boutillier J, Cardona V, Magnan P, Ogier M, De Mezzo S, Montespan F, Menini W, Mosnier J, Naz P and Prat NJ (2022) A New Anthropomorphic Mannequin for Efficacy Evaluation of Thoracic Protective Equipment Against Blast Threats. Front. Bioeng. Biotechnol. 9:786881. doi: 10.3389/fbioe.2021.786881

[11] Boutillier J., Willinger R., Deck., (2017) Contribution to the understanding andmodelling of the damaging effects ofairborne shock waves on the thorax, université de Strasbourg

[12] Christensen A.M., Smith V.A., Ramos V., Shegogue C., Whitworth M., Primary and secondary skeletal blast trauma, J. Forensic Sci. 57 (1) (2012), https://doi.org/10. 1111/j.1556-4029.2011.01938.x

[13] Zhou J., Tao G., Biomechanical modelling for the response of human thorax to blast waves, Acta Sin. 31 (4) (2015) 589–598.

[14] Bodo M., Roth S., Numerical investigation of similarity laws for blast simulation: open-field propagation and interaction with a biomechanical model, Mech. Adv. Mater. Struct. 25 (2017) 1140–1147,

[15] Roth S., Three-dimensional numerical study of the influence of the thorax positioning submitted to blast loading: Consequences on body trauma, Mech. Adv. Mater. Struct. (2018).

[16] Tang F., Guo Z., Yuan M., Qian X., Du Z., Mechanical response of human torso under blast loading, Safety Science, Volume 131, 2020, 104936

[17] Morena A, Peroni L, Scapin M. Numerical Investigation of the Blast-Induced Injuries Using an Open-Source Detailed Human Model. Int J Numer Method Biomed Eng. 2024 Dec;40(12):e3879. doi: 10.1002/cnm.3879. Epub 2024 Oct 21. PMID: 39433406; PMCID: PMC11618233.

[18] Lustig M., Gefen A., Epstein Y., Finite element modeling framework for evaluating the efficacy of protective plates in minimizing organ and tissue damage resulting from a blast wave impact, Journal of the Mechanical Behavior of Biomedical Materials, Volume 169, 2025, 107070

[19] Taddei L., Bracq A., Delille R., Bourel B., Marechal C., Lauro F., Roth S., Effect of blast loading on the risk of rib fractures: a preliminary 3D numerical investigation, Forensic Science International, Volume 326, 2021, 110930

[20] Phillips, Y. Y., Mundie, T. G., Yelverton, J. T., and Richmond, D. R. (1988). Cloth Ballistic Vest Alters Response to Blast. *J. Trauma* 28 (1), S149–S152. doi:10.1097/00005373-198801001-00030

[21] Gibson, P. W. (1994). Amplification of Air Shock Waves by Textile Materials. *J. Text Inst.* 86 (1), 119–128. doi:10.1080/00405009508631315

[22] Prat, N. J., Boutillier, J., Cardona, V., Monterspan, F., Menini, W., Mosnier, J., et al. (2019). “Injury and Biomarkers from Pigs Following Isolated Open-Field Blast Exposure Depend on Ballistic protection Level,” in Poster from the Military Health System Research Symposium, Kissimmee, Florida

[23] Long, J. B., Bentley, T. L., Wessner, K. A., Cerone, C., Sweeney, S., and Bauman, R. A. (2009). Blast Overpressure in Rats: Recreating a Battlefield Injury in the Laboratory. *J. Neurotrauma* 26 (6), 827–840. doi:10.1089/neu.2008.0748

[24] Wood, G. W., Panzer, M. B., Shridharani, J. K., Matthews, K. A., Capehart, B. P., Myers, B. S., et al. (2013). Attenuation of Blast Pressure behind Ballistic Protective Vests. *Inj. Prev.* 19 (1), 19–25. doi:10.1136/injuryprev-2011-040277
[25] Sekine, Y., Saitoh, D., Yoshimura, Y., Fujita, M., Araki, Y., Kobayashi, Y., et al. (2021). Efficacy of Body Armor in protection against Blast Injuries Using a Swine Model in a Confined Space with a Blast Tube. Ann. Biomed. Eng. 49 (10), 2944–2956. doi:10.1007/s10439-021-02750-x
[26] Roth, S., Torres, F., Feuerstein, P., and Thoral-Pierre, K. (2013). Anthropometric dependence of the response of a thorax FE model under high speed loading: Validation and real world accident replication. Comput. Methods Programs Biomed. 110 (2), 160–170. doi:10.1016/j.cmpb.2012.11.004
[27] Bir, C., Viano, D., and King, A. (2004). Development of biomechanical response corridors of the thorax to blunt ballistic impacts. J. Biomechanics 37, 73–79. doi:10.1016/ s0021-9290(03)00238-0
[28] Greer A.D., et al, Numerical Modeling for the Prediction of Primary Blast Injury to the Lung, A thesis presented to the University of Waterloo, Ontario, Canada, 2006
[29] Lau IV, Viano DC. The Viscouc Criterion – bases and applications of an injury severity index for soft tissues.Proceeding of the Thirtieth Stapp Car Crash Conference, 1986, 123-142, SAE Paper No. 861882
[30] Gibson P.W., Amplification of air shock waves by textile materials, Journal of Textile Institute, 86(1), pg 119-128, 1995.
[31] Skews B.W., Bugarin S., Blast Pressure Amplification due to Textile Coverings, Textile Research Journal (2006) Vol 76(4): 328–335 DOI: 10.1177/0040517506062264
[32] Bir C., The evaluation of blunt ballistic impacts of the thorax, Submitted to the Graduate School of Wayne State University Detroit, Michigan 2000.

formaterte: Fransk (Frankrike)

Light-Weight Armour for Defence & Security
LWAG 2026

Calibration of Four Failure Models for HHA and UHA Steel

Andreas Heine[a]*, Robbert Rietkerk[a], Werner Riedel[a]

[a]*Fraunhofer EMI, Ernst-Zermelo-Str, 4, 79104 Freiburg, Germany*

Abstract

As presented at prior LWAG meetings, we have taken steps toward a full characterization of high-hardness-armor (HHA) and ultrahigh-hardness-armor (UHA) steels [1], in order to obtain a predictive simulation capability for those most modern grades of armor steel. The widespread materials SECURE 500 and ARMOX 600 were considered as representatives of the HHA and UHA material classes, respectively, for this study.

The first major step was the derivation of a suitable plasticity model. For this purpose, an application of machine learning methods turned out to be most promising for efficient and unbiased calibration of a model [2]. In an inverse optimization process, parameters for the Johnson-Cook plasticity model were obtained that are perfectly reproducing the results of the material tests [3], thereby also confirming the general suitability of the Johnson-Cook strength model for HHA and UHA steels. That approach also shed new light on the interpretation of certain material tests and model parameters [4].

After a brief review of the above earlier findings, the present contribution complements those with recent results on the failure modeling of the same two steel grades. Four different failure models were included in this study – the Johnson-Cook failure model, its modification by Chocron-Erice-Anderson, the Xue-Wierzbicki model, and the Hosford-Coulomb model. These models consider in different ways the effects of stress triaxiality or Lode-angle dependence. For both materials and all four models, simulation parameters were derived. This derivation was done both in a purely experimental and in a combined experimental-numerical approach, the latter approach more realistically considering the actual loading paths. A quantitative comparison between the obtained models regarding their capability to reproduce the test data is presented allowing statements about the suitability of the different models. Rather than providing an extended abstract or a full paper, we refer to the related journal publication [5].

References

[1] Heine A, Früh P, Riedel W. Steps toward characterizing and modeling UHA steels for armor design purposes: LWAG 2019, Roubaix, France.
[2] Rietkerk R, Früh P, Riedel W, Heine A. Machine learning as an alternative approach to quantify the thermal softening of HHA and UHA armor steels: LWAG 2022, Freiburg, Germany.
[3] Heine A, Rietkerk R, Riedel W. New approaches to the constitutive modeling of protective materials: LWAG 2024, Rocamadour, France.
[4] Rietkerk R, Früh P, Lörcher L, Sauer M, Heine A, Riedel W. Bridging the gap between rate-dependent plasticity and stress wave dynamics: Calibrating a constitutive model for high-strength steel by inverse optimization. International Journal of Impact Engineering **195** (2025) 105087.
[5] Rietkerk R, Heine A, Riedel W. Calibration of triaxiality and Lode angle parameter-dependent failure models for high and ultra-high-hardness steel based on experimental material characterization tests: Engineering Fracture Mechanics **333** (2026) 111788.

* Corresponding author. Tel.: +49 761 2714 435
E-mail address: andreas.heine@emi.fraunhofer.de

Light-Weight Armour for Defence & Security
LWAG 2026

Post-impact cavitation behind ballistic plates: experimental evidence and velocity threshold

H. Perruchot[a]*, O. Pennetier[a], J. L. Hanus[b], N. Prat[c], M. Arrigoni[d], A. Langlet[a]

[a]*LaMé - EA7494 - Univ. Orléans, Univ. Tours, INSA CVL, 63 av. de Lattre de Tassigny, 18020 Bourges, France*
[b]*LaMé - EA7494 - INSA CVL, Univ. Tours, Univ. Orléans, 88 Boulevard Lahitolle, 18000 Bourges, France*
[c] *IRBA – French Armed Forces Biomedical Research Institute, 91220 Brétigny sur Orge, France*
[d] *ENSTA - IPP- IRDL UMR 6027 CNRS, 2 rue François Verny, 29806 Brest Cedex 9, France*

Introduction

Light-weight ballistic protections are subjected to large deformations under projectile impact. Their performance is conventionally assessed through the Back Face Signature (BFS), which quantifies the residual deformation of the rear surface of the armour panel [1]. Although BFS has proven effective as a first-order criterion for blunt trauma risk, it does not capture the full mechanical response transmitted to the underlying biological tissues. Upon impact, a compressive stress wave propagates through the plate and into any contiguous fluid-filled biological structure — such as the thoracic cavity, the cerebrospinal fluid (CSF), or the abdominal contents [2]. This compression is followed by a pronounced transient pressure drop in the fluid.

When the local pressure falls below the vapour pressure of the fluid (for water $P_v \approx 2.3$ kPa at 20°C), cavitation may be triggered: vapour nuclei grow into macroscopic bubbles which subsequently collapse violently, releasing focused energy that can cause internal lesional damage independent of direct mechanical trauma [3,4]. This mechanism has received increasing attention in the context of blast-induced traumatic brain injury (TBI), where CSF cavitation has been identified as a potential secondary injury pathway [5,6]. However, experimental evidence of cavitation specifically induced by ballistic impact on protections remains scarce, and no velocity threshold has been established under controlled laboratory conditions.

The present study addresses this gap using a pneumatic launcher instrumented with pressure sensors and high-speed imaging. The objectives are: (i) to identify the impact velocity threshold beyond which post-impact cavitation occurs; (ii) to characterise the resulting pressure wave signatures; and (iii) to validate a Rayleigh-Plesset (RP) bubble dynamics model against experimental observations. These results support the introduction of the plate residual back-face velocity as a complementary criterion to BFS for assessing internal injury risk in ballistic protective systems.

Experimental setup

Experiments were carried out using a Thiot Ingenierie pneumatic launcher (velocity range: 10–190 m/s). A 12 mm diameter steel ball impacted a 2 mm thick, 150 × 150 mm² steel plate clamped over a rectangular open-top water tank. Impact velocity was recorded by a laser barrier system upstream of the target (cf. Figure 1). A total of 16 shots were performed across the velocity range 11.7–50.0 m/s.

A piezoelectric pressure sensor was embedded in the water volume behind the plate to record dynamic pressure histories at high sampling frequency. A high-speed camera provided direct visualisation of bubble nucleation, growth and collapse. Bubble radii were extracted from image sequences using a circular fitting algorithm and compared against model predictions. The cavitation threshold was identified through systematic analysis of both the pressure signal and the imaging data (visualisation of bubble formation).

* Corresponding author. Tel.: +33 6.70.91.49.84
E-mail address: hugo.perruchot@univ-orleans.fr

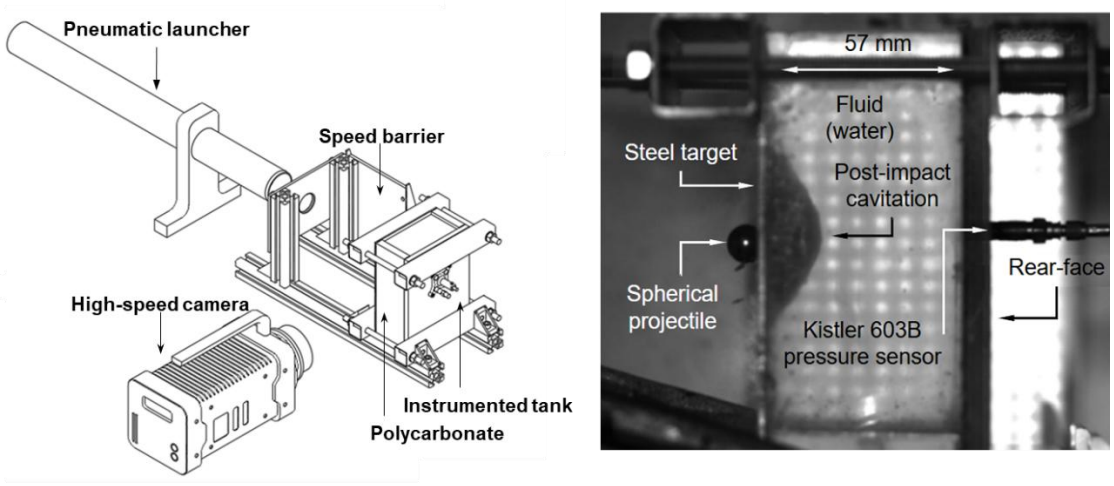

Figure 1. Left: Schematic of the experimental setup: pneumatic launcher, clamped steel plate, and instrumented water tank. Right: Experimental results.

Theoretical framework

The elastic rebound of the plate following impact is identified as the primary mechanism generating the tensile stress wave responsible for cavitation (cf. Figure 1). The plate deflects rapidly inward during impact, then springs back, creating a rarefaction wave that propagates into the fluid volume. This mechanism is consistent with the observations of Marsh & Bentil [5] for blast-induced CSF cavitation and is supported here by the temporal correlation between plate rebound and the onset of negative pressure in the sensor signal.

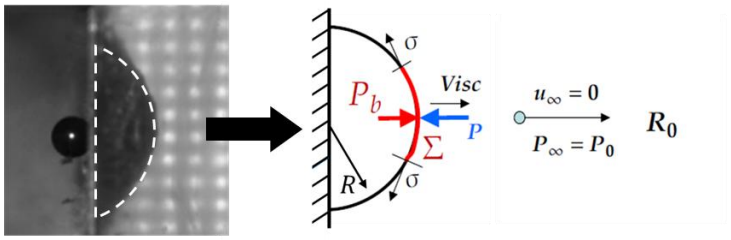

Figure 2. Diagram of a theoretical hemispherical bubble at the rear surface of the plate.

Due to the proximity of bubble nucleation to the plate rear surface, the bubble adopts a hemispherical geometry (cf. Figure 2). The equivalent spherical radius $\mathrm{R(t)}$ is used throughout, leaving the standard equation formally unchanged.

Applying a pressure balance on the bubble interface Σ (cf. Figure 2), accounting for surface tension σ and viscous dissipation μ, yields:

$$\Rightarrow \frac{P_b(t) - P(t)}{\rho} = R(t)\frac{d^2R(t)}{dt^2} + \frac{3}{2}\left(\frac{dR(t)}{dt}\right)^2 + \frac{4\mu}{R(t)}\frac{dR(t)}{dt} + \frac{2\sigma}{\rho R(t)}$$

where $\mathrm{P_b(t) = P_V + P_{g0}\left(\frac{R_0}{R(t)}\right)^{3\kappa}}$ is the total internal pressure, combining the vapour pressure $\mathrm{P_V}$ and the polytropic non-condensable gas contribution. Incorporating liquid inertia through the acceleration of the surrounding fluid, this reduces to the full Rayleigh-Plesset equation [7,8]:

$$\Rightarrow \frac{P_V - P(t)}{\rho} = R(t)\frac{d^2R(t)}{dt^2} + \frac{3}{2}\left(\frac{dR(t)}{dt}\right)^2 + \frac{4\mu}{R(t)}\frac{dR(t)}{dt} + \frac{2\sigma}{\rho R(t)} - \frac{P_{g0}}{\rho}\left(\frac{R_0}{R(t)}\right)^{3\kappa}$$

where $\rho = 1000\ \mathrm{kg/m^3}$ is the liquid density, $\sigma = 0.0728\ \mathrm{N/m}$ the surface tension, and $\mu = 0.001\ \mathrm{Pa.s}$ the dynamic viscosity. The far-field pressure is taken as constant and equal to atmospheric pressure (100 kPa).

The initial nucleus radius $\mathrm{R_0}$ is the sole fitting parameter, adjusted to match the experimentally observed bubble lifetime. Once $\mathrm{R_0}$ is determined, the model predicts the full temporal evolution $\mathrm{R(t)}$ and the maximum radius $\mathrm{R_{max}}$, which can be compared directly to high-speed imaging measurements.

Results and discussion

Table 1 summarises the key pressure metrics for all 10 shots in which cavitation was observed. The peak impact pressure $\mathbf{P_{impact}}$ increases monotonically with impact velocity, following a quasi-linear trend, consistent with linear acoustic propagation theory for the moderate velocity range investigated. The negative impulse $\mathbf{I^-}$ defined as the time-integral of pressure below the cavitation threshold ($P_V = 2.3 \cdot 10^{-3}$ MPa), similarly increases with velocity, quantifying the energy available for bubble nucleation and growth. It should however be noted that $\mathbf{I^-}$ is sensitive to signal noise and should therefore be interpreted as a qualitative trend. The time spent below threshold t_{sub} and the maximum bubble radius R_{max} follow the same trend, confirming the physical consistency of the dataset.

Shot	v (m/s)	P_{impact} (MPa)	P_{impl} (MPa)	Ratio (%)	I^- (MPa·ms)	t_{sub} (ms)	R_{max} (mm)
01	50.00	1.646	0.506	30.7	0.220	1.496	15.49
02	40.30	1.413	0.292	20.7	0.168	1.198	12.51
03	36.50	1.230	0.253	20.6	0.174	1.288	12.93
04	20.16	0.803	0.233	29.1	0.081	0.907	6.89
05	19.23	0.718	0.284	39.6	0.149	2.115	7.71
06	18.94	0.635	0.263	41.3	0.134	1.978	8.05
07	17.18	0.687	0.189	27.6	0.144	2.120	7.06
08	16.39	0.689	0.099	14.3	0.109	2.299	6.63
09	15.92	0.667	0.181	27.1	0.126	2.204	6.39
10	12.89	0.533	0.118	22.2	0.114	2.372	5.26

Table 1. Summary of pressure metrics and bubble characteristics for all shots with observed cavitation.

The pressure ratio P_{impl}/P_{impact} ranges from 14.3% to 41.3% with no clear monotonic trend with velocity. This behaviour is attributed to the non-linear nature of bubble collapse dynamics: the collapse intensity is a complex function of R_{max}, the confinement geometry, and the local pressure field at the moment of implosion, rather than solely the initial impact velocity.

Among the 16 shots, cavitation was consistently absent for v < 13.8 m/s and consistently present for v > 16.4 m/s. A transition zone is identified between approximately 12.9 and 15.9 m/s, within which cavitation occurrence is not deterministic. This variability reflects the stochastic nature of nucleation, governed by the local population of dissolved gas micro-nuclei in the water [7]. The cavitation event observed at the lowest tested velocity (12.89 m/s, Shot 10) similarly points to the sensitivity of the threshold to water quality (dissolved gas content, preparation history).

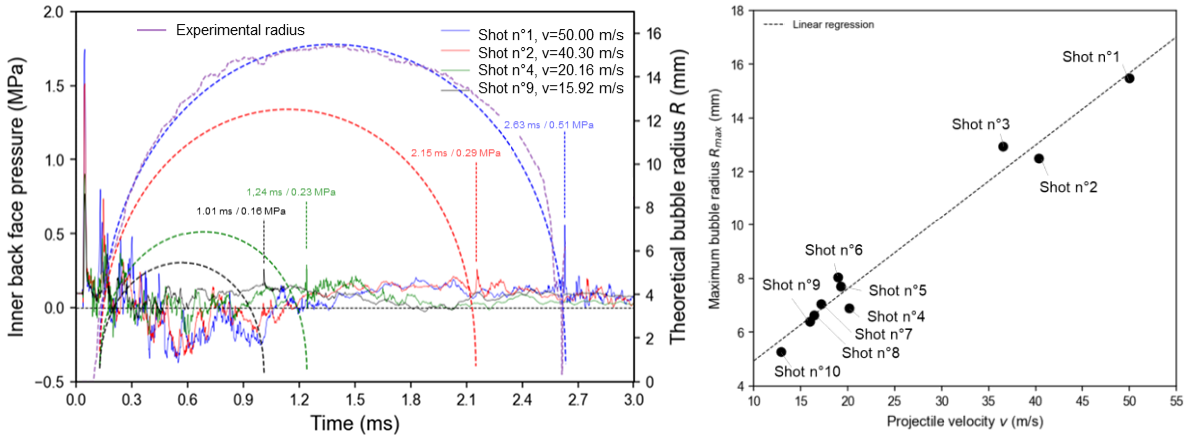

Figure 3. Comparison of RP model prediction and experimental R(t) for a representative shot (n°4). Right: R_{max} vs. impact velocity for all cavitating shots.

The Rayleigh-Plesset model, with R_0 fitted to match the experimental bubble lifetime, accurately reproduces the growth and collapse phases of the bubble as observed by high-speed imaging (cf. Figure 3). The predicted R_{max} values are in good agreement with measurements across the full velocity range (R_{max}= 5.26 –15.49 mm for v = 12.89–50.0 m/s).

Conclusion

This study provides experimental evidence of post-impact cavitation behind a 2 mm steel plate subjected to ballistic impact from a 12 mm steel ball. The stochastic transition zone (12.9–15.9 m/s) highlights the role of dissolved gas content in nucleation and suggests that a probabilistic rather than deterministic threshold is more appropriate — particularly relevant for biological fluids such as CSF, where gas concentrations vary between individuals [5]. Pressure analysis reveals quasi-linear scaling of $\mathbf{P_{impact}}$ and $\mathbf{I^{-}}$ with impact velocity, and the Rayleigh-Plesset model accurately reproduces measured bubble growth and collapse dynamics. These results support the use of plate back-face velocity as a complementary criterion to BFS for quantifying the risk of internal cavitation-induced injuries in the assessment of ballistic protective systems.

However, the main limitation of this study is the use of water as a biological surrogate, which lacks the viscoelastic response of living tissue. Future work will address these points through biologically relevant simulants and more representative impact geometries.

References

[1] Dancerel-Bourlon E, Delille R, Bourel B, Mauzac O, Prat N, Bir C, et al. Experimental and numerical replication of blunt ballistic impact on a male thorax surrogate: study of rib fractures and lung injuries predictions. Front Bioeng Biotechnol. 2025;13:1704069.

[2] Cannon L. Behind armour blunt trauma — an emerging problem. J R Army Med Corps. 2001;147(1):87–96.

[3] Lauterborn W, Ohl C-D. Cavitation bubble dynamics. Ultrasonics Sonochem. 1997;4(2):65–75.

[4] Goeller J, Wardlaw A, Treichler D, et al. Investigation of cavitation as a possible damage mechanism in blast-induced traumatic brain injury. J Neurotrauma. 2012;29(10):1970–1981.

[5] Marsh JL, Bentil SA. Cerebrospinal fluid cavitation as a mechanism of blast-induced traumatic brain injury: a review of current debates, methods, and findings. Front Neurol. 2021;12:626393.

[6] Salzar RS, Treichler D, Wardlaw A, et al. Experimental investigation of cavitation as a possible TBI injury mechanism in living populations exposed to blast. Ann Biomed Eng. 2017;45(10):2363–2373.

[7] Brennen CE. Cavitation and Bubble Dynamics. Cambridge University Press; 2013.

[8] Franc J-P, Michel J-M. Fundamentals of Cavitation. Fluid Mechanics and Its Applications, vol. 76. Springer; 2004.

Light-Weight Armour for Defence & Security
LWAG 2026

Ballistic performance of additively manufactured reaction bonded silicon carbide

Charlotte Iványi [a,*], Wouter van der Sluis [a], Dennis van Veen [a]

[a] TNO Platform Protection & Advanced Materials, Ypenburgse Boslaan 2, 2496 ZA Den Haag, Netherlands
* Corresponding author. Tel.: +31 6 27 91 57 44, *e-mail address:* charlotte.ivanyi@tno.nl

Introduction

Lightweight ceramic materials play a key role in modern ballistic protection systems. Additive manufacturing (AM) of ceramics is gaining interest in this context, as it enables mould-free production of complex geometries, large or curved components, and application-specific parts that are challenging or economically unfeasible to realise with conventional ceramic processing. Potential applications include curved vehicle and naval armour panels, large-area protective panels, and customised or modular personal protection systems.

The ballistic performance of additively manufactured ceramics has received limited attention in the literature and remains insufficiently characterised. One of the main reasons is that many additive manufacturing techniques are not capable of producing thick (≥ 6 mm), monolithic, near-fully dense ceramic components limiting their relevance for ballistic applications. As a result, only a small number of processing routes are currently considered viable for such applications.

One of these routes is the combination of additive manufacturing with reaction bonding to produce reaction-bonded silicon carbide (RB-SiC). In this approach, binder jetting is first used to fabricate a thick, porous SiC preform. This preform is subsequently densified through a reaction-bonding step, in which molten silicon infiltrates the porous structure and reacts with carbon to form additional SiC. The final material consists of primary and secondary SiC phases, together with a residual silicon content of approximately 15%. While RB-SiC generally exhibits lower ballistic performance than fully sintered monolithic SiC, primarily due to the presence of residual silicon, it is already in use for personal protection systems due to its favourable balance between performance, manufacturability, and cost. The combination with binder jetting offers additional advantages in terms of scalability, large build volumes, and geometric freedom, without fundamentally altering the conventional reaction-bonding process.

In addition to RB-SiC, reaction-bonded materials combining SiC and B_4C are available. These materials aim to improve ballistic performance at equal areal density and are therefore also included in the present study.

At TNO, the ballistic performance of RB-SiC as a stand-alone ceramic material has not yet been systematically assessed. Previous experience is primarily based on RB-SiC integrated within complete armour solutions. The aim of the present work is therefore threefold:

- to place the ballistic performance of RB-SiC in perspective relative to fully sintered SiC and Al_2O_3 which are more commonly studied reference materials in armour research,
- to compare additively manufactured and conventionally manufactured RB-SiC,
- to compare the ballistic behaviour of various reaction-bonded material systems, namely RB-SiC and RB-B_4C-SiC.

Materials and methods

Materials

To address the objectives, a set of reaction-bonded ceramic materials was selected, including both conventionally manufactured (pressure-based slip casting) and additively manufactured variants. The material set consists of RB-SiC, for which both manufacturing routes were included, and an additively manufactured RB-B_4C-SiC as a second reaction-bonded system.

In addition, fully sintered SiC and Al_2O_3, previously characterised at TNO, were included as reference materials to provide a benchmark for ballistic performance relative to commonly used armour ceramics.

Material characterization

Material characterisation was performed prior to ballistic testing. Density was determined using the Archimedes method on fragments taken from multiple samples. Elastic properties were derived from ultrasonic sound-velocity measurements in combination with density and sample thickness. Vickers hardness measurements were conducted using a HV0.3 load, and fracture toughness was estimated using the Palmqvist indentation method.

For the reaction-bonded materials, density and elastic properties are measured as bulk material properties, whereas hardness and fracture toughness were determined specifically for the SiC phase only. Due to the multiphase nature of the material, phase-specific characterisation would in principle be required, but reliable measurements of the silicon phase were not feasible.

Ballistic testing

Ballistic testing was performed at the Laboratory for Ballistic Research (LBR) at TNO. The test programme was designed to evaluate both the V50 ballistic limit and the residual velocity and residual energy after perforation, enabling direct comparison between additively manufactured and conventionally manufactured RB materials, as well as with fully sintered SiC and Al_2O_3 reference data.

Two configurations were considered:

1. Ceramic with backing:
   - Ceramic tile bonded to a GFRP backing plate
   - Tests performed to determine V50
   - Additional residual velocity and residual energy measurements conducted at an impact velocity of 920 m/s
2. Ceramic without backing:
   - Bare ceramic tile
   - Impact velocity: 825 m/s
   - Used primarily for residual velocity and residual energy measurements

For all tests, the threat corresponds to an AP 7.62 x 51 mm projectile.The test setup is shown schematically in Figure 1.

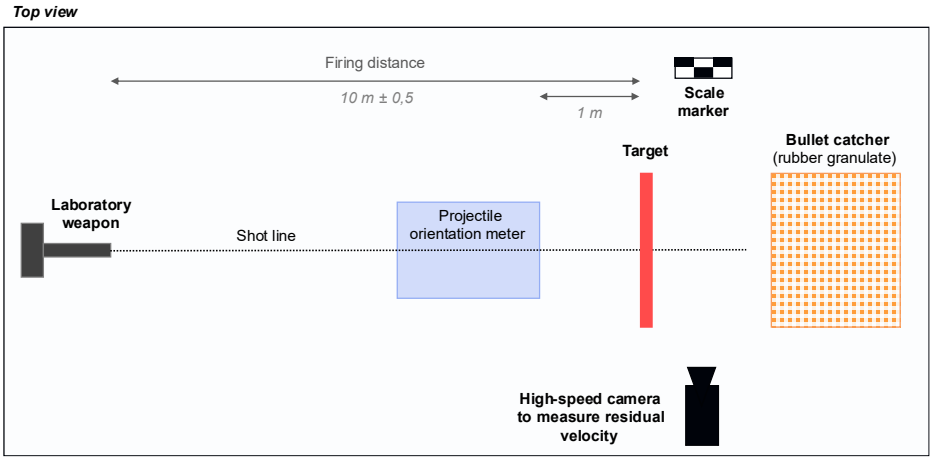

Figure 1: Top view of the ballistic test set-up.

Projectiles were launched using a laboratory gun, positioned at a distance of 10 m from the target. The target was mounted in a rigid support for the samples with backing and positioned loosely for samples without backing.

The impact velocity and projectile orientation were measured using a set of light-gate velocity sensors positioned 1 m in front of the target. In the case of yaw angle exceeding 3° shots were excluded from the analysis, as excessive yaw may influence penetration and introduce additional scatter in the ballistic results.

The rear side of the target was monitored using high-speed video (HSV) cameras, positioned to capture the ejection of debris and the dust cloud after perforation. The motion of this dust cloud was used to determine the residual velocity of the projectile in perforation cases. This method provides a reliable estimate of residual velocity, particularly when the projectile undergoes significant deformation or fragmentation.

Downrange of the target, a bullet-catching device was installed to enable the recovery of the projectile core, allowing determination of the residual projectile mass. The recovered mass is used in the residual energy analysis. The projectile jacket is excluded from this evaluation to specifically assess the ceramic's ability to blunt and erode the projectile core.

Results

Material characterisation

The results of the material characterization are summarized in Table 1. Overall, the additively manufactured RB-SiC showed no major deviations in key mechanical or structural properties compared to conventional material, supporting its further ballistic evaluation. Both RB materials exhibit typical reaction-bonded SiC morphologies, with the AM material showing slightly more clustering of residual silicon but no defects like porosity.

Table 1: Material properties of studied and reference materials.

	Studied materials				Reference materials	
	AM RB-SiC	**Conventional RB-SiC**	**AM RB-B_4C-SiC**	**Conventional RB-B_4C-SiC**	**SiC**	**Al_2O_3**
Density [g/cm^3]	3.07	3.08	2.91	2.85	3.18	3.88
Shear modulus [GPa]	158	176	161	165	188	147
Youngs modulus [GPa]	383	412	375	384	429	360
Vickers hardness [GPa]	28.9*	28.9*	n/a	n/a	n/a	n/a
Fracture toughness [MPa.m$^{1/2}$]	3.1*	3.2*	n/a	n/a	n/a	n/a
Composition [%]	85% SiC 15% Si	90% SiC 9% Si	51% SiC 34% B_4C 14% Si	51% SiC 38% B_4C 11% Si	>99% SiC	98% Al_2O_3

** Properties were determined for the SiC phase only*

Ballistic results to date

At the time of writing, ballistic testing has been completed for the additively manufactured RB-SiC material. Testing of conventionally manufactured RB-SiC, in identical configurations with and without backing, is planned but has not yet been completed.

The V50 of the AM RB-SiC was measured to be 733 m/s. For comparisson, fully sintered SiC with the same backing and areal density exhibits a V50 of 850 m/s. As expected, due to the presence of residual silicone in the materal, the RB-SiC material performs worse in terms of ballistic protection.

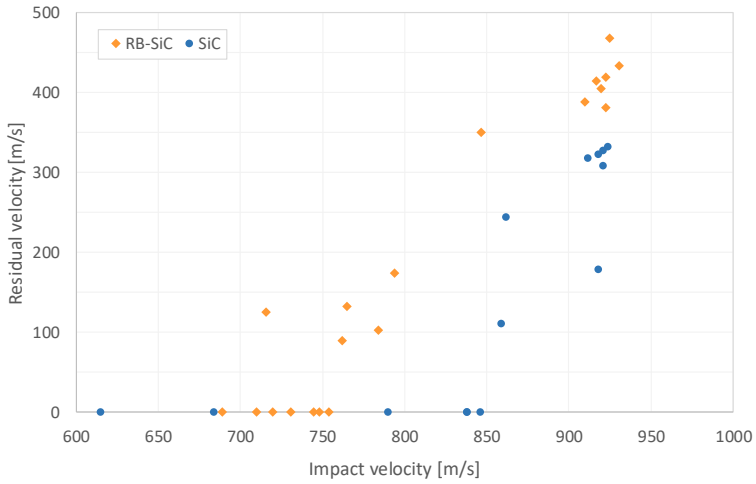

Figure 2: Residual velocity as a function of impact velocity for ceramic tiles tested with backing, comparing additively manufactured RB-SiC with fully sintered SiC at comparable areal density.

This difference is also reflected in the residual-velocity behaviour of perforated targets. The residual velocity data shown in Figure 2 shows that for backed configurations, RB-SiC reaches full perforation at lower impact velocities

and exhibits higher residual velocities compared to fully sintered SiC. This indicates a reduced energy absorption capacity of the RB-SiC material, consistent with the lower V50.

Nevertheless, the performance difference is considered workable. In specific applications, such as curved edges or geometrically complex regions of future composite military platforms, this difference may be compensated by locally increased thickness where a limited weight penalty is acceptable. A logical next step is to quantify the thickness increase required for RB-SiC to achieve equivalent ballistic protection to fully sintered SiC.

For the configuration without backing, residual velocities were measured and compared with reference data for fully sintered SiC and Al_2O_3. The results show that, in terms of residual velocity, the performance of RB-SiC lies between that of SiC and Al_2O_3, with the additively manufactured RB-SiC performing better than Al_2O_3. This is a positive result, as Al_2O_3 remains a widely used armour material, although it is increasingly replaced by SiC where feasible due to performance-to-weight considerations.

The RB-B_4C-SiC material shows a similar performance range to RB-SiC. No systematic difference in ballistic performance was observed between the two reaction-bonded materials in terms of residual velocity. At the time of writing, analysis of the residual energy, including post-processing of residual projectile mass data, is still ongoing and will be used to further assess potential performance differences.

Figure 3 shows the residual velocity as a function of impact velocity for all reaction-bonded materials and reference ceramics tested without backing, highlighting the position of the additivelly manufactured RB materials relative to conventionally used ceramics.

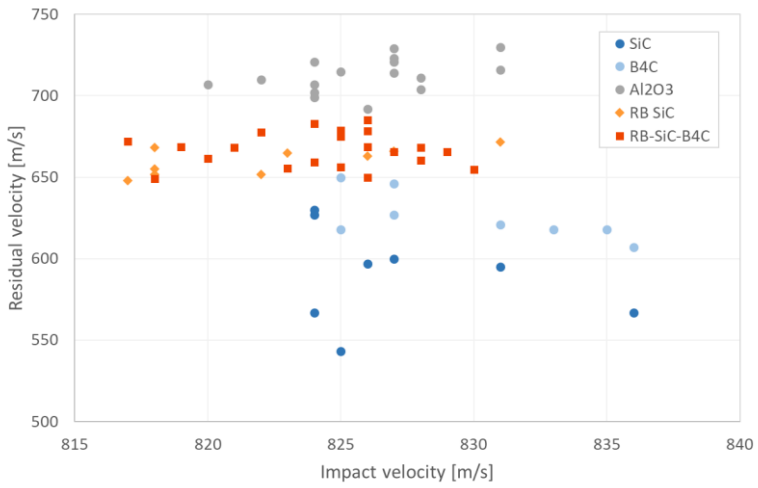

Figure 3: Residual velocity as a function of impact velocity for reaction-bonded ceramics and reference materials tested without backing at comparable areal density.

Conclusion

This work provides an initial assessment of the ballistic performance of additively manufactured reaction-bonded ceramics. The results indicate that these materials exhibit competitive ballistic behaviour when positioned relative to commonly used reference ceramics. However, the study is still ongoing and several open questions remain. In particular, ballistic testing of conventionally manufactured reaction-bonded ceramics is planned to isolate any effect of the additive manufacturing route. In addition, new questions emerging from the current results, such as the influence of B_4C addition on ballistic performance at equal areal density, require further investigation.

Light-Weight Armour for Defence & Security
LWAG 2026

Additively Manufactured Cellular Structures for Enhanced Blast and Ballistic Protection

Kappe Konstantin[a]*, Aron Pfaff[a]

[a]*Fraunhofer Institute for High-Speed Dynamics, Ernst-Mach-Institut, EMI, Freiburg, Germany*

Extended Abstract

For the last years, lightweight cellular structures, including honeycombs, foams, and lattices have gained notable attention [1]. These structures possess impressive mechanical properties under compression, such as increased specific strength and stiffness, as well as excellent energy absorption capabilities [2]. They find applications in dynamic load scenarios, such as crash, impact, or blast mitigation. However, the fabrication of geometrically defined lattice structures is challenging. In this context, additive manufacturing advancements offer opportunities to create complex structures with new materials and tailored properties, enhancing the mechanical properties of cellular structures [3, 4].

However, due to the various possibilities for geometries, arrangements, and dimensions of unit cells, finding an optimal design for different requirements can be challenging and time-consuming [5]. In particular, designing a cellular structure that performs effectively under multiple loading scenarios, such as for blast mitigation and ballistic protection, is difficult because these scenarios impose fundamentally different demands on the structure and involve distinct physical mechanisms. While blast loading typically applies a more distributed load to a sandwich structure, with energy being absorbed primarily through the plastic deformation of the cellular core, ballistic impact is far more localized and different mechanisms occurs, including plastic deformation and failure of the cell walls as well as fragmentation of the projectile core by asymmetric loading conditions.

The dynamic response of sandwich structures under blast loading has been widely studied analytically [6, 7], numerically [8–10], and experimentally [8, 11], yet only limited work has addressed the systematic optimization of their geometric properties. Due to the large design space of possible cell topologies and lattice configurations, identifying optimal solutions is highly complex and computationally demanding. Efficient numerical optimization methods are therefore essential. However, the strong geometric and material nonlinearities involved make gradient-based approaches unsuitable, and parameterized finite-element (FE)-based optimization often requires many costly dynamic simulations. Surrogate modeling techniques, such as kriging, response surfaces, or neural networks, offer a way to approximate the design space with far fewer simulations [12–14] and can be combined with evolutionary algorithms to search for optimal configurations [15]. For example, in [16] a neural-network surrogate model is used to optimize aluminum foam-core panels under blast loading. While foam density can be varied easily using homogenized material models, lattice structures pose greater challenges, as parameterizing different geometries and generating corresponding FE models requires substantial effort. To address this, Taguchi-based design-of-experiments approaches have therefore been used in [17] to identify influential geometric and material parameters for improving the blast resistance of auxetic lattice-core structures.

However, the ballistic behavior of cellular structures is far less explored in the literature and often limited to academic studies. Existing work shows that auxetic honeycombs can outperform conventional honeycombs and foams at moderate impact velocities (up to 600 m/s) due to their characteristic deformation mechanisms [18, 19]. Ballistic performance is influenced by multiple parameters such as projectile shape, velocity, and geometric

* Corresponding author. Tel.: +49 (761) 2714 – 587
E-mail address: konstantin.kappe@emi.fraunhofer.de

parameters of the sandwich structures (e.g., plate and core thickness, core relative density). Some studies investigate cellular cores in sandwich configurations, where the lattice mainly supports the front plate and leads to modest performance gains, cf. Ref. [20]. More recent studies have focused on the numerical and experimental investigation of the ballistic performance of different cellular topologies under projectile impact loading according to STANAG 4569 Level 2, see [21]. Therefore, the samples are additively manufactured using Maraging M300 steel. Significant differences for the topologies could be observed and different failure mechanisms, like fragmentation of the projectile core could be identified. However, a significant lower ballistic performance is achieved in comparison to a monolithic plate using the identical material. Furthermore, a major influence on the residual velocity caused by the impact position is identified. Additional research examines multi-material or polymer-filled lattices, which can further enhance ballistic resistance, but may negatively affect compressive performance relevant for blast loading [22–25].

In this study, cellular structures are investigated as the core of a sandwich structure intended to improve protection against both blast and ballistic threats. Yet, it is evident that the structural requirements differ significantly between these two scenarios. For blast mitigation, the energy of the explosion is primarily absorbed through the plastic deformation of filigree structural features, such as struts. In ballistic scenarios, however, the fragmentation of the projectile core is particularly beneficial, a process that filigree structures influence only minimally. Thus, the optimization of cellular structures with respect to blast loading is presented. The optimized samples are additively manufactured from 30CrMoNb5-2 steel and experimentally investigated in a small-scale explosive-driven shock tube. Subsequently, modifications to the cellular designs are proposed to also enhance their ballistic performance, by adding solid elements to ensure fragmentation of the projectile core.

Optimization for blast mitigation

A novel design and optimization framework for graded cellular lattice structures as core of a sandwich structure subjected to blast loading is introduced. The design framework can be divided into the following steps:

1. Cellular topologies are selected based on literature review and their compressive properties are analyzed over a wide range of relative densities. A typical compressive stress-strain curve is shown in Figure 1. The compressive behavior can be divided into (I) a linear elastic, (II) a plateau, and (III) a compression region. The plateau region is particularly interesting for energy absorption, and the plateau stress (1) and densification strain (2) can be described as a function of relative density using semi-empirical forms according to [2] and [26]. Further, the most promising cell structures are chosen for investigation in the blast loading, based on their load uniformity (3) and energy absorption capability (4).

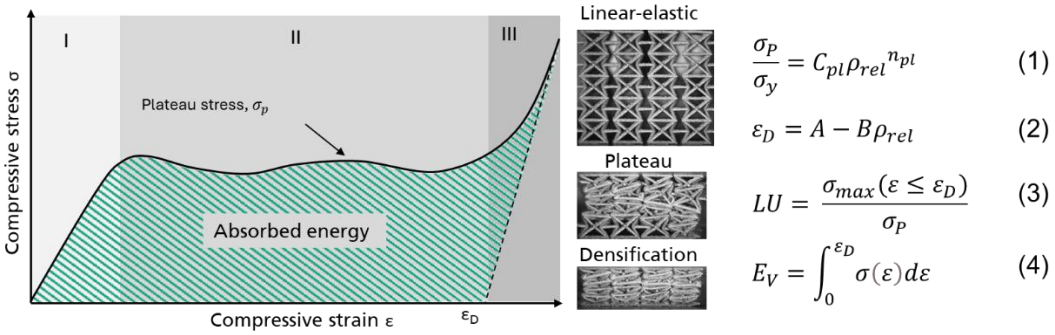

$$\frac{\sigma_P}{\sigma_y} = C_{pl}{\rho_{rel}}^{n_{pl}} \quad (1)$$

$$\varepsilon_D = A - B\rho_{rel} \quad (2)$$

$$LU = \frac{\sigma_{max}(\varepsilon \leq \varepsilon_D)}{\sigma_P} \quad (3)$$

$$E_V = \int_0^{\varepsilon_D} \sigma(\varepsilon) d\varepsilon \quad (4)$$

Figure 1 Typical compressive stress strain curve of a cellular structure and its characteristics properties.

2. To limit the design space for the detailed numerical optimization as much as possible, the relative densities of the cellular lattice core, for the EDST blast loading conditions, are determined using pre-dimensioning utilizing the conservation of energy and momentum. It is assumed that the reflected impulse of the blast load is fully transferred to the upper plate of the sandwich structure, causing its movement and the associated kinetic energy. This energy must be absorbed by the cellular core before densification arises. With the semi-empirical formulars for the plateau stress (1) and densification strain (2) the homogeneous relative density is determined.

3. A detailed numerical optimization is performed to improve performance through the introduction of a bi-linear gradient of the strut diameters. Therefore, a surrogate-based optimization procedure with an adaptive sampling strategy is utilized. Through a large number of validated, automized simulations, a

neural network is trained as a surrogate model and utilized for optimization with a genetic algorithm. The simulation model and optimization procedure is described in detail in [5].

The proposed framework is applied, and sandwich structures are optimized regarding the maximum transmitted force for a blast loading scenario, see Figure 1 a). For experimental testing, an explosive-driven shock tube (EDST) is utilized to generate a planar pressure front, which enables the investigation of the sandwich structures on a laboratory scale, see Figure 1 b). The structures, with a size of 60 x 60 x 40 mm³, are subjected to a reflected impulse and maximum overpressure of 2600 kPa·ms and 25000 kPa, respectively, which corresponds to an equivalent of approx. 3.9 kg TNT in 1 m distance of a hemispherical free field air-blast, corresponding to a scale distance of 0.64 m/kg$^{1/3}$.

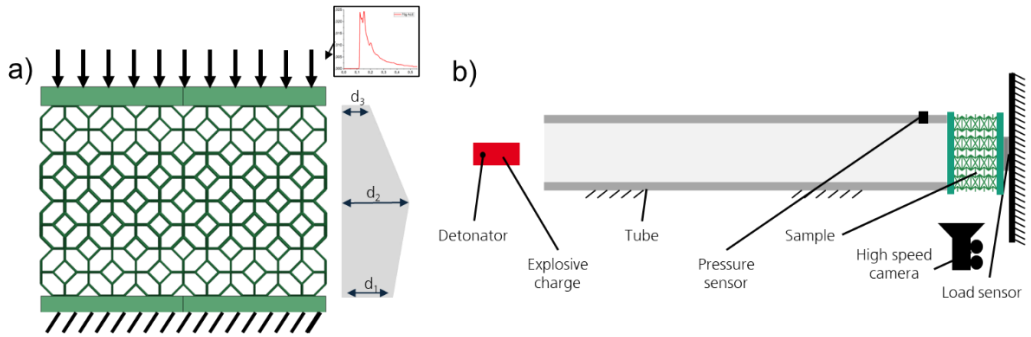

Figure 2 a) Optimization problem of a sandwich structure under blast loading with variables d_1, d_2 and d_3 with regard to the maximum transmitted force and b) optimized sandwich structure under blast loading in explosive-driven shock tube experiment (schematic).

The optimized structures are fabricated using 30CrMoNb5-2 steel powder (atomized Secure® 300 steel from Thyssenkrupp Steel Europe AG). In this fabrication process, the materials strength and failure strain are specially tailored to the requirements of the cellular structure in the laser powder bed fusion additive manufacturing process.

The optimized structures are tested in the EDST. The results of an optimized face centered cubic (FCC) cell topology are shown in Figure 3. The analytically defined preliminary design provided a solid starting point but tended to overestimate the necessary strut diameters due to the omission of e.g., rate-dependent hardening effects. The experimental results show good agreement with the predicted structural response form the detailed simulation-based optimization. However, deviations can be observed, in particular due to manufacturing inaccuracies of some geometries.

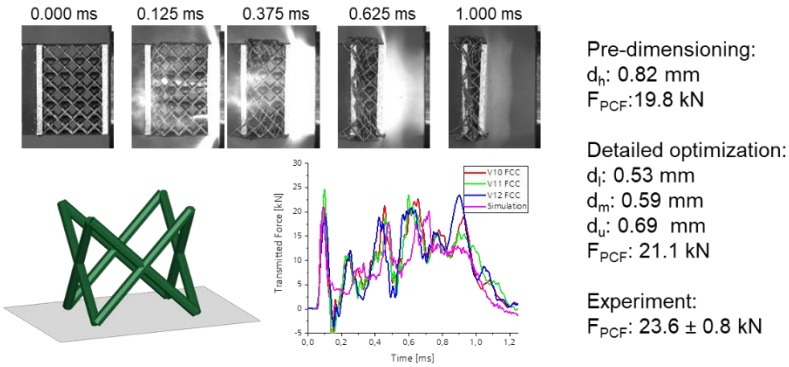

Figure 3 Response of an optimized sandwich structure with an FCC lattice core.

Enhancing the ballistic performance:

To increase the ballistic performance, solid structures are integrated into the cellular structure. These features are designed to achieve a fragmentation of the projectile core and thereby improve the overall ballistic resistance of the structure. The concept is illustrated schematically in Figure 4.

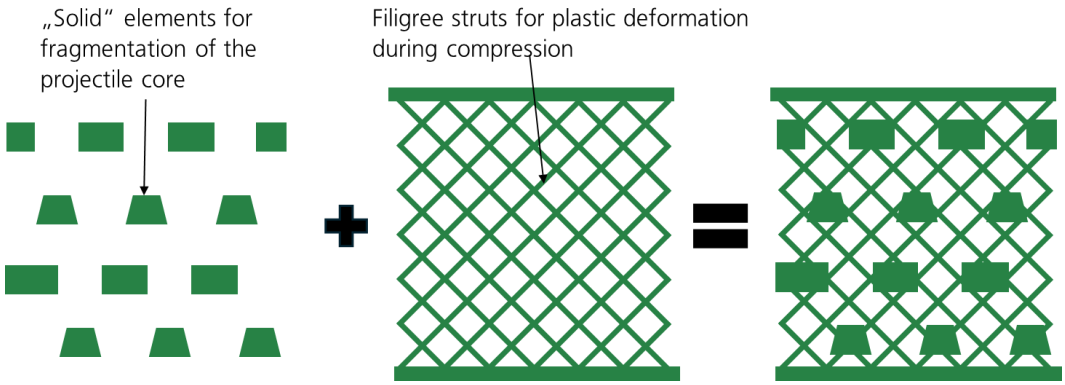

Figure 4: Solid elements integrated into cellular structures to enhance the ballistic performance by fragmentation of the projectile core.

The solid elements are positioned to minimally restrict compressive deformation while enhancing the likelihood of projectile-core fragmentation. Therefore, the position, size, and shape are determined through a parameter study using validated finite element simulations with the 7.62 × 39 mm AP BZ projectile according to Baranowski et al. and Burian et al. [21, 27] and an additively manufactured M300 steel lattice target based on [28]. The results indicate that rectangular cross-sections with a height of 4 mm and a width and lateral distance corresponding to the projectile core (~ 6.1 mm) are advantageous. Four layers of solid elements are introduced for fragmentation and compared with a mass-equivalent monolithic plate of the same material.

Since the fragmentation of the projectile and thus the ballistic performance in cellular structures is particularly dependent on the impact position this factor is taken into account. The residual velocity as a function of the initial velocity and relative position for the monolithic plate and the modified cellular structure are shown in Figure 5. A dependence of the ballistic limit velocity on the position is evident. However, it is observed that this performance varies, either better or worse, compared to the monolithic plate, depending on the impact position.

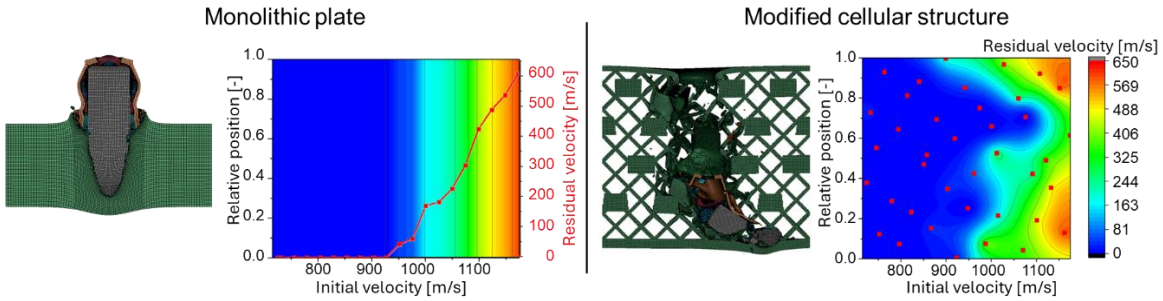

Figure 5 Residual velocity as a function of the initial velocity and relative position for the monolithic plate and the modified cellular structure for a ballistic impact with a 7.62 × 39 mm AP BZ projectile.

Conclusions:

The proposed concepts for lightweight protective structures demonstrate promising performance against both blast and ballistic threats. The following key conclusions can be drawn:

- The optimization strategy for blast loading introduces a novel and effective approach for designing cellular structures with advanced configurations. The optimized structures show good agreement between simulations and experiments.
- The integration of solid elements enables targeted tailoring of the structural response to meet the distinct requirements of blast and ballistic loading and can substantially improve ballistic resistance compared to conventional cellular architectures, as in [21].
- Numerical simulations indicate that the integrated-solid-element concept can achieve performance levels comparable to those of a monolithic plate. However, comprehensive ballistic experiments are required to validate these findings and enable a detailed evaluation.

References

[1] H. Altenbach und A. Öchsner, *Cellular and porous materials in structures and processes*. Wien, New York: Springer Verlag, 2010.

[2] L. J. Gibson und M. F. Ashby, *Cellular Solids: Structures and properties - Second edition*. Cambridge University Press, 2014.
[3] M. K. Thompson *et al.,* "Design for Additive Manufacturing: Trends, opportunities, considerations, and constraints", *CIRP Annals*, Jg. 65, Nr. 2, S. 737–760, 2016, doi: 10.1016/j.cirp.2016.05.004.
[4] A. Pfaff, M. Jäcklein, K. Hoschke und M. Wickert, "Designed Materials by Additive Manufacturing—Impact of Exposure Strategies and Parameters on Material Characteristics of AlSi10Mg Processed by Laser Beam Melting", *Metals*, Jg. 8, Nr. 7, S. 491, 2018, doi: 10.3390/met8070491.
[5] K. Kappe, K. Hoschke, W. Riedel und S. Hiermaier, "Multi-objective optimization of additive manufactured functionally graded lattice structures under impact", *International Journal of Impact Engineering*, S. 104789, 2023, doi: 10.1016/j.ijimpeng.2023.104789.
[6] A. G. Hanssen, L. Enstock und M. Langseth, "Close-range blast loading of aluminium foam panels", *International Journal of Impact Engineering*, Jg. 27, Nr. 6, S. 593–618, 2002, doi: 10.1016/S0734-743X(01)00155-5.
[7] M. Liang, Z. Li, F. Lu und X. Li, "Theoretical and numerical investigation of blast responses of continuous-density graded cellular materials", *Composite Structures*, Jg. 164, S. 170–179, 2017, doi: 10.1016/j.compstruct.2016.12.065.
[8] P. Pawlowski, M. Stanczak, P. Broniszewska-Wojdat, L. Blanc, T. Fras und A. Rusinek, "Energy-absorption capacity of additively manufactured AlSi10Mg cellular structures subjected to a blast-induced dynamic compression–experimental and numerical study", *International Journal of Impact Engineering*, Jg. 198, S. 105216, 2025, doi: 10.1016/j.ijimpeng.2024.105216.
[9] G. Imbalzano, S. Linforth, T. D. Ngo, P. V. S. Lee und P. Tran, "Blast resistance of auxetic and honeycomb sandwich panels: Comparisons and parametric designs", *Composite Structures*, Jg. 183, S. 242–261, 2018, doi: 10.1016/j.compstruct.2017.03.018.
[10] X. Lan, S. Feng, Q. Huang und T. Zhou, "Blast response of continuous-density graded cellular material based on the 3D Voronoi model", *Defence Technology*, Jg. 14, Nr. 5, S. 433–440, 2018, doi: 10.1016/j.dt.2018.06.003.
[11] M. Stanczak, T. Fras, L. Blanc, P. Pawlowski und A. Rusinek, "Blast-Induced Compression of a Thin-Walled Aluminum Honeycomb Structure—Experiment and Modeling", *Metals*, Jg. 9, Nr. 12, S. 1350, 2019, doi: 10.3390/met9121350.
[12] N. M. Patel, "Crashworthiness Design using Topology Optimization" Dissertation, Aerospace and Mechanical Engineering, University of Notre Dame, Notre Dame, Indiana, 2007.
[13] S. Koziel, D. E. Ciaurri und L. Leifsson, "Surrogate-Based Methods" in *Studies in Computational Intelligence, Computational Optimization, Methods and Algorithms*, J. Kacprzyk, S. Koziel und X.-S. Yang, Hg., Berlin, Heidelberg: Springer Berlin Heidelberg, 2011, S. 33–59, doi: 10.1007/978-3-642-20859-1_3.
[14] T. W. Simpson, J. D. Poplinski, P. N. Koch und J. K. Allen, "Metamodels for Computer-based Engineering Design: Survey and recommendations", *EWC*, Jg. 17, Nr. 2, S. 129–150, 2001, doi: 10.1007/PL00007198.
[15] J. Fang, G. Sun, N. Qiu, N. H. Kim und Q. Li, "On design optimization for structural crashworthiness and its state of the art", *Struct Multidisc Optim*, Jg. 55, Nr. 3, S. 1091–1119, 2017, doi: 10.1007/s00158-016-1579-y.
[16] C. Qi, S. Yang, L.-J. Yang, Z.-Y. Wei und Z.-H. Lu, "Blast resistance and multi-objective optimization of aluminum foam-cored sandwich panels", *Composite Structures*, Jg. 105, S. 45–57, 2013, doi: 10.1016/j.compstruct.2013.04.043.
[17] G. Imbalzano, P. Tran, P. V. Lee, D. Gunasegaram und T. D. Ngo, "Influences of Material and Geometry in the Performance of Auxetic Composite Structure under Blast Loading", *AMM*, Jg. 846, S. 476–481, 2016, doi: 10.4028/www.scientific.net/AMM.846.476.
[18] C. Qi, S. Yang, D. Wang und L.-J. Yang, "Ballistic resistance of honeycomb sandwich panels under in-plane high-velocity impact" (eng), *TheScientificWorldJournal*, Jg. 2013, S. 892781, 2013, doi: 10.1155/2013/892781.
[19] S. Yang, C. Qi, D. Wang, R. Gao, H. Hu und J. Shu, "A Comparative Study of Ballistic Resistance of Sandwich Panels with Aluminum Foam and Auxetic Honeycomb Cores", *Advances in Mechanical Engineering*, Jg. 5, S. 589216, 2013, doi: 10.1155/2013/589216.
[20] N. Novak, M. Vesenjak, G. Kennedy, N. Thadhani und Z. Ren, "Response of Chiral Auxetic Composite Sandwich Panel to Fragment Simulating Projectile Impact", *Physica Status Solidi (b)*, Jg. 257, Nr. 10, 2020, Art. no. 1900099, doi: 10.1002/pssb.201900099.
[21] P. Baranowski, M. Kucewicz, P. Płatek, K. Kappe, K. Cieplak und J. Małachowski, "Numerical and experimental evaluation of maraging steel cellular topologies for ballistic panel design", *International Journal of Impact Engineering*, Jg. 206, S. 105447, 2025, doi: 10.1016/j.ijimpeng.2025.105447.
[22] T. J. Daugherty, "Assessment of the ballistic performance of compositional and mesostructural functionally graded materials produced by additive manufacturing", *YOUNGSTOWN STATE UNIVERSITY*, Jg. 2020.
[23] A. Dmitruk *et al.,* "Experimental and Numerical Study of Ballistic Resistance of Composites Based on Sandwich Metallic Foams", *Appl Compos Mater*, Jg. 28, Nr. 6, S. 2021–2044, 2021, doi: 10.1007/s10443-021-09957-0.

[24] L. Zhao *et al.,* "Ballistic behaviors of injection-molded honeycomb composite", *J Mater Sci*, Jg. 53, Nr. 20, S. 14287–14298, 2018, doi: 10.1007/s10853-018-2611-y.
[25] C. J. Yungwirth, D. D. Radford, M. Aronson und H. N. Wadley, "Experiment assessment of the ballistic response of composite pyramidal lattice truss structures", *Composites Part B: Engineering*, Jg. 39, Nr. 3, S. 556–569, 2008, doi: 10.1016/j.compositesb.2007.02.029.
[26] M. I. Idris, T. Vodenitcharova und M. Hoffman, "Mechanical behaviour and energy absorption of closed-cell aluminium foam panels in uniaxial compression", *Materials Science and Engineering: A*, Jg. 517, 1-2, S. 37–45, 2009, doi: 10.1016/j.msea.2009.03.067.
[27] W. Burian *et al.,* "Protection effectiveness of perforated plates made of high strength steel", *International Journal of Impact Engineering*, Jg. 126, S. 27–39, 2019, doi: 10.1016/j.ijimpeng.2018.12.006.
[28] M. Edwards-Mowforth, M. Costas, M. Kristoffersen, F. Teixeira-Dias und T. Børvik, "On the ballistic perforation resistance of additively manufactured and wrought maraging steel: Experiments and numerical models", *International Journal of Impact Engineering*, Jg. 201, S. 105271, 2025, doi: 10.1016/j.ijimpeng.2025.105271.

Light-Weight Armour for Defence & Security
LWAG 2026

Transparent Polymer Armour: Influence of Ageing on the Protective Performance

Karl-Ludwig Krüger[a,b]1, Sebastian Engelbrecht[a], Vincent Pichot[a], Thomas Goepfert[a], Anthony Bracq[a], Nicolas Montmasson[a], Laurent Sinniger[a], Paul Beillard[a], Anne Jung[b]

[a]*French-German Research Institute of Saint-Louis, 5 rue de Général Cassagnou, Saint-Louis, 68300, France*
[b]*Helmut-Schmidt-University/ University of the Federal Armed Forces Hamburg, Holstenhofweg 85, Hamburg, 22043, Germany*

Extended Abstract

Transparent polymer laminates comprising polycarbonate (PC) and poly(methyl methacrylate) (PMMA) are critical for personal protective equipment (e.g. ballistic visors). For these multi-layered structures, mechanical integrity and optical clarity directly govern performance. Environmental exposure – elevated temperature, humidity, and UV radiation – induces hygrothermal and photo-oxidative ageing, degrading structural and optical properties [1-3].

This study correlates artificial ageing protocols with natural degradation kinetics to establish predictive accelerated – test models. The samples underwent hygrothermal cycling (70°C, 98 % RH) for up to 2000 hours, followed by non-destructive evaluation and quasi-static 4-point bending, acc. to ASTM D7264/ D7264M and ISO 14125. A quantitative comparison of the artificially aged samples, with natural aged visors was performed, regarding their ballistic performance. These naturally aged visors, reached their replacement time, after several years of in-service-life. The ballistic visors provide a protection-level IIIA, the ballistic tests were performed according to the NIJ0101.03 standard.

Two different configurations of quasi-static testing were chosen to test the multi-layered composite, this can be observed in Figure 1. Configuration A, shown in the left, represents the lengthwise alignment, where the delamination resistance of the adhesive is tested. Here, the force is applied parallel to the materials layered structure. On the right-hand side of Figure 1, the edgewise alignment for the 4-point bending test is shown. For this configuration the bulk material is tested, and the force is allied perpendicular across the layers. Key mechanical properties (flexural strength/ modulus) were quantified for different ageing durations.

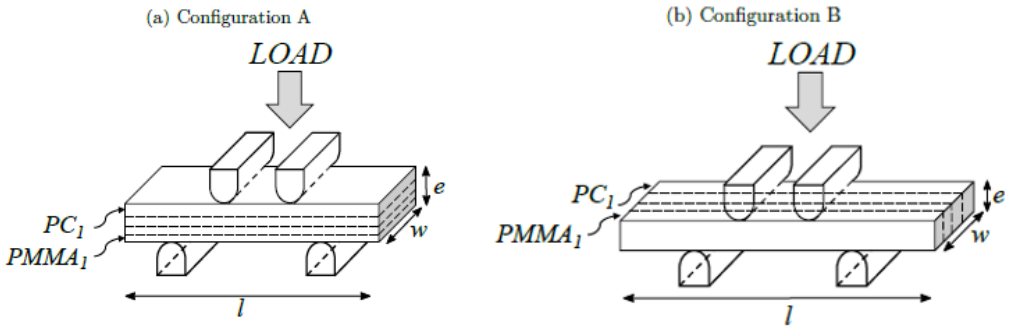

Figure 1: 4-point bending configurations: Lengthwise (A), Edgewise (B)

---

* Corresponding author. Tel.: +33 3 89 69 5992
E-mail address: Karl-Ludwig.Krueger@isl.eu

Figure 2 presents the stress-strain curves of the two different testing alignments, showing the unaged samples vs. after the longest ageing cycles, representative 70 °C at 98 % RH. Configuration A, where the adhesive layer is tested, the samples show a uniform behaviour, without huge influences due to ageing. Configuration B, shows

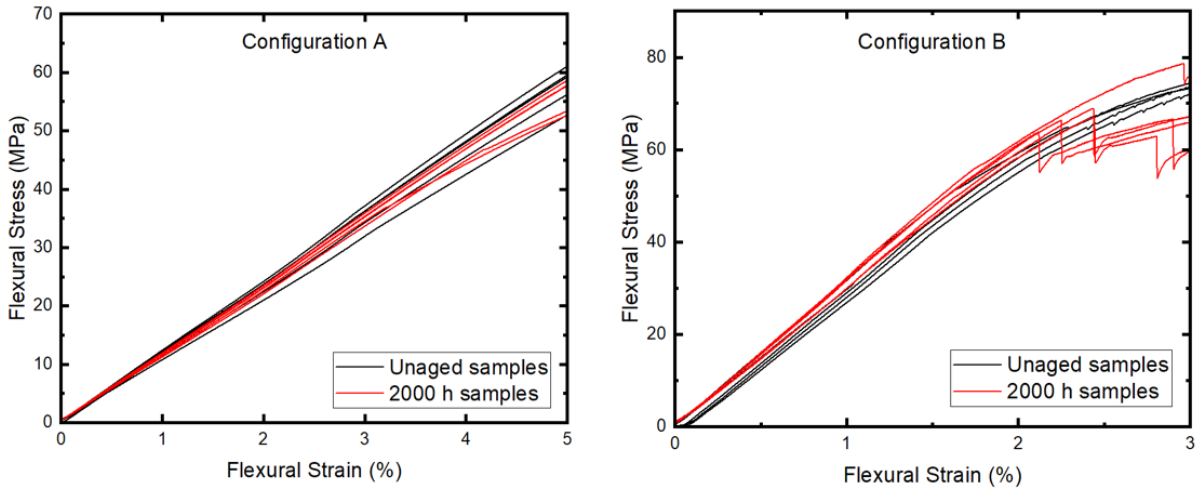

Figure 2: Stress/Strain curves- unaged versus 2000 h - Configuration A + B

a pronounced influence of ageing on the material, which results in a different breaking behaviour.

It became evident, that the ageing had an influence on the material, where the aged samples showed a breakage in the PMMA and PC layer, but in the unaged samples, a breaking of the PC was not observed.

Post-ageing, visors exhibited a misty/cloudy appearance, this behaviour is shown in Figure 3. It presents unaged visor on the left, showing a clear and transparent sample. The centre picture shows the same visor, directly after the ageing at high temperature and humidity condition. A strong misty appearance is evident, after the ageing time of 2000 hours. The right part of Figure 3 represents the visor after an extended amount of time after the ageing. The sample was stored at room temperature and room humidity. It shows, that the haze is still present after over a month of time. A weight gain ~ 1 % was measured for the visor samples, with their increasing ageing time.

Figure 3: Visor before ageing - left, directly after the ageing (70 °C, 98 % RH for 2000 h) - centre, over a month after the ageing cycle - right

Ballistics were performed in accordance to the NIJ0101.03 standard, therefore a 9x19 mm projectile was used in the tests. The ballistic test was supported by the use of digital image correlation (DIC).

Figure 4, presents the deformation of the artificial aged and the unaged visors. The red curves represent the aged samples, the black curves are presenting the unaged visor samples.

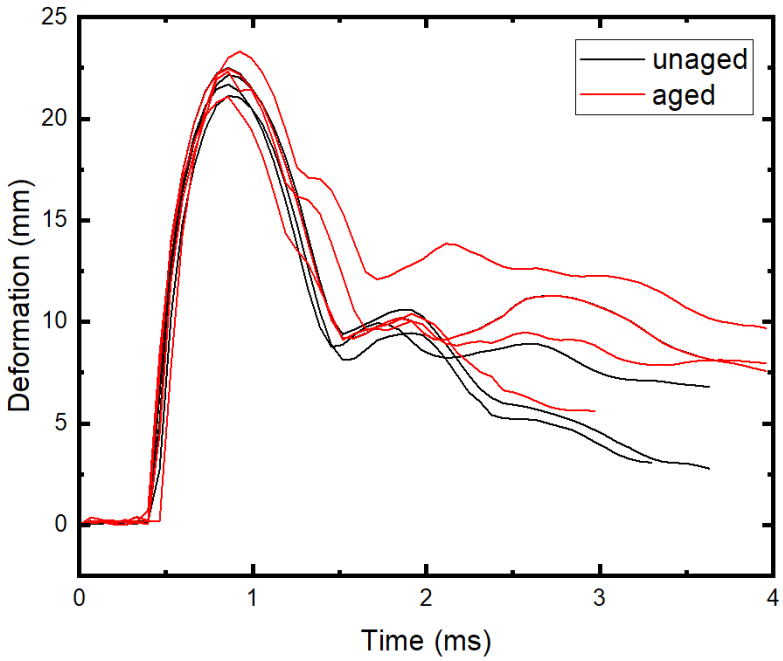

Figure 4: Deformation of aged/ non-aged visors

The total range of deformation for the artificially aged visors stretched from 20.4 mm to 21.8 mm. For the unaged samples the range of deformation spans from 21.1 mm to 22.5 mm. The red and black curves show a very similar deformation behaviour for either unaged and aged samples. All visors fulfilled their procurement requirements and were successful in stopping the projectiles.

After the tests, a careful post-mortem analysis of the visors has been performed. For all the visors, independent of their ageing condition, a delamination between the last PMMA layer and the PC backing layer occurred. Despite showing a similar picture for all the samples, aged and unaged, shown in Figure 4, it became clear that the breaking of the samples occurred only for the aged samples. A similar picture was shown in comparison to some naturally aged visors, which were used in service until they reached the end of their guarantied lifetime. The backside of the naturally aged visors showed similar cracks, as the artificially aged samples. These observations validate the artificial ageing approach, resulting in a breaking of the aged samples.

Here, harsh artificial conditions were used, to get a broader image of the ageing effects, different temperatures and adjusted humidity might have more insights on this topic.

References

[1] Swinarew et al, The Evaluation of Simulated Environmental Degradation of Polycarbonate Filled with Inorganic and Organic Reinforcements; Polymers 2021;13: 3572
[2] Liu et al, Characterization of Polymer Aging: A Review; Chinese J. Polym. Sci. 2024;42;1642-1660
[3] White et al, Polymer ageing: physics, chemisty or engineering? Time to reflect; ScienceDirect 2006; 9; 1396-1408

Light-Weight Armour for Defence & Security
LWAG 2026

Combining Photon Doppler Velocimetry and X-ray Tomography to Assess Ceramic Armour Performance

Thibaut Lemiere[a]*, Charles Francart[a], Pascal Forquin[a]

[a]*Univ. Grenoble Alpes, 3SR lab., Risk and vulnerabilites team, Grenoble, France*

Introduction

The increasing demand for lightweight, high-performance ballistic protection systems has driven significant research into advanced armor configurations combining ceramic strike faces with polymeric backing materials. Alumina (Al), Silicon carbide (SiC) and other technical ceramics have emerged as particularly attractive front-plate. However, the inherent brittleness of monolithic ceramics necessitates the integration of a compliant backing layer to provide structural support, absorb residual kinetic energy, and capture ceramic fragments during the ballistic event. Ultra-high molecular weight polyethylene (UHMWPE) composites have proven to be excellent backing materials, offering great specific energy absorption, high tensile strength, and superior multi-hit capability.

Material and Method

To evaluate the ballistic performance of the protection, we conducted controlled impact experiments using a multicaliber gas gun. The target specimen has been mounted in a sarcophagus positioned at the muzzle end of the barrel, ensuring repeatable alignment between the projectile and the target (Figure 1). The target configuration comprised a ceramic tile measuring 100mm x 100mm x 6mm (length x width x thickness) with a 100mm x 100mm x 15mm thick Dyneema® HB24 composite backing bonded to the rear surface of the tile using a structural epoxy.

We measured the residual velocities using a Heterodyne Velocimetry (HV) system, which provided continuous velocity profiles along the projectile's trajectory. We performed each test under the same conditions and systematically examined the post-impact specimens to assess damage patterns.

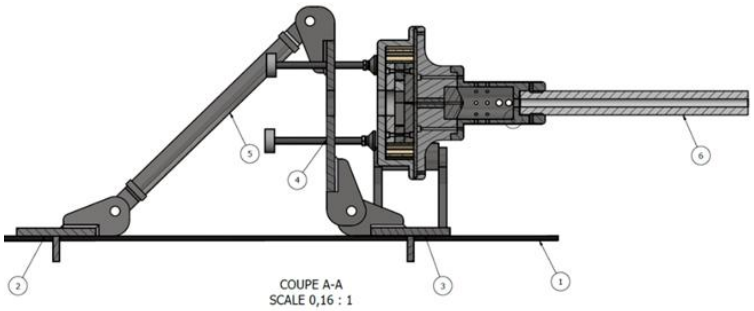

Figure 1: Overview of the ballistic impact assembly . (1-launcher frame, 2,3,4,5-chair, 6-nuzzle)..

Non destructive post-mortem analysis was further carried out using X-ray computed tomography (CT). A scan resolution of 50 µm (voxel size) was selected to accurately resolve crack patterns and enable three-dimensional segmentation of the fragments.

* Corresponding author. Tel.: +33 6 61 85 68 51
E-mail address: thibaut.lemiere@univ-grenoble-alpes.fr

The ceramics tested in this study are presented in Table 1. The experimental investigation was carried out on an F99.7 alumina, two grades of silicon carbide, Saint-Gobain SiC_1 and its coarse grain variant SiC_2, and a reaction-bonded boron carbide (RBBC) designated RBBC_1.

	Alumina F99.7	SiC_1	SiC_2	RBBC_1
Composition	AL_2O_3	α-SiC	α-SiC	SiC-B_4C-Si
Process	Natural sintering	Natural sintering	Natural sintering	Reactif sintering
ρ [kg/m³]	3900	~3100	~3100	~2800
E [GPa]	386	430	422	393
ν [-]	0,22	0,16	0,16	0,2
Cl [m/s]	10625	12057	11943	12470
	Homogeneous		Heterogeneous	

Table 1: Physical properties of tested materials ()

To ensure a robust comparison between microstructures, two or three repeated tests were performed under identical conditions for each material. The projectile used was an 7.62 API-BZ high strengh steel core, launched at an initial velocity of 960 m/s. The projectile was guided by a sabot, which was arrested before reaching the target by a sabot stopper.

Results and discussion

Measured velocities and displacements measurements obtained through HV setup are reported in Figure 2 for each test. Linear regression is applied to the signal's tail to extract the maximum deflection value.

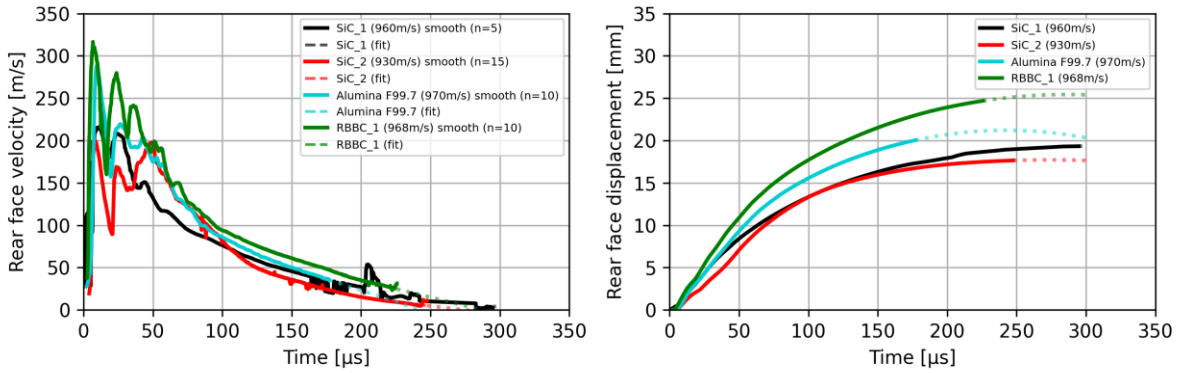

Figure 2: (left) Rear face velocity measured and smooth (right) Displacement computed from integrated velocity

Thanks to the sarcophagus each target can be retrieved and the final deflection can be measured. A springback effect (R) is observed, and a ratio between final deflection (Df) and maximum deflection (Dmax) can be computed (eq. 1).

$$R = 1 - \frac{D_{final}}{D_{max}} \quad (1)$$

When comparing these results (Figure 3) with ballistics tests conducted using Plastiline [1], the values are consistent with those reported in the literature with an average ratio egal 30%. This can be attributed to a springback effects (R). Furthermore, considering the maximum displacement as a performance index, SiC_2 can be considered the best protection, followed by SiC_1.

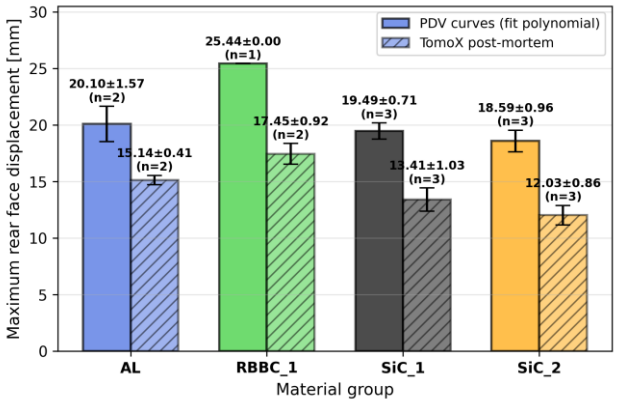

Figure 3: Comparison between measured maximum displacement and post mortem displacement

Further insights into these ballistics tests can be found in the fragmentation pattern. The most straightforward way to highlight differences in fragmentation is to plot the granulometric curve of the fragments (Figure 4.a). This is achieved by segmenting the CT scan of each ceramic sample using a Distance Transform 3D Watershed of the MorpholibJ plugin [2] in ImageJ software (Figure 4.b).

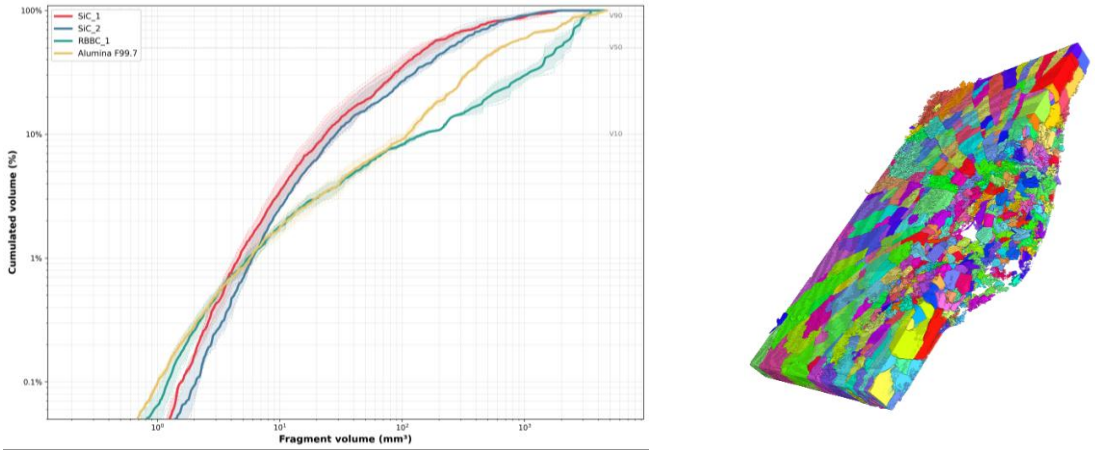

(a) (b)

Figure 4: (a) Granulometric study of the ceramic fragment and (b) Segmented CT scan of SiC_1

Preliminary observations suggest that sintered SiC (SiC_1 and SiC_2) grades display similar fragmentation behavior, generating predominantly smaller fragments compared to Alumina and Reaction Bounded (RBBC_1). This can be observed in their granulometric curves, which are consistently shifted toward lower fragment volumes. In contrast, Alumina and RBBC_1 exhibit a distribution skewed toward larger fragment volumes, indicating coarser fragmentation upon impact.

More detailed observations tend to dissociate the two sintered SiC (SiC_1 and SiC_2) grades. The spatial distribution of fragment size can be observed in Figure 5. SiC_1. Sintered SiC exhibits larger fragments in the regions away from the impact point,.

Alumina F99.7 and RBBC_1 both exhibit a spatial gradient in fragment size, with larger fragments concentrated at the top surface and smaller fragments toward the crater interior. However, this gradient is heterogeneous in RBBC_1, which displays localized zones of fine fragmentation at mid-depth, suggesting a more complex comminution pattern compared to the SiC_1 and SiC_2 ceramics. This heterogeneous fragmentation is consistent with the multiphasic nature and complex microstructure of Reaction Bounded (RBBC_1), in which differences in local mechanical properties between phases can promote preferential crack initiation and arrest, leading to Discountions spatially fragment size distributions.

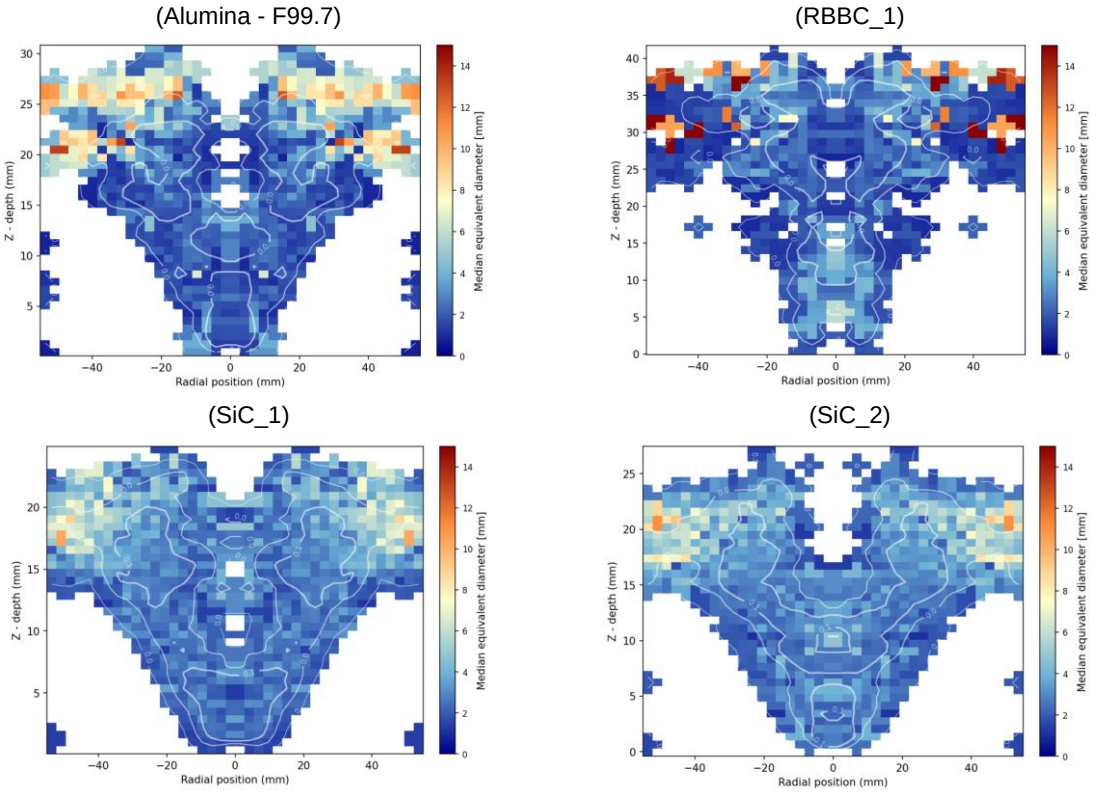

Figure 5: Average longitudinal section of the equivalent diameter obtained by angular scanning (72 planes).The horizontal axis represents the radial position relative to the impact axis (r=0), with r<0 and r>0 corresponding to the two opposite sides of the section plane.

Conclusion

The use of PDV (Photonic Doppler Velocimetry) in this ballistic test configuration provides new insights into the ballistic performance of ceramic armor. When combined with CT scan analysis, these results allow us to establish a link between the ceramic manufacturing process and fragmentation behavior, which may relate to ballistic performance. Sintered α-SiC (SiC_1 and SiC_2) appear to offer superior protection, particularly in single-hit configurations. Furthermore, reaction bounded tend to produce larger fragments in the impact zone (RBBC_1), which could be advantageous for multi-hit performance by preserving greater ceramic integrity between successive impacts. However, this relationship between ceramic manufacturing process, fragment size distribution, and multi-hit resistance remains an indirect inference from the present data, and dedicated ballistic multi-hit testing would be required to confirm this hypothesis.

Aknowledgement

This research received external funding from AID (Agence Innovation Défense). This support is gratefully acknowledged. The authors would like to acknowledge B. Bouteiller (Saint-Gobain company) for is useful comments.

References

[1] T. Camalet, “Caractérisation et modélisation du comportement dynamique des matériaux constituant une structure de protection céramique-composite,” 2020.

[2] Legland, D., Arganda-Carreras, I., & Andrey, P. (2016). MorphoLibJ: integrated library and plugins for mathematical morphology with ImageJ. Bioinformatics, 32(22), 3532-3534.

Light-Weight Armour for Defence & Security
LWAG 2026

Design of a Split-Hopkinson Pressure Bar System

P. Maleka[a]*, P. Mangoro[a], N. Singh[a] ,C.Du Preez[a]

[a]*Flamengro, a Division of Armscor SOC Ltd, 370 Nossob St, Erasmuskloof, Pretoria, 0048, South Africa*

Abstract

The Split Hopkinson Pressure Bar (SHPB) is a widely used experimental technique for characterising the dynamic mechanical response of materials at high strain rates. Commercial SHPB systems can be costly and may not offer the flexibility required for specialised research applications. This work presents the systematic design, development, and validation of an in-house SHPB system, emphasising design methodology, material selection, manufacturability, and experimental reliability. The developed system is intended to provide a cost-effective, modular, and repeatable platform for high-strain-rate testing of engineering materials for defence and security applications. This paper presents the methodology and engineering design of the Flamengro developed SHPB system, intended to support ballistic-relevant dynamic testing capabilities. The design process followed a systematic methodology encompassing requirements definition, numerical method which involved computational modelling of the system and the experimental method which consisted of a physical testing under controlled conditions. Particular emphasis was placed on achieving repeatable striker bar velocities and strain-rate control. Key design considerations included gas cannon configuration, bar material selection, bar length optimisation, instrumentation layout, and wave dispersion minimisation to ensure accurate stress–strain measurements. The SHPB system was designed to test light weight armour materials at a maximum striker bar velocity of 100m/s and a strain rate of 10 000 s^{-1}. The paper details the mechanical design employed to accurately capture incident, reflected, and transmitted stress waves. Validation of the system was conducted through baseline testing and comparison with theoretical predictions, demonstrating reliability and repeatability of the system.

Keywords: SHPB, dynamic testing, striker bar velocity, strain rate

1. Background

The need to understand material behaviour under extreme loading conditions has become increasingly important in modern engineering, particularly in defence and security applications where materials are subjected to high-velocity impacts and blast-type events. Under such conditions, materials experience very high strain rates, often exceeding $10^3 - 10^4\ s^{-1}$, and their mechanical response can differ significantly from quasi-static behaviour. Accurate characterisation of this dynamic response is therefore essential for the design and optimisation of protective systems such as lightweight armour, energy-absorbing structures, and impact-resistant components.

The Split Hopkinson Pressure Bar (SHPB) has emerged as a standard experimental technique for investigating material behaviour at high strain rates due to its ability to generate controlled stress waves and provide time-resolved measurements of stress, strain, and strain rate. Despite its widespread adoption, access to SHPB systems remains limited in many research and development facilities. Commercially available systems are often prohibitively expensive and typically designed as general-purpose platforms, offering limited flexibility for custom configurations required in specialised applications such as ballistic testing or novel material systems. In addition to cost constraints, many commercial SHPB systems do not readily accommodate iterative design modifications, integration with bespoke system, or adaptation to specific specimen geometries, bar material selection, instrumentation layout and loading conditions. For organisations engaged in advanced materials research, particularly in defence-related contexts, there is a need for a tailored experimental platform that can be adapted to

* Corresponding author. Tel.: +27 12 428 3169
E-mail address: pitso@flamengro.co.za

evolving testing requirements while maintaining levels of accuracy and repeatability. Consequently, the development of an in-house SHPB system presents a viable approach to overcoming the limitations associated with commercial alternatives. Such a system allows for a tailored design process aligned with specific research objectives, enabling enhanced control over key performance parameters, improved integration of customised measurement systems, and greater flexibility for iterative development. Additionally, in-house development offers potential cost reduction, design transparency, ease of maintenance, the ability to implement incremental improvements based on experimental feedback and facilitates a deeper understanding of system behaviour, which is essential for ensuring experimental reliability. In response to these limitations, the development of an in-house SHPB test bench enables full control over the design process, allowing the system to be purpose-built to meet specific performance targets, such as achieving striker velocities up to 100 m/s and strain rates of 10 000 s^{-1}.

2. Introduction

SHPB operates based on the principle of one-dimensional wave propagation and is widely used for testing the dynamic properties of materials at high strain rates. The apparatus is composed of several key components, gas cannon, striker bar, incident bar, transmission bar, and specimen to be tested.

In the SHPB setup, the striker bar is positioned within the barrel of the gas cannon, which is connected to a pressurised gas chamber. The striker bar, incident bar, and transmission bar are all made of the same material and have the same cross-sectional area to ensure uniformity and accurate measurements. A key requirement during the testing process is that all three bars must remain elastic throughout the test. The sample material under investigation is placed between the incident and transmission bars. The gas cannon propels the striker bar towards the incident bar with a high velocity. Upon impact, an elastic compression wave is generated and propagates through the incident bar towards the sample. When this wave reaches the sample, it interacts with the material, inducing plastic deformation as the stress exceeds the yield strength of the material. This interaction between the wave and the sample is crucial for characterising the material's behaviour under high strain rates.

At the interface between the sample and the transmission bar, part of the incident wave is transmitted through to the transmission bar, creating a transmitted pulse. Another portion of the wave is reflected back into the incident bar as a reflected pulse. To accurately measure the strain caused by these waves, strain gauges are attached to both the incident and transmission bars. These strain gauges are configured in a half Wheatstone bridge arrangement, which helps to mitigate the effects of bending and ensures that only the axial strain is measured. The elastic strains that occur in the incident and transmission bars, as a result of the transmitted and reflected pulses, provide the necessary data to calculate the stress-strain response of the sample. By analysing the signals from the strain gauges, the stress and strain experienced by the material can be determined, which is essential for understanding the material's behaviour under dynamic loading conditions, such as those encountered in high-speed impacts or rapid deformation events.

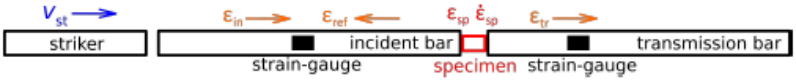

Figure 1: Schematic of the SHPB principle[1]

3. Split Hopkinson Pressure Bar Design

Flamengro's SHPB system was designed based on the requirements and specifications outlined in Table 1. The Hopkinson bar materials are varied depending on the test sample.

Table 1: Product design specifications

Design parameters	
Maximum strain rate	10 000 s^{-1}
Temperature range	Room temperature up to 400 ℃
Maximum striker bar velocity	100 m/s
Maximum tank pressure	16 bar
Tank volume	20 L

Barrel length	6 m, 4 m, 2 m
Barrel diameter	25 mm, 32 mm, 40 mm nominal bore
Specimen size	From ø 2 mm×2 mm up to ø 10 mm×10 mm
Hopkinson Bars dimensions	
Length of the experimental set-up	10 m
Length of striker bar	0.35 m, 0.5 m (ø20mm for all striker bar)
Length of incident bar	2 m, ø20 mm
Length of transmission bar	2 m, ø20 mm
Hopkinson Bars materials	
Material of striker bar	Maraging steel (350 grade)
Material of incident bar	Maraging steel (350 grade)
Material of transmission bar	Maraging steel (350 grade)
Material of specimen	Armox 500T

The following design requirements are met:

- The yield strength of the specimen must be less than the yield strength of the pressure bars.
- The incident bar should be at least twice as long as the striker bar, to avoid overlapping of the incident and reflected pulses.
- Furthermore, the mechanical impedances of the striker bar and the incident bar should be identical. Mismatched impedances may result in amplitude and profile changes of the generated pulse. If the striker bar impedance is higher, the unloading of the pulse into the incident bar will occur in a progressive way, and the generated stress wave will have various step amplitudes.
- Armox 500T was the chosen material for the specimen during the design phase to ensure that the system can accommodate a range of materials with lower impedance than Armox 500T.

3.1. Gas-gun and SHPB analytic model

The model of the exit velocity for a compressed air cannon was derived from various theoretical frameworks, including established models of gas expansion[2]. An existing study developed an analytic prediction model which is based on adiabatic process and on one-dimensional wave propagation theory in linear elastic cylindrical slender bars. The analytic prediction model was primarily used due its simplicity and efficiency, enabling researchers to estimate the key parameters of an SHPB test without the need for complex numerical simulations. By utilising the principles of wave propagation in slender bars and considering the effects of the gas-gun system, the model provides a valuable tool for understanding and optimising SHPB testing for a variety of materials under high-strain-rate conditions. This simplified approach can be particularly useful for rapid prototyping and preliminary testing when detailed numerical analyses are not feasible or necessary. It allows for the calculation of various parameters such as the velocity of the striker bar, strain rate of the specimen, the stress and strain waves within the incident and transmission bars, and the stress-strain relationship in the specimen under dynamic loading conditions.

The system was designed using the adiabatic model for the gas-gun system, with striker impact velocity calculated using the following equation[1]:

$$v_{st} = \sqrt{\frac{2}{m_{st}}\left\{\frac{C_P.P.V}{\gamma-1}\left[1-\left(\frac{V}{A_{st}.l_{bref}+V}\right)^{(\gamma-1)}\right]-F_f.l_{bref}\right\}} \quad [1]$$

The nominal strain rate in the specimen was determined from the striker bar velocity using the following relation[1]:

$$\dot{\varepsilon}_{sp} = \frac{2C_0\left(v_{st}.A_i.\rho.C_0.\beta - A_{sp}.\sigma_{sp} - A_{sp}.\sigma_{sp}.\beta\right)}{A_i.E.l_{sp}(1+\beta)} \quad [2]$$

The following design assumptions were made:

- The gas undergoes a rapid compression or expansion within the barrel.
- Adiabatic process (no heat is exchanged with the environment).
- The gas behaves ideally, following the equation of state for ideal gases.
- The process is isentropic (entropy remains constant throughout the compression and expansion phases).
- The barrel is considered to be seamless.
- The diameter of the striker bar within the barrel is considered to be equal to the diameter of the barrel.

3.2. Flamengro SHPB System

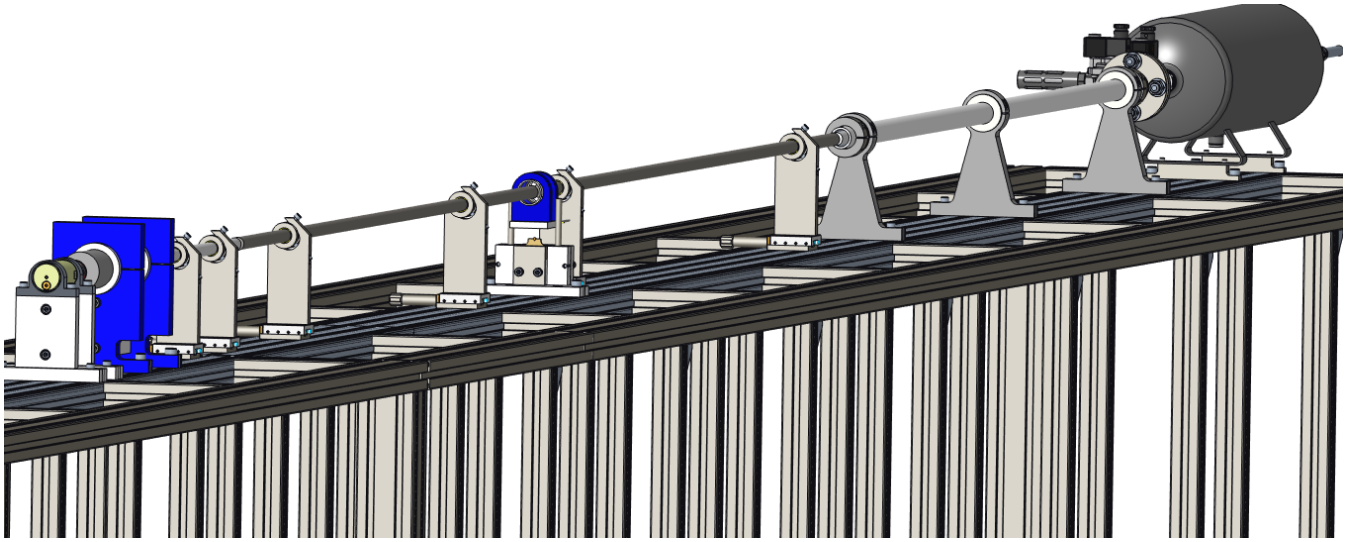

Figure 2:Flamengro SHPB test bench

4. Experimental Results

4.1. Gas Cannon Characterisation

The gas cannon was separately characterised where the system replicated the assumptions of the model. The results from Figure 3 show that the computational model followed the same general velocity–pressure trend observed in the HSV experimental data, demonstrating that the theoretical framework captured the fundamental behaviour of striker bar acceleration within the gas cannon system. Quantitative differences were observed across the tested pressure range. On average, the experimentally measured velocities were approximately $\pm$12% higher than the model predictions, with variability reflected by a standard deviation of approximately 0.12. According to the predefined evaluation criteria, these results indicate acceptable agreement between the model and experimental measurements.

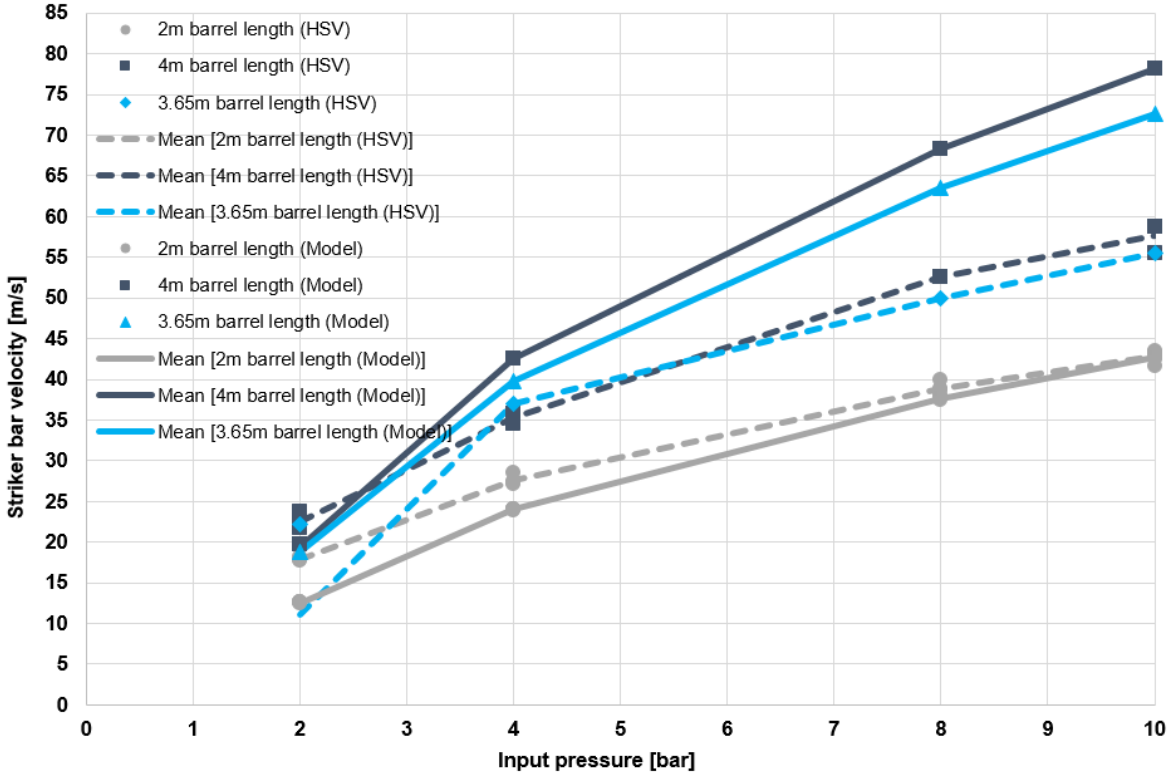

Figure 3: Striker bar velocity vs. input pressure for 50mm OD barrel with 350mm striker bar

4.2. SHPB Test

An SHPB test was conducted on a UNS C38500 Brass sample at different strain rates using IGUS SMWH Hard-Chromed bars. The samples, 6x6mm and 10x10mm, were tested at required strain rates of $3000s^{-1}$ and $2000s^{-1}$ respectively. In Table 2, an average of the experimental engineering strain rates was used.

Table 2: Comparison of model predictions and experiment

	Sample: 6x6mm P = 3.2 bar			**Sample: 10x10mm P = 3.0 bar**		
	Model	Experiment	Relative diff	Model	Experiment	Relative diff
$v_{st}\,[m/s]$	15.78	19.15	17.58%	14.98	18.75	20.11%
$\dot{\varepsilon}_{sp}[s^{-1}]$	2526.93	2763.77	8.57%	1325.11	1251.08	5.92%
$v_{st}[m/s]$	15.78	19.15	17.58%	14.98	18.37	18.45%
$\dot{\varepsilon}_{sp}[s^{-1}]$	2526.93	2849.29	11.31%	1325.11	1069.90	23.85%

The following properties were calculated for a sample of 10x10mm at a strain rate of $2000s^{-1}$ and the test results can be seen in Figure 4.

Table 3: Theoretical calculations of UNS C38500 Brass sample

Incident strain	1454 μm/mm
Reflected strain	-1289 μm/mm
Transmitted strain	167 μm/mm
Strain in the specimen	0.2575 mm/mm
Incident stress	305.39 MPa
Transmitted stress	35 MPa
Reflected stress	-270.39 MPa

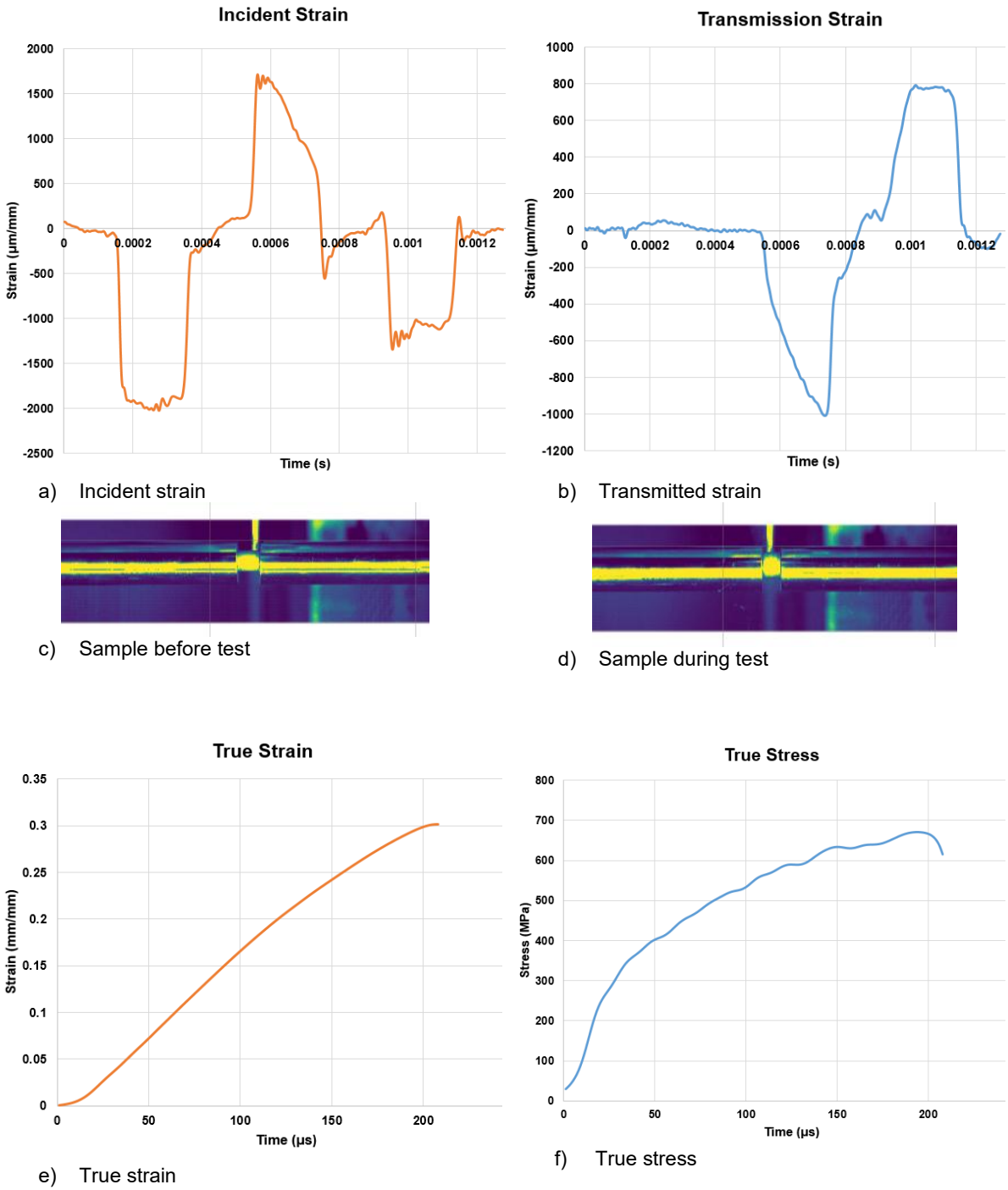

a) Incident strain

b) Transmitted strain

c) Sample before test

d) Sample during test

e) True strain

f) True stress

Figure 4: UNS C38500 Brass Test results

5. Conclusion

The system was designed using a numerical approach based on a theoretical adiabatic model, complemented by an experimental method in which preliminary tests were conducted to validate the model's predictions. The concept design adhered to the assumptions incorporated into the theoretical model to ensure consistency between analytical and experimental results. All mechanical components were designed within industry-recommended limits and are theoretically capable of meeting the performance requirements specified. The gas cannon is capable of generating the required striker bar velocity to achieve a maximum strain rate of 10,000 s^{-1}.

References

[1] “Split Hopkinson pressure bar: design parameters and prediction of the experiment output,” presented at the Engineering Mechanics 2018, May 2018, pp. 213–216. doi: 10.21495/91-8-213.
[2] Z. J. Rohrbach, T. R. Buresh, and M. J. Madsen, “Modeling the exit velocity of a compressed air cannon,” *American Journal of Physics*, vol. 80, no. 1, pp. 24–26, Jan. 2012, doi: 10.1119/1.3644253.

Light-Weight Armour for Defence & Security
LWAG 2026

Evaluating Steel Equivalence of Soft Ballistic Protection Materials through Finite Numerical Models

Manuel Fernandez-Melgosa[a]*, Ana Ferreira Azevedo[a], Frederik Coghe[a]

[a]*Royal Military Academy, Avenue de la Renaissance, Brussels, 1000, Belgium*

Abstract

Soft ballistic plates are flexible, multilayered protective inserts made from high strength synthetic fibers such as Aramid or UHMWPE, which are specifically designed to absorb and dissipate the kinetic energy of low velocity ballistic threats. These soft armor protections can be used either as primary protective elements or as backing layers combined with harder materials-such as ceramic or steel plates-to mitigate residual projectile energy and control armor deformation. However, the numerical modeling of soft ballistic plates is challenging due to the anisotropic behavior of the constitutive materials and the presence of specific failure mechanisms, including fiber breakage and delamination, all of which have an influence on the ballistic performance of the plates. In this study, a numerical investigation of a UHMWPE material (Dyneema®) soft ballistic laminates is carried out with the objective of developing an equivalent rigid target made of Armox® steel that can replicate the ballistic response of the soft panels. To achieve this, the LS-DYNA solver is employed to perform ballistic simulations on both Dyneema® laminates and Armox® steel plates impacted by different types of projectiles. The Dyneema® laminates are modeled as orthotropic materials, while the Armox® steel plates are described using the Johnson–Cook constitutive and failure models. The projectiles are treated as rigid bodies of known geometries. The expected outcomes of this work include determining the ballistic limit of both Dyneema® and Armox® plates as a function of projectile type and armor thickness, comparing the numerical results obtained off Armox® steel with analytical ballistic models available in the literature, and establishing an equivalent Armox® thickness capable of replicating the ballistic performance of the soft Dyneema® panels. The proposed equivalence approach aims to simplify armor design studies by replacing detailed soft-armor modeling with an equivalent rigid steel representation, thereby reducing computational effort while preserving predictive accuracy.

Introduction

Fiber-based fabrics and composite materials have been widely used in personal armour systems over the years, as they provide an effective alternative to traditional monolithic plates such as steel. These materials offer enhanced fragmentation and ballistic protection due to their high mass efficiency, making them ideal for preserving user mobility while maintaining protection. However, their inherent complexity makes them difficult to analyse both numerically and experimentally, owing to intricate failure mechanisms and the large number of material properties and failure parameters that must be characterised through extensive testing.

One possible approach to address this challenge is to assist in the design and selection of fiber-based fabrics and composite materials through the concept of monolithic equivalence. Although the failure modes in these materials differ significantly from those in monolithic systems, this approach can serve as a useful starting point in the personal armour design process. Establishing a monolithic equivalence may enable simpler experimental procedures and more efficient numerical modelling of orthotropic materials.

* Corresponding author. Tel.: +32 471586189
E-mail address: manuel.fernandezmelgosa@mil.be

Numerical setup

The numerical investigation was conducted on both the Dyneema® layers and the Armox® plate. For the characterization of Dyneema®, two types of projectiles were considered: a 1.1 g fragment simulating projectile (FSP) and a 1.05 g steel ball. Both penetrators were modelled as rigid bodies.

The Dyneema® layers were represented using solid elements with a single element through the thickness. In the FSP simulations, only half of the plate was modelled by applying a symmetry boundary condition (Figure 1a). The plate boundaries were fully constrained in both translation and rotation. Each Dyneema® layer was defined using *MAT_COMPOSITE_FAILURE (MAT059), with material properties taken from [1] and modified strength parameters to calibrate the numerical model against available experimental data. Element erosion was governed by the maximum equivalent effective strain at failure (EFEPS) implemented via the *ADD_EROSION card. Contact between the penetrator and the layers, as well as interlayer contact, was modelled using a single-surface eroding contact formulation. A segment-based penalty contact with pinball formulation and warped segment checking was employed (SOFT = 2, SBOPT = 3), with a DEPTH value of 5. Proper definition of symmetry and sliding options within the contact algorithm was found to be essential for accurate results.

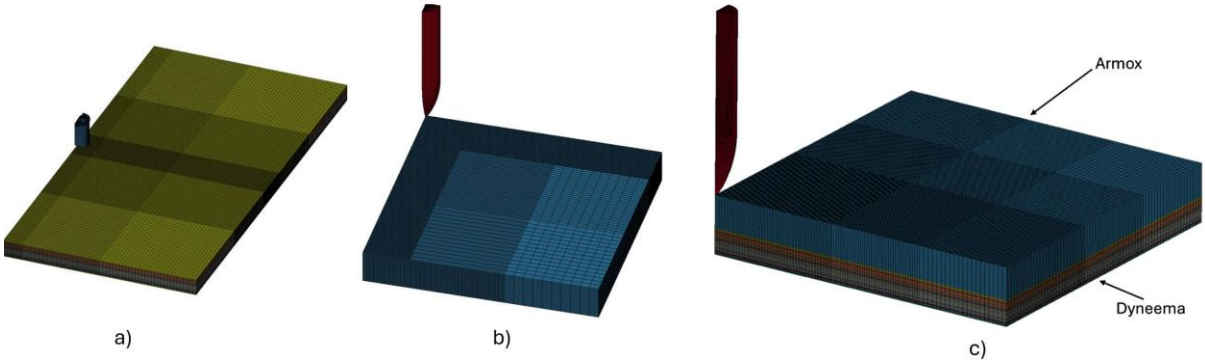

Figure 1: a) Dyneema® model with the FSP 1.1g; b) Armox® model with the 7.62x54R API and c) Armox® backed with Dyneema® layers with the 7.62x54R API.

The steel plate simulation (Fuigure 1b) was performed to determine the yield strength at high strain rates, enabling the application of the analytical model proposed by Lambert and Jonas (LJ model) and Rech and Ipson (RI model) [7]. The penetrator used in the simulations corresponds to the core of a 7.62 × 54R API projectile, consistent with the experimental work conducted by the Poland Military University (WAT) [6]. Due to the absence of significant erosion observed in the experiments, the projectile was modelled as a rigid body. The Armox® plate was modelled using the Johnson–Cook constitutive model, *MAT_JOHNSON_AND_COOK (MAT015), coupled with the Grüneisen equation of state (*EOS_GRUNEISEN), with material parameters obtained from the literature [2], [3], [4]. Contact between the penetrator and the plate was defined using a single-surface eroding contact formulation, employing the same algorithm and parameters as those used in the Dyneema® layer simulations. Option C in the contact definition was activated to allow the selection of a stable time step (DTSTIF) compatible with the speed of sound in steel and the minimum element size in the contact region. Additional simulation settings, including control contact parameters, were selected in accordance with recommendations from the literature

The final set of simulations consists of a ballistic study of an Armox® plate backed by Dyneema® layers (Figure 1c). Two Armox® thicknesses were considered, 5 mm and 7 mm, combined with Dyneema® laminates consisting of 10, 19, and 29 layers. The objective is to maintain a constant total thickness while evaluating the influence of different material distributions between Armox® and Dyneema® on ballistic performance. The penetrator used in all simulations is a 7.62×54R API projectile. The contact between the Armox® plate and the Dyneema® layers is modelled using an automatic single-surface contact formulation.

Results and Conclusions

First, the characterization of the Dyneema®® layers is discussed. Figure 2 represents the impact sequence of the FSP penetrating several layers of Dyneema®, close to the ballistic limit. Figure 3a presents the ballistic limit as a function of areal density for Dyneema® impacted by a 1.1 g FSP, showing good agreement with the experimental curve reported in [3]. Additionally, the ballistic limit of Dyneema® subjected to impact by a steel sphere shows an error of less than 10% compared to the experimental results provided by Patrik Appelgren from the Swedish Defence Research Agency (FOI)

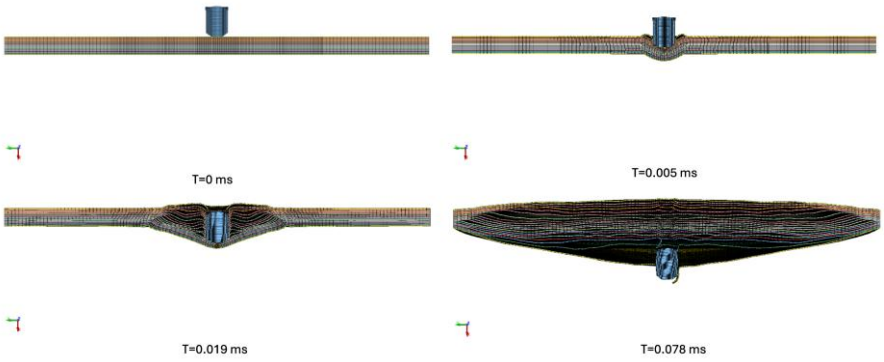

Figure 2: Sequence ilustrating the impact event of the FSP against 20 layers of Dyneema® at 590 m/s

The results of the Armox® characterization are presented in Figure 3 and Figure 4, showing good agreement with the experimental data reported in [6]. Figure 4 compares the numerical simulations with the analytical Lambert–Jonas model, constructed using the reported ballistic limit. A yield strength of 1.3 GPa at high strain rates was selected to achieve the best agreement with the experimental results. However, when compared with material data available in the literature, the model presented in [2] was found to overestimate the strength of the steel.

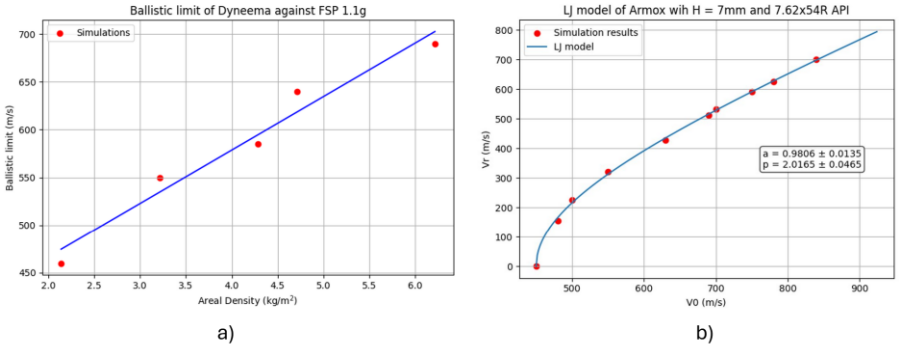

Figure 3: a) Ballistic limit as a function of the aerial density of the Dyneema®; b) Lambert and Jonas model with coefficients

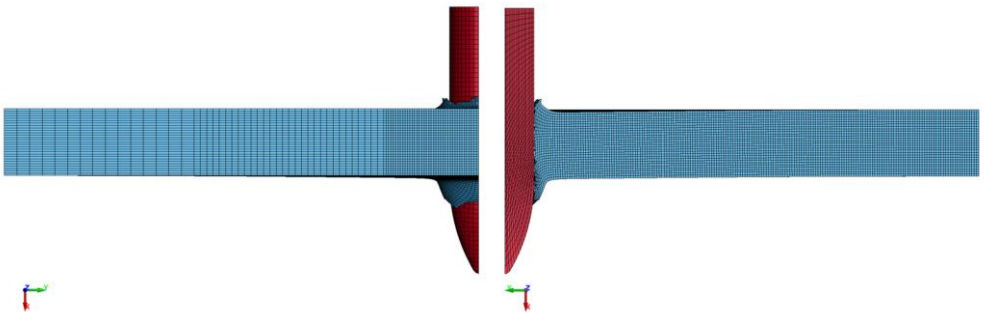

Figure 4: 7.62x54R API penetrating 7mm of Armox® at 650 m/s from the front (left) and the internal (right) view

The following results present the equivalent Armox® thickness required to match the impact response of a projectile against Dyneema® layers. Figure 5 shows a target with a total thickness of 9 mm subjected to a projectile impact at a velocity of 650 m/s. It can be observed that the failure mode of the Dyneema® layers differs between both cases; however, the failure mode of the Armox® plate remains almost unchanged.

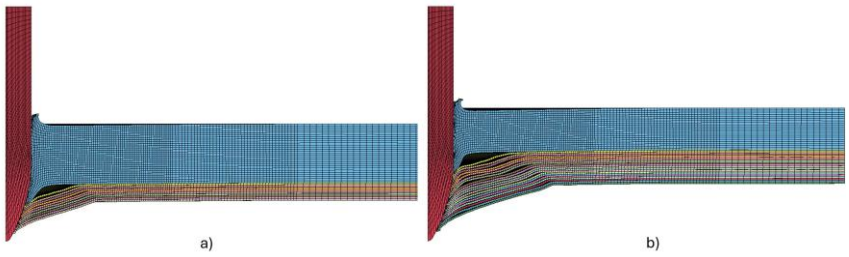

Figure 5: a) 7mm of Armox® and 2mm of Dyneema®; b) 5mm of Armox® and 4mm of Dyneema®

Figure 6 shows the residual velocity of Armox® plates backed with Dyneema® layers impacted at 650 m/s and the equivalent thickness. For each total thickness, two Armox® thicknesses and corresponding Dyneema® layer configurations are considered. As expected, increasing the number of Dyneema® layers reduces the residual velocity by 20–30m/s. This corresponds to an equivalent Armox® thickness of approximately 1 mm per 2 mm of Dyneema®, obtained using the Recht–Ipson (RI) ballistic limit model with the previously determined yield strength.

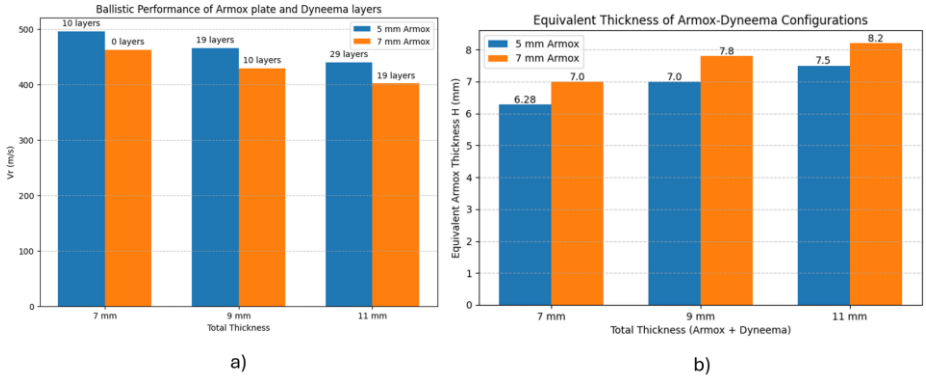

Figure 6: a) Residual velocity depending on Armox® and Dyneema® combination; b) Equivalent Armox® thickness depending on the Armox®-Dyneema® configuration

References

[1] Wu, K. K., Chen, Y. L., Yeh, J. N., Chen, W. L., & Lin, C. S. (2020). Ballistic Impact Performance of SiC Ceramic-Dyneema® Fiber Composite Materials. Advances in Materials Science and Engineering, 2020(1), 9457489.

[2] Paman, A., Sukumar, G., Ramakrishna, B., & Madhu, V. (2020). An optimization scheme for a multilayer armour module against 7.62 mm armour piercing projectile. International Journal of Protective Structures, 11(2), 185-208.

[3] van der Werff, H., & Heisserer, U. (2016). High-performance ballistic fibers: Ultra-high molecular weight polyethylene (UHMWPE). In Advanced fibrous composite materials for ballistic protection (pp. 71-107). Woodhead Publishing.

[4] Li, D., Huang, F., Ren, B., Zhang, W., Xiong, J., Zhou, B., & Guo, X. (2024). Ballistic analysis of high-performance armor steel by numerical simulation. Scientific Reports, 14(1), 11466.

[5] Skoglund, P., Nilsson, M., & Tjernberg, A. (2006, August). Fracture modelling of a high performance armour steel. In Journal de Physique IV (Proceedings) (Vol. 134, pp. 197-202). EDP science

[6] Fikus, B., Szupieriko, D., Kohnke, M., & Piasta, K. (2026). Comparison of the terminal ballistic efficiency of high hardness steels and titanium based alloys [Unpublished manuscript].

[7] Rosenberg, Z., & Dekel, E. (2020). Terminal ballistics (3rd ed.). Springer.

Light-Weight Armour for Defence & Security
LWAG 2026

Finite Element Analysis of Ballistic Resistance Performance Degradation in Damaged Small Arms Protective Inserts

Massimo Di Fulvio, Luca Lomazzi, Andrea Manes*

Politecnico Di Milano, Department of Mechanical Engineering, Via la Masa 1, Milan, 20156, Italy

Extended Abstract

Introduction

Modern personal ballistic protection systems, particularly Small Arms Protective Inserts (SAPIs), are designed to defeat small and medium calibre threats while maintaining low weight and high mobility. Current advanced composite armours rely on a multi-layer architecture composed of a hard ceramic strike face backed by a ductile composite laminate. This configuration ensures high energy absorption efficiency and favourable strength-to-weight ratio.

Despite their excellent nominal ballistic resistance, SAPIs are vulnerable to multiple ballistic hits or off-design events. Low-velocity impacts and improper handling can generate barely visible impact damage (BVID) or hidden internal damage within the ceramic tile or the composite backing. Because ceramic materials exhibit complex brittle fracture mechanisms and stochastic crack propagation, evaluating the residual ballistic performance of a damaged SAPI remains an open and critical problem.

The primary objective of this work is to develop and validate a high-fidelity finite element (FE) modelling framework capable of accurately reproducing the ballistic response of an undamaged ceramic composite SAPI, quantifying performance degradation due to prior ballistic impact and assessing the influence of a pre-existing through-thickness crack in the ceramic layer. The final goal is to provide a predictive numerical methodology that supports quantitative prognosis of damaged ballistic protections.

Numerical model description

The numerical and experimental tests of a composite SAPI subjected to the ballistic impact of a 7.62 APM2 projectile proposed by Lin et al. were used to validate the modelling framework [1].

The model (showed in Figure 1Figure *1*) consists of a 12 mm Alumina (Al_2O_3) ceramic strike face, a 6.3 mm UHMWPE (Dyneema®) laminate backing, and a 50 mm Roma Plastilina® No.1 clay block to evaluate Back Face Deformation (BFD), in compliance with NIJ Standard 0101.06 [2]. The assembly measures 250 mm in width and 300 mm in height. The 7.62 APM2 projectile is composed of a hardened steel core (red), a brass jacket (blue) and rear cap (yellow), and a lead filler (green).

The alumina tile mechanical behaviour is described using the Johnson-Holmquist II (JH-2) model, specifically developed for brittle materials under impact loading [3]. The model can capture the characteristic damage phenomena in ceramics, such as shock wave propagation, radial cracking, conoid formation, and comminution zone development.

The UHMWPE laminate is modelled using global orthotropic elasticity combined with the Tsai-Wu failure criterion, to capture fibre tensile fracture, matrix cracking and in-plane shear failure. Delamination is modelled with a layered strategy: the plies are meshed individually and interact through tiebreak contacts.

* Corresponding author.
E-mail address: andrea.manes@polimi.it

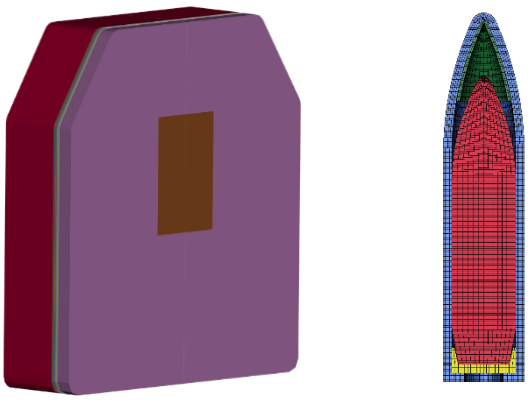

Figure 1. Finite element models of the armor system (left) and projectile (right).

The metal projectile components and the plastilina block are modelled using the Johnson-Cook constitutive law for plasticity [4]:

$$\sigma_{VM} = \left(A + B\bar{\varepsilon_p}^{n}\right)\left(1 + C\ln\frac{\dot{\bar{\varepsilon_p}}}{\dot{\bar{\varepsilon_0}}}\right)[1 - (T^*)^m] \quad (1)$$

that allows capturing the effects of strain hardening, strain-rate sensitivity and erosion. Projectile erosion and plastic flow during impact can also be accounted for when the material model is coupled with a fracture criterion and an equation of state.

The simulations are performed using the LS-Dyna explicit dynamic finite element solver.

Model Validation

To validate the numerical framework, two cases presented in Lin's publication were reproduced, to compare the damage morphology in the protection and the final back face signature. In detail, the configurations considered are: (i) ballistic impact on a soft body armour (composed of UHMWPE laminate only) and (ii) composite ceramic SAPI.

Soft Armor Validation

The UHMWPE laminate model was validated against numerical simulation results involving a 7.62×25 mm projectile.

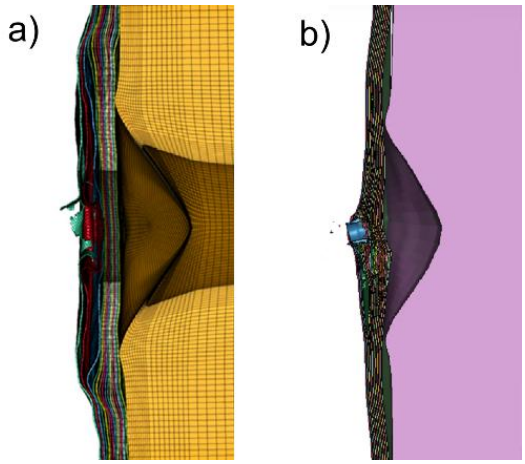

Figure 2. Comparison of the impact on the soft body armor at 300 μs: a) original work by Lin et al. [1] and b) current work.

The final value of plastilina back face deformation measured in the current model is 25.7 mm, as opposed to the 24.5 mm value reported by Lin. Figure 2 shows a comparison of the damage morphology in the protection during the ballistic impact.

Composite SAPI Validation

The full alumina/UHMWPE system was validated considering an impact of a 7.62 APM2 projectile (as visible in Figure 3).

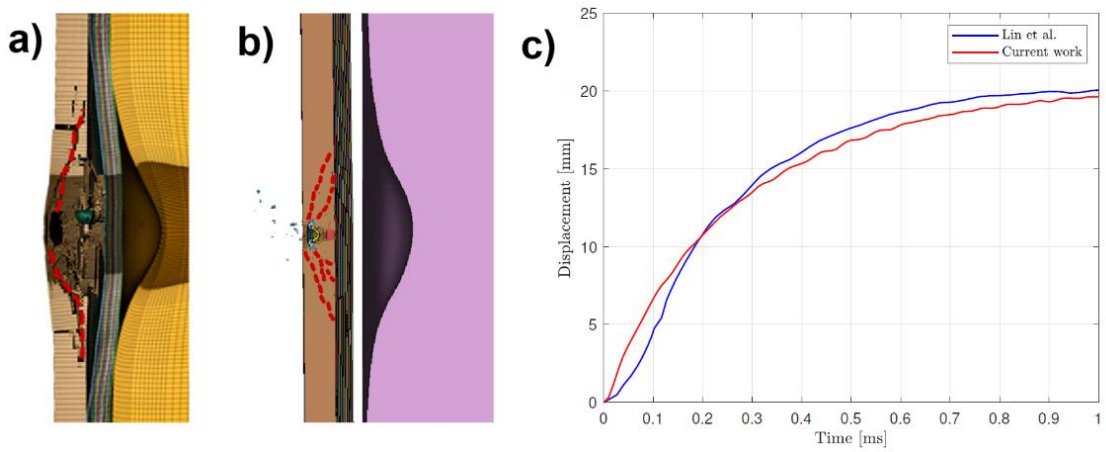

Figure 3. Comparison of the impact on the ceramic composite SAPI at 800 μs: a) original work by Lin et al. [1], b) current work and c) plastilina BFD history comparison.

Figure 3c shows the back face deformation history registered by the plastilina for the current work and the reference; the final values of BFD are 19.6 mm for the current work and 20.1 mm by Lin's model. The proposed model is able to reproduce all the typical failure phenomena, such as ceramic fragmentation and conoid formation, projectile core erosion and UHMWPE delamination, closely matching the reference. This validation confirms that the proposed numerical framework is physically reliable and suitable for damage studies.

Results

Multiple hits

The investigation of the multiple hit ballistic resistance of the protection was conducted with a parametric study of the effects of the distance between the first and second hit locations, varying the distance from 0 to 60 mm. In all cases the projectile is able to defeat the armor, but as the spacing between the two hits increases, the residual kinetic energy of the projectile reduces, dropping to 0.03% of the initial projectile kinetic energy at a distance of 60 mm. The results of the parametric study are presented in Figure 4.

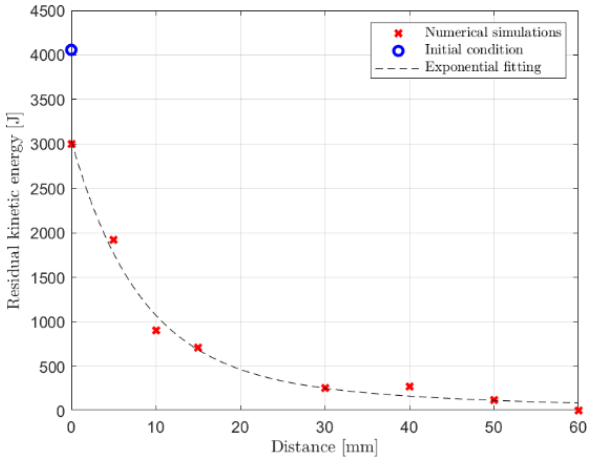

Figure 4. Residual projectile kinetic energy with regards to the distance between the two ballistic hits.

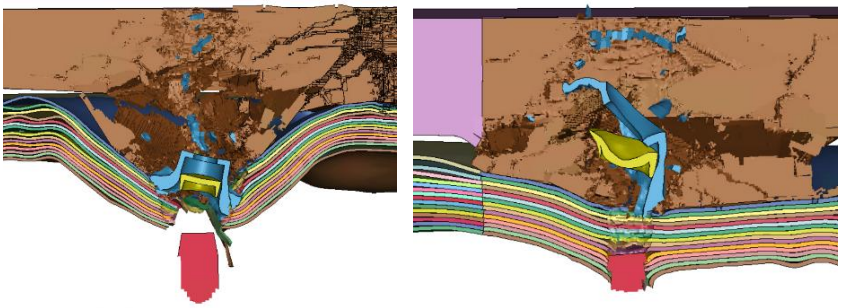

Figure 5. 30 mm (left) and 60 mm (right) spaced second impact simulation at 100 μs.

The ceramic conoid created in the first impact limits the alumina fragmentation in the second hit, and consequently the amount of energy the armor is able to absorb and dissipate. Figure 5 shows how different impact distance affects the ceramic fracture morphology and UHMWPE failure mode (extensive tearing versus localized soft plugging).

Cracked ceramic tile

The effect of a through-thickness crack and width of the alumina tile was studied simulating 6 impacts at increasing distances from the crack location, from 0 mm (projectile directly impacting the crack) to 20 mm. Since the armor is able to stop the threat for all the considered scenarios, the protective performance was evaluated measuring the back-face deformation with the plastilina backing. The results of this investigation (plotted in Figure 6) highlight how increasing the distance from the crack results in a reduction of back face signature, except for a local minimum in the near proximities of the crack, where the projectile is able to impact simultaneously both sides of the crack and consequently a larger portion of protection is able to absorb energy.

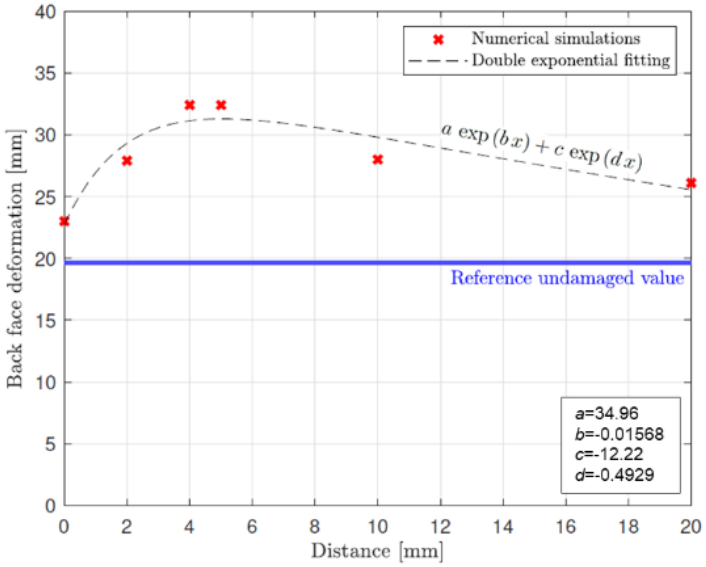

Figure 6. Back-face deformation with regards to the impact distance

The crack promotes shear sliding between the two sides of the ceramic tile and stops the shockwave propagation in the tile, preventing the formation of an extended conoid of comminuted ceramic, that dissipates the projectile's energy. As the distance between the crack and the impact location increases, the ceramic comminution is extended on a larger area, and the protective performance approaches the nominal value of an intact armor, thanks to a better distribution of internal loads.

Conclusions

The scope of this work is to build a validated numerical methodology capable of predicting ballistic resistance degradation in damaged SAPIs.

The results of this work show that pre-existent damage in the ceramic layer of a composite SAPI reduces the degree of protection against a subsequent ballistic hit, because it limits further fragmentation and development of ceramic conoid (that allows the distribution of the impact energy on a larger area of UHMWPE laminate). Increasing the distance from the damage results in increasing residual protective capability, allowing to define a safe radius outside of which the nominal protective capability is guaranteed.

References

[1] Jun Lin, Yongqiang Li, Sheng Liu, Hualin Fan. Numerical investigation of the high-velocity impact performance of body armor panels. *Thin Walled Structures 189*, 110909, 2023

[2] National Institute of Justice (U.S. Department of Justice). Backface signatures of soft body armors and the associated trauma effects – NIJ standard 0101.06, 1976

[3] G. R. Johnson et al. An improved computational constitutive model for brittle materials. A*IP Conference Proceedings*, 1994

[4] G. R. Johnson et al. A constitutive model and data for metals subjected to large strains, high strain rates and high temperatures. *Proceedings 7th International Symposium on Ballistics*, 1983

Light-Weight Armour for Defence & Security
LWAG 2026

Experimental Secondary Fragment Procedure for Testing of Light Textiles

A. Miranda-Vicario[a*], G. Algarabel[a], F. Coghe[a]

[a] *Department of Weapon Systems and Ballistics, Royal Military Academy, RenaissanceAvenue, 30, B-1000 Brussels, Belgium*

Abstract

The threat posed by Improvised Explosive Devices (IEDs) has grown significantly in recent years, with approximately 28,800 explosion events recorded between 2010 and 2020 and more than 35,000 resulting casualties. Unlike conventional munitions, IEDs often lack engineered metallic fragments and are instead packaged in improvised containers. Consequently, secondary debris (primarily soil, gravel, and environmental materials) becomes the dominant hazard. Existing standards, such as NATO AEP-2920, rely on metal fragment-simulating projectiles, which do not accurately replicate the threat posed by soil and debris in real blast scenarios [1], [2].

To address this gap, a new testing methodology was developed for lightweight protective garments (<0.5 kg/m²). The approach uses a controlled cloud of sand particles fired from a 12-gauge cartridge at approximately 550 m/s. The target assembly consists of three layers: the fabric under test, a chamois leather layer, and a foam witness sheet. Damage to the witness layer—specifically, the number of perforations—is used to rank fabric performance. Initial benchmarking confirmed that this method provides a more realistic characterization of protection against secondary debris compared to traditional fragment-based tests [3].

Several design decisions were required to obtain the final testing configuration and to understand the limitations of the methodology. Sand particles inherently exhibit dispersion due to variations in size and shape. This dispersion complicates the analysis, as greater spread influences the number and distribution of impacts when different textiles are tested. To reduce variability, more homogeneous projectiles: 1-mm and 2-mm glass spheres were evaluated. However, these alternatives produced significantly poorer results, demonstrating the importance of correctly characterizing and selecting sand before testing (Figure 1).

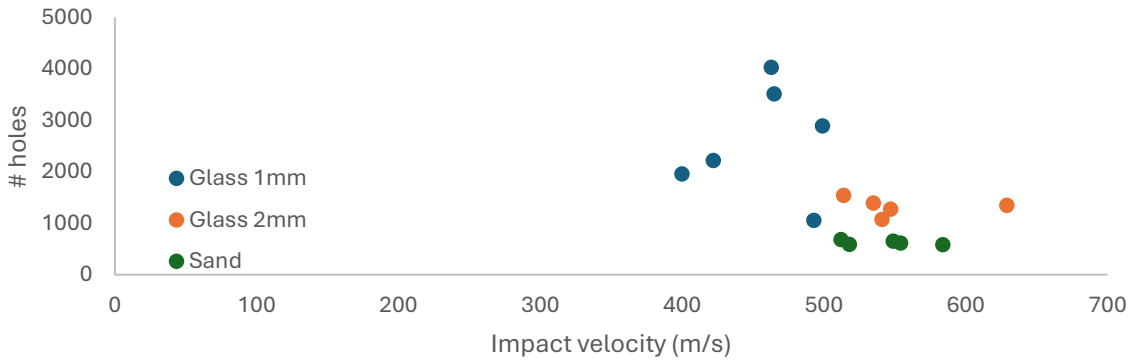

Figure 1: Number of holes vs the impact velocity.

* Corresponding author. Tel.: +32 244 1459
E-mail address: angel.mirandavicario@mil.be

To accelerate the sand cloud, no sabot was used. Although this choice increases barrel wear and produces less uniform acceleration, it was ultimately found to be the best option. A sabot would introduce additional, unintended projectiles: its components have far greater mass than individual sand grains and tend to travel faster and straighter, failing to disperse like the sand cloud (Figure 2). This would cause severe and unrealistic damage to the textile samples and make it impossible to accurately count sand impacts. A sabot stripper was also not feasible, as the sabot fragments would still pose a greater threat than the sand itself.

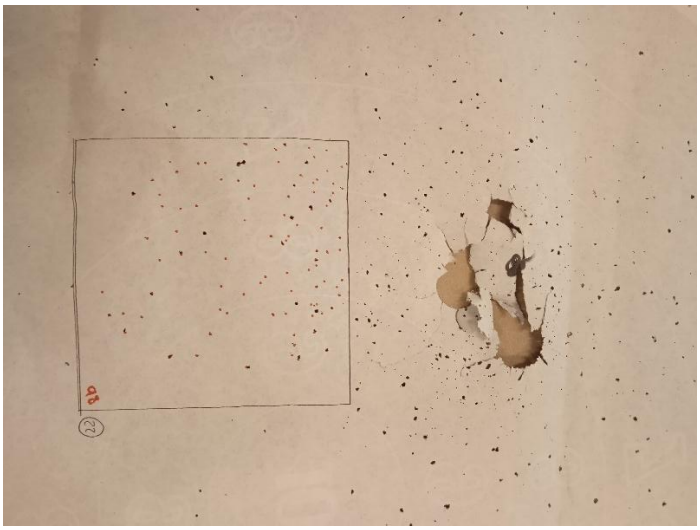

Figure 2: Target after testing.

To rank the textiles, perforations are counted on the front face of the foam witness layers, a skin layer and a foam layer [4]. This location provides a clear and interpretable damage pattern, as the first layer (the textile) has already filtered and slowed the particles. Counting perforations on the back face of the foam was not possible: the material produced irregular exit holes with remnants of foam, preventing reliable quantification. The influence of textile areal density on the number of perforations was also examined. Within the selected mass range, the effect was minor; smaller than the inherent variability of the procedure (Figure 3).

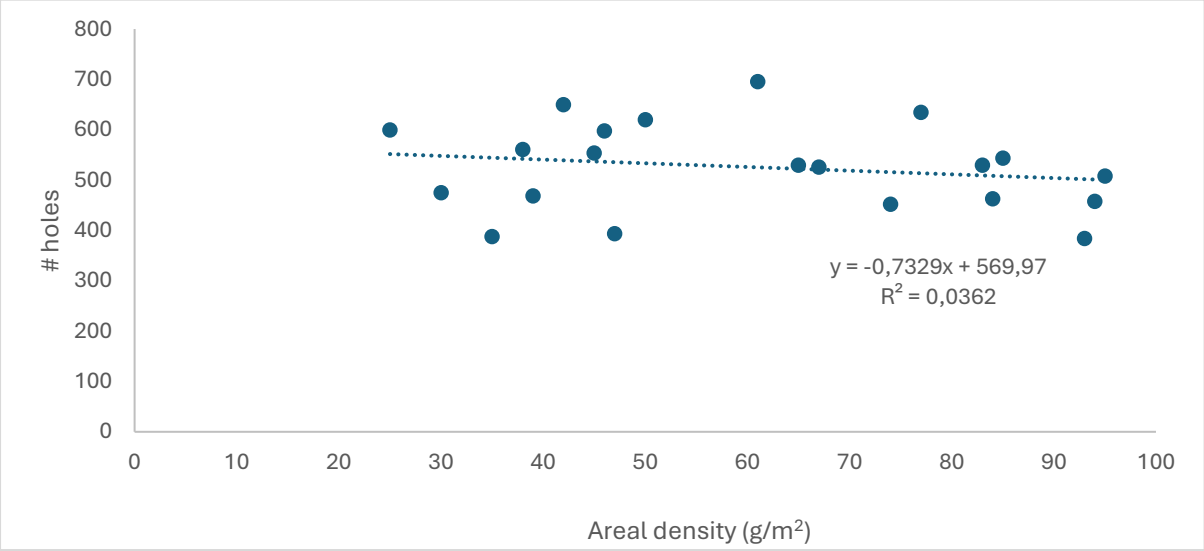

Figure 3: Number of holes vs areal density of the back face layers.

Following this first phase, additional studies were conducted to deepen understanding of fabric performance. Parameters related to fabric manufacture—such as weave density, yarn type, and finishing treatments—were investigated to determine their influence on resistance to sand-particle impacts. Furthermore, tests on swine tissue were performed to better understand penetration mechanisms and to provide a biological reference for assessing real-world injury risks. For the threat level studied, sand particles penetrated approximately 20 mm into unprotected swine tissue but did not perforate bone. When a textile layer was placed over the tissue, the number of penetrations decreased drastically, demonstrating the protective potential of lightweight garments (Figure *4*). These findings align with previous research showing that secondary debris is a major contributor to extremity injuries in blast events.

This integrated approach not only improves the evaluation of lightweight protective garments but also establishes a foundation for future design optimization aimed at mitigating secondary-debris threats.

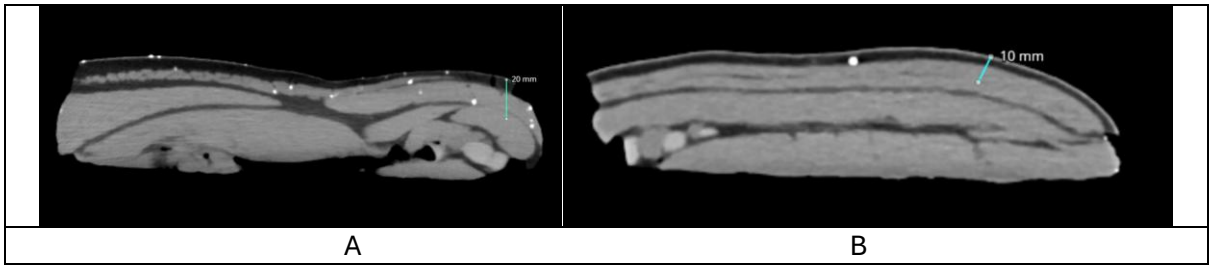

Figure 4: Swine target after the test a)unprotected and b)protected.

References

[1] P. Vivek and T. G. Sitharam, 'Sand ejecta kinematics and impulse transfer associated with the buried blast loading: A controlled laboratory investigation', *Int. J. Impact Eng.*, vol. 104, pp. 85–94, Jun. 2017, doi: 10.1016/j.ijimpeng.2017.02.017.

[2] C. Saunders and D. Carr, 'Towards developing a test method for military pelvic protection*', *J. Text. Inst.*, vol. 109, no. 10, pp. 1374–1380, Oct. 2018, doi: 10.1080/00405000.2018.1471966.

[3] A. Miranda-Vicario, G. Algarabel, R. Huzsvar, A. Moumen, and F. Coghe, 'Characterization of Lightweight Fabrics Subjected to Sand-Particle Impact', *Exp. Tech.*, Mar. 2026, doi: 10.1007/s40799-026-00873-1.

[4] NATO, 'AEP- 94: Skin penetration assessment of Non-lethal projectiles', Jul. 2021.

Light-Weight Armour for Defence & Security
LWAG 2026

Development and validation of lightweight ballistic protections based on multilayer hardfacing

Antoine Monnet[a,b]*, Teresa Fras[a], Slim Bahi[b] , Antoine Guitton[b] , Alexis Rusinek[b]

[a]*French-German Research Institute of Saint-Louis (ISL), Saint-Louis, 68300, France*
[b]*Université de Lorraine, CNRS, Arts et Métiers, LEM3, Metz, 57070, France*

The development of lightweight and efficient armor solutions has become increasingly important in response to the continuous evolution of kinetic threats, including high-velocity projectiles, fragments, and small-caliber ammunition. In this context, improving protection while maintaining acceptable mass, cost, and manufacturability remains a major challenge. Among the possible approaches, metallic composites based on the dual-hardness concept are particularly attractive, as they combine the energy absorption capacity of a ductile substrate with the high hardness and erosion capability of a hard front layer. Although hardfacing has been widely investigated for wear-resistant applications [1-4], its potential for ballistic protection, especially in the case of multilayer deposits with high concentrations of carbide-forming elements, remains insufficiently explored. This work addresses that gap by investigating the development and validation of a hardfaced steel target designed for lightweight ballistic protection.

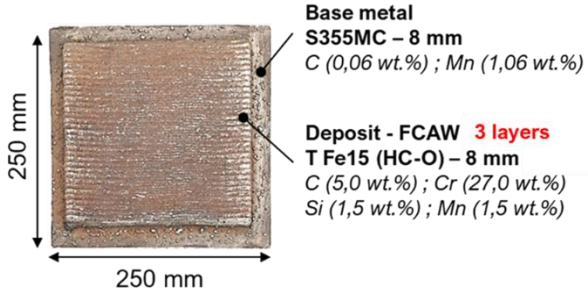

Figure 1: As manufactured metallic composite after hardfacing

In the present study, an 8 mm thick high chromium-carbon hardfacing alloy (HC-O, or T Fe15 according to EN 14700, with approximately 5 wt.% C and 27 wt.% Cr), analogous to white cast iron, was deposited by Flux-Cored Arc Welding (FCAW) onto an 8 mm thick low-carbon S355MC steel substrate. A 200x200 mm² overlay was produced on a 250 × 250 mm² substrate using three successive deposited layers, each approximately 2.6 mm thick. The resulting bi-material plate is shown in Figure 1. Several specimens were extracted from the manufactured plate in order to characterize the corresponding cross-sectional regions. Quantitative and qualitative chemical analyses were carried out together with detailed microstructural identification, crystallographic observations, and hardness measurements from the base metal to the upper deposited layer. These investigations were used to establish correlations between local chemistry, microstructure in the as-clad condition, and hardness [1]. The microstructural and hardness results are summarized in Fig. 2. A marked diffusion of chromium and carbon toward the interface during solidification and cooling generated a pronounced through-thickness chemical and microstructural gradient across the deposit. Owing to the high chromium and carbon contents in the filler wire, primary M_7C_3 carbides formed within a retained γ-Fe matrix. This microstructure led to an approximately 500%

* Corresponding author. Tel.: +33(0)389695127
E-mail address: antoine.monnet@isl.eu

increase in hardness relative to the base metal, with maximum average values close to 900 HV in the upper deposited layer (Figure 2-A). Phase-specific microhardness measurements further showed that, near the surface, the average hardness of the austenitic matrix exceeded 750 HV, while that of the primary hexagonal M_7C_3 carbides approached 1550 HV (Figure 2-B). These results confirm the strong hardening effect associated with carbide formation and the existence of a highly heterogeneous but functionally gradded hardfaced structure.

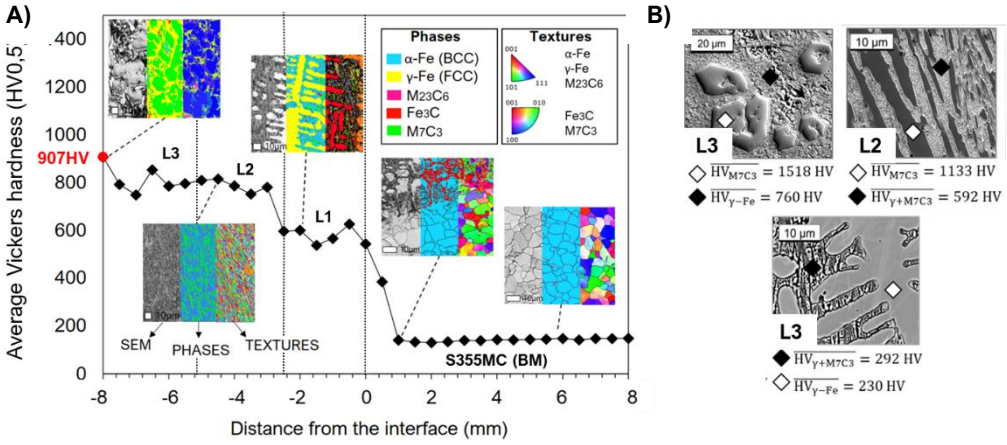

Figure 2: A- Overview of the microstructure, phase, texture and hardness investigations previously performed on the overall composite [3,8,14] ; B- Individual Vickers measurements performed on each characteristic microstructure on layers 1,2 and 3

To evaluate the ballistic efficiency of this solution, four identical targets (T-01 to T-04) were manufactured and tested on a ballistic range. For each target, a multi-hit configuration was considered, with nine shots performed over a broad range of impact velocities. Each impact was recorded using a high-speed camera in order to identify the impact location and document the failure sequence on the deposited side. The ballistic limit velocity, defined as the minimum projectile velocity required to produce complete perforation, was determined for each target. As reference materials, a monolithic 16 mm thick S355MC plate and a commercial Mars 600 armor steel plate with equivalent areal density were also tested under the same firing conditions. The target performance was then assessed through comparisons of ballistic limit velocity, depth of penetration, and projectile erosion. A part of the ballistic results are presented in Fig. 3.

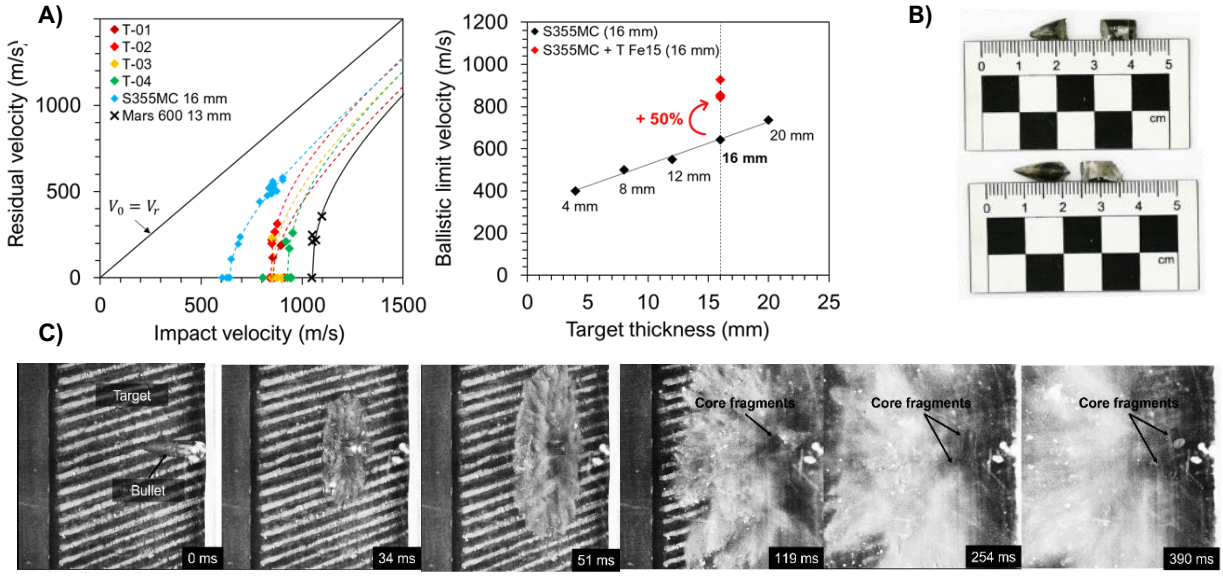

Figure 3: A- Ballistic curves obtained for S355MC 16 mm , S355MC 8 mm + T Fe15 8 mm and Mars 600 13 mm ; B- Fragmented cores from conducted experimental tests; C- Frames from high speed camera during a ballistic test for a scenario of protection (Initial velocity of the projectile : 911 m/s)

The addition of an 8 mm T Fe15 hardfacing layer onto an 8 mm S355MC substrate increased the ballistic limit velocity by nearly 50% compared with a monolithic 16 mm S355MC plate (Figure 3-A). Moreover, the ballistic limit of the hardfaced solution approached that measured for commercial Mars 600 steel at equivalent areal density. Fragmentation of the projectile core was observed in all tested configurations, including both protection and perforation cases (Figure 3-B). For most impacts, except under full perforation conditions, the mean depth of penetration remained close to the interface or within the deposited layer indicating that the hardfacing was, in most cases, sufficient to arrest the core before complete penetration of the substrate (Figure 3-C). Beyond the clear improvement in ballistic performance, the proposed architecture also appears attractive in terms of mass efficiency and cost-effectiveness, which supports its relevance for further development as a lightweight protective solution.

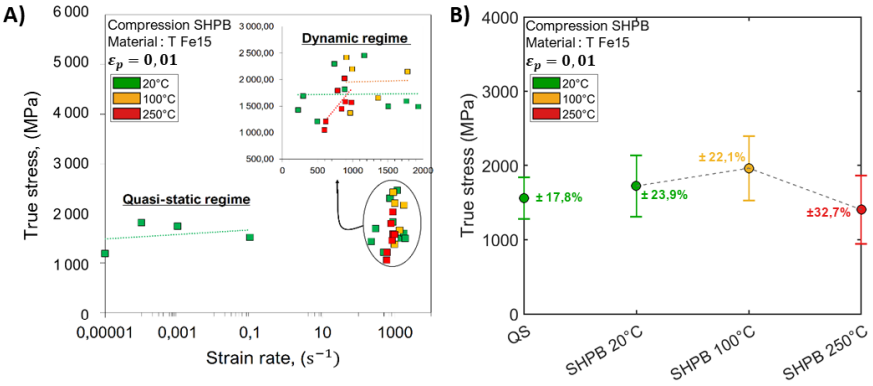

Figure 4: A) Strain-rate sensitivity of T Fe15 for tested temperatures of 20°C, 100°C and 250°C; B) Quantitative statistics of maximum true stress as a function of loading regime and temperature

In parallel with the ballistic investigation, the intrinsic mechanical behavior of the hardfacing deposit was examined under controlled loading conditions, since carbide-rich hardfacings are most often characterized in the literature in terms of hardness and wear resistance rather than intrinsic mechanical behavior under controlled loadings [5-7]. To address this gap, a combined experimental–numerical framework was developed, accounting simultaneously for microstructural gradients, loading-rate effects, and damage-driven behavior. Specimens extracted at different distances from the substrate–deposit interface were tested in compression from quasi-static to dynamic regimes using a universal testing machine and a Split Hopkinson Pressure Bar (SHPB) apparatus. Tests were conducted at 20°C, 100°C, and 250°C, and were complemented by high-speed imaging and digital image correlation. As shown in Figure 4, the studied alloy exhibited a typical high-strength together with a low-ductility response characteristic of carbide-rich quasi-brittle materials, with compressive strengths reaching approximately 2–2.5 GPa and failure governed by early damage accumulation followed by brittle fragmentation (Figure 5) [8].

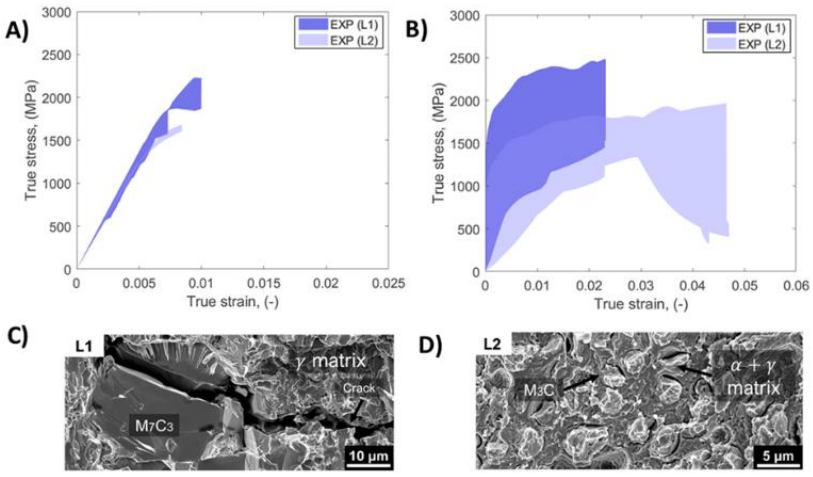

Figure 5: Experimental true stress-true strain envelopes (meaning the outer boundary enclosing the complete set of stress–strain curves) of T Fe15 for **A)** Quasi-static regime; **B)** Dynamic regime. Fracture surfaces highlighting post-test microstructure for **C)** L1-type specimens and **D)** L2-type specimens (L1 = Specimens located at the upper deposit layer; L2 = specimens located close to the interface with the S355MC substrate)

Beyond the effects of strain rate and temperature, one of the main outcomes of the study is the demonstrated influence of microstructural gradients on the mechanical response. Specimens extracted from different depths in the deposit exhibited markedly different behaviors. The carbide-rich upper layer provided higher strength, but also promoted strong strain localization and abrupt damage. In contrast, the more diluted region near the interface deformed in a more progressive manner, although at lower stress levels. The corresponding true stress–true strain envelopes and post-mortem fracture surface observations are presented in Figure 5. These results highlight that the macroscopic response of the deposit cannot be described only in terms of stiffness and peak strength, but must also account for progressive damage accumulation and post-peak strength degradation. To capture this behavior within a predictive constitutive framework, the Johnson–Holmquist JH-2 model was adopted for the hardfacing deposit. The model was calibrated through a combined experimental, analytical, and inverse-identification strategy, and was able to reproduce the main features of the response as well as the damage-driven softening observed for the two investigated microstructural states. The use of distinct parameter sets for the different sub-layers proved to be an efficient way to incorporate microstructural sensitivity into a macroscopic constitutive description. Comparisons between experimental and numerical strain fields obtained by digital image correlation showed good agreement in both strain levels and fracture patterns, as illustrated in Figure 6 [8]. This constitutive modeling of the deposit was performed as a prerequisite for the full-scale representation of the hardfaced plate and will serve as the basis for subsequent finite element simulations of the ballistic tests, with the aim of capturing the influence of through-thickness microstructural heterogeneity on the overall impact response.

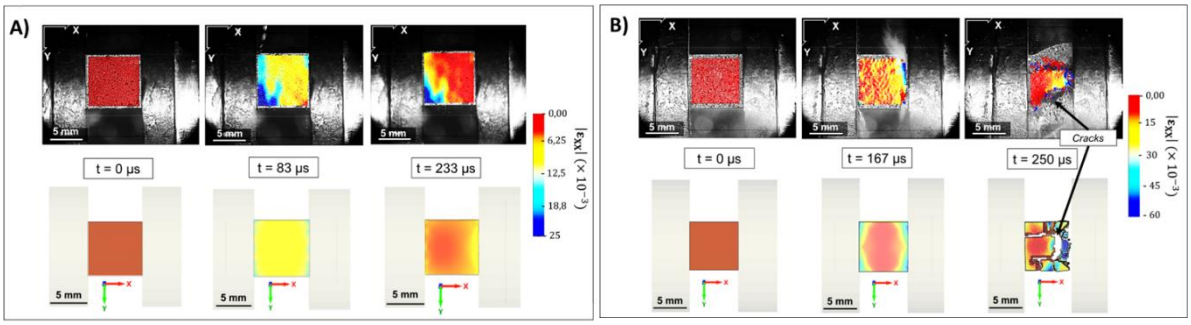

*Figure 6: Comparison between experimental and numerical strain fields (using JH-2 model) along the loading direction obtained for **A)** L1 sub-material and **B)** L2 sub-material* (L1 = Specimens located at the upper deposit layer; L2 = specimens located close to the interface with the S355MC substrate)

[1] A. Monnet, T. Fras, Á. Kazup, S. Bahi, A. Rusinek, et A. Guitton, « Multi-scale characterization of a high chromium-carbon based hardfacing alloy welded by flux-cored arc welding », *Materials Characterization*, p. 116038, janv. 2026, doi: 10.1016/j.matchar.2026.116038.

[2] A. Monnet, T. Fras, Á. Kazup, S. Bahi, A. Rusinek, et A. Guitton, « Corrigendum to “Multi-scale characterization of a high chromium-carbon based hardfacing alloy welded by flux cored arc welding” [Materials Characterization, Volume 233 (2026), 116038]. », *Materials Characterization*, vol. 233, p. 116130, mars 2026, doi: 10.1016/j.matchar.2026.116130.

[3] T. Fras, B. Koenig, P. P. Meyer, et I. Diop, « Microstructural characteristics of a highchromium cast iron hard-facing alloy », *Bulletin of the Polish Academy of Sciences Technical Sciences*, p. 151957-151957, sept. 2024, doi: 10.24425/bpasts.2024.151957.

[4] J. Winczek, M. Gucwa, M. Mičian, R. Koňár, et S. Parzych, « The Evaluation of the Wear Mechanism of High-Carbon Hardfacing Layers », *Archives of Metallurgy and Materials*, juill. 2023, doi: 10.24425/amm.2019.129502.

[5] M. R. Ardigo-Besnard, A. Tellier, A. Besnard, et J.-P. Chateau-Cornu, « Effect of the microstructure on the tribological properties of HIPed and PTA-welded Fe-based hardfacing alloy », *Surface and Coatings Technology*, vol. 425, p. 127691, nov. 2021, doi: 10.1016/j.surfcoat.2021.127691.

[6] M. Ban, N. Hasegawa, Y. Ueno, H. Shinozaki, T. Aoki, et H. Fukumoto, « Wear Resistance Property of Hardfacing Weld Overlays Containing Metal Carbides », *Tribology Online*, vol. 7, nº 4, p. 207-212, 2012, doi: 10.2474/trol.7.207.

[7] T. A. Passos, H. Costa, F. K. C. Luz, et G. Pintaude, « The Effect of the Dilution Level on Microstructure and Wear Resistance of Fe-Cr-CV Hardfacing Coatings Deposited by PTA-P », *Coatings*, vol. 12, nº 12, p. 1835, déc. 2022, doi: 10.3390/coatings12121835.

[8] A. Monnet *et al.*, « Microstructure-driven mechanical response and constitutive modeling of a Fe–Cr–C hardfacing deposit under quasi-static and dynamic loading ». 13 mars 2026. Consulté le: 5 avril 2026. [En ligne]. Disponible sur: https://hal.univ-lorraine.fr/hal-05552244

Light-Weight Armour for Defence & Security
LWAG 2026

Numerical investigation of the performance of ballistic helmets against 9mm FMJ

N. Nsiampa[a], F. Coghe[a]

[a] *Royal Military Academy, Avenue de la Renaissance 30, B-1000 Brussels – Belgium*

Extended Abstract

Combat helmets are designed to protect military personnel during impact events by defeating incoming threats (blunt, ballistic, or blast threats) without inflicting serious or fatal injury to the head. To enhance protection while maintaining comfort, combat helmet manufacturers try to maximize protection for a minimum weight by using advanced materials with a higher strength-to-weight ratio. Two types of materials meeting this characteristic have emerged in the design of modern ballistic helmets: aramid fibers represented by Kevlar developed in 1960 by Dupont and Ultra-High-Molecular-Weight Polyethylene (UHMWPE) with Dyneema as its leading commercial form. These materials exhibit different mechanical properties, which significantly influence the energy absorption during impact. Kevlar and UHMWPE composite helmets provide more effective protection and comfort against small arms projectiles and fragments compared to traditional metallic helmets. In this study, combat helmets made from Kevlar and Dyneema fibers are analyzed using a finite element head model, developed in the framework of kinetic energy non-lethal applications. The model is subjected to impact by a 9 mm FMJ (Full Metal Jacket) projectile at 435 m/s under identical frontal loading conditions. The impact force is monitored to compare the performance of both materials. The use of numerical simulations is essential to better understand and predict the effects of the helmet material on the ballistic performance and consequently, the risk of head injury to soldiers.

Introduction

Kevlar and Dyneema are both high-performance fibers used in military applications for ballistic protection, but they differ substantially in their material structure, physical properties and mechanical response. Kevlar is an aramid fiber that is typically arranged in various woven patterns, such as plain weave. Dyneema, by contrast, is made from ultra-high-molecular-weight polyethylene (UHMWPE) fibers often used in unidirectional (UD) layers. The two materials also differ in density: Dyneema is significantly lighter than Kevlar. The difference in physical and mechanical properties leads to different mechanisms of absorbing and dissipating energy under ballistic impact, which in turn can influence the behind helmet blunt trauma (BHBT).
To compare the ballistic performance of Kevlar and Dyneema materials in terms of BHBT, a 50th percentile head model is used. A 9 mm projectile impact on a helmeted head is examined, and head contact force and skull strain is used as qualitative metrics [1]. Due to the lack of experimental data, the study is comparative in nature and should be interpreted as qualitative assessment rather a validated predictive analysis.

Numerical setup

Figure 1 illustrates the setup of a helmeted head impacted by a 9×19 mm FMJ projectile; further details are provided in [1]. The same setup is used for both scenarios, with the helmet-shell material being the only variable, allowing a direct comparison of how each material will respond under identical impact conditions. The helmet-shell thickness is 7.8 mm, and the impact velocity is set to 435 m/s. A half-model is employed to reduce computational cost. The head impact force and the skull strain are used as metrics for comparison.

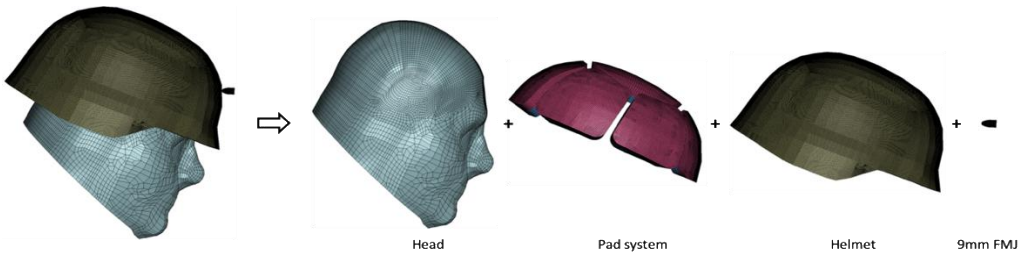

Figure 1: Setup of the impact of 9 mm against a protected head [1].

The Kevlar 129 material model developed in [2] is adopted, and its validation is performed by comparing the simulated ballistic limit with the experimental ballistic limit for 9 mm FMJ impacts against the Advanced Combat Helmet (ACH). The Enhanced Combat Helmet (ECH) is a Dyneema HB80-based helmet, but to the best of the authors' knowledge, there is no experimental data available in the open literature for the ballistic limit of 9 mm FMJ impacts on the ECH helmet. Therefore the validation of the Dyneema HB80 model is performed using flat-panel tests subjected to 1.1 g Fragment-Simulating Projectiles (FSP), as reported in [3]. The Dyneema HB80 material parameters are derived from the stiffness matrix provided in [4].

Results and discussions

The ballistic limit of the ACH under 9 mm FMJ impact obtained from the simulations is 450 m/s. According to requirements, the ACH is designed to stop a 9 mm projectile at a velocity of 358 ± 15 m/s without complete penetration of the outer shell [5–6]. Using a Dyneema-based helmet with the same geometric characteristics, a ballistic limit of 520 m/s is obtained, which meet the performance requirements for ballistic helmets. As described in [7], the helmet shell, including any hardware exposed on the outside of the shell, shall be resistant to penetration from a 9mm Full Metal Jacketed Round Nose (FMJ RN) bullet with a nominal mass of 124 grains in accordance with NIJ 0106.01 at1400 (+ 50) feet per second at 0°.

The Dyneema and Kevlar material models are implemented in the case of equal shell thickness, as described in the setup (Figure 1). Figure 2 shows the head deformation at 0.16 ms for both helmet shells. Figure 3 gives the head impact force and the skull strain as function of time.

Figure 2: Deformation of the head protected with – Left: Kevlar helmet – Right: Dyneema helmet

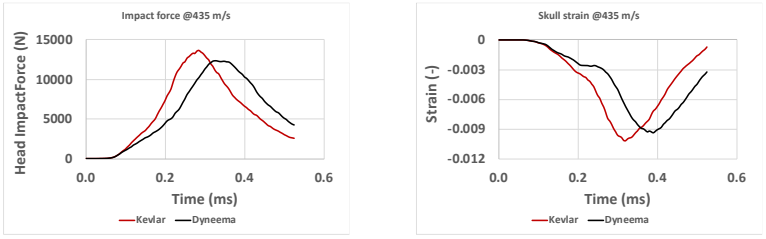

Figure 3: Comparison of head impact force (left) and skull strain (Right) as function of time

Results show that the Kevlar helmet produces higher head force and higher skull strain than the Dyneema helmet although the difference is less than 10%. This suggests that, within the BHBT framework, the likelihood of sustaining cranial injury is higher with the Kevlar helmet than with the Dyneema helmet for equal helmet shell thickness and identical impact conditions. One of the parameters that are taken into consideration is the areal density. Areal density combines both material properties and structural aspects (shell geometry) and it plays a

primary role in both resistance-to-penetration, as reflected by the ballistic limit and in BHBT, as reflected by the back face deformation, because it governs several mechanisms, including kinetic energy absorption via the amount of material available, as well as the stiffness and deformation behaviour of the helmet shell. In this study, the areal density of the Kevlar helmet shell is 0.96 g/cm², whereas that of the Dyneema helmet shell is 0.76 g/cm². This seems in contradiction with the fact that higher areal density will reduce back face acceleration. The reason might be that the Dyneema model is not capturing the correct deformation and failure mechanisms as it is validated using FSP. A 9 mm FMJ which is a deformable projectile does not induce the same deformation mechanisms in the Dyneema laminates as an FSP. Therefore, validation based solely on FSP impacts is not fully representative of the actual threat.

The Dyneema-based composites generally offer superior resistance-to-penetration compared with Kevlar-based systems [8–9] and the Dyneema helmet shell has a lower flexural stiffness than the Kevlar helmet shell, which leads to a higher back face deformation, the main cause of the BHBT. This can be seen in the force-time curves (Figure 3) as the Dyneema helmet curve is smoother than the Kevlar helmet curve.

The acceptable impact-force tolerance for cranial fracture is approximately 5 kN and for the skull strain 0.4% (moderate skull fracture) [10–12]. When compared to the maximum values of the model results, the model predicts higher risk of skull fracture. As shown in [1], the numerical results consistently show higher values for the considered injury metrics, suggesting a potentially higher cranial injury risk. Unfortunately, no experimental data are available to assess in which extent the model can predict what is seen in real situations Therefore, the analysis remains qualitative.

Conclusions

A qualitative study was conducted by comparing the response of a helmeted head subjected to 9 mm FMJ impact using Dyneema-based and Kevlar-based helmet shells of equal thickness. The results indicate that, at equal thickness, the Kevlar-based helmet is associated with a lower likelihood of cranial injury than the Kevlar helmet but the difference is not big. The two materials exhibit different structural behaviours: Kevlar, typically configured as woven aramid layers, and Dyneema, arranged as unidirectional UHMWPE laminates, differ in stiffness, areal density, and energy-absorption mechanisms. These differences lead to measurable variations in how each helmet attenuates the impact and mitigates the forces to the head.

References

[1] Nsiampa N, Coghe F. Preliminary study of Behind Helmet Blunt Trauma Assessment using a Numerical Head Model. Proceedings - 17th Personal Armour Systems Symposium 2025.

[2] Nsiampa N, Coghe F. Modeling of Schuberth helmet under ballistic impact for head injury assessment. Proceedings - 34th International Symposium on Ballistics 2025; 2:1479-1487.

[3] van der Werff, H., & Heisserer, U. (2016). High-performance ballistic fibers: Ultra-high molecular weight polyethylene (UHMWPE). In Advanced fibrous composite materials for ballistic protection (pp. 71-107). Woodhead Publishing..

[4] Utomo B, Meer B, Ernst LJ, Rixen D. High-speed Impact Modelling and Testing of Dyneema Composite, PhD Dissertation (2011).

[5] Palta E, Fang H, Weggel DC. Finite element analysis of the Advanced Combat Helmet under various ballistic impacts. International Journal of Impact Engineering, 2018; 112:125-143.

[6] NIJ (1981), Ballistic standard for ballistic helmets. U.S. Department of Justice National Institute of Justice, Standard -0106.01.

[7] Purchase Description Helmet for Enhanced Combat Helmet (Draft), version 0.1, PD-ECH-ICE-PG16-0001; 2009.

[8] Mortlock RF. Protecting American Soldiers: The Development, Testing, and Fielding of the Enhanced Combat Helmet (ECH). https://www.pmi.org/-/media/pmi/documents/public/pdf/learning/pmj/early-edition/feb-mar-2018/j20180296.pdf

[9] Hester J, Johnson T, Freeman F. Managing Risks: Statistically Principled Approaches to Combat Helmet Testing. https://apps.dtic.mil/sti/trecms/pdf/AD1124049.pdf

[10] Motherway JA, Verschueren P, Van der Perre G, Vander Sloten J, Gilchrist MD. The mechanical properties of cranial bone: The effect of loading rate and cranial sampling position. J. Biomech. 2009; 42:2129-2135.

[11] Raymond D., Van Ee C, Crawford G, Bir C. Tolerance of the skull to blunt ballistic temporo-parietal impact. J. Biomech., 2009; 42: 2479-2485.

[12] Freitas CJ, Mathis JT, Scott N, Bigger RP, MacKiewicz J. Dynamic Response Due to Behind Helmet Blunt Trauma Measured with a Human Head Surrogate. Int J Med Sci 2014; 11(5):409-425. doi:10.7150/ijms.8079. https://www.medsci.org/v11p0409.htm

Light-Weight Armour for Defence & Security
LWAG 2026

Reducing Behind-Armour Blunt Trauma with TPMS Structures

Sebastian Reimold[a], Sergej Grednev[a], Anne Jung[a*]

[a]*Helmut-Schmidt-University / University of the Federal Armed Forces Hamburg, Holstenhofweg 85, Hamburg, 22043, Germany*

Extended Abstract

Behind-Armour Blunt Trauma (BABT) remains a critical challenge in the development of modern personal protective equipment. Even when a projectile is successfully stopped by a ballistic vest, the transferred kinetic energy can cause severe blunt trauma injuries such as rib fractures, lung contusions, or internal bleeding. The reduction of these deformation-induced injuries is therefore an essential aspect in the optimization of future lightweight protection systems. [1]

Triply Periodic Minimal Surface (TPMS) structures have attracted increasing interest for energy-absorbing applications due to their high specific energy absorption, low density, and tunable mechanical behaviour. [2] Their continuous cellular architecture enables an efficient distribution of stresses and deformation energy, making them promising candidates for ballistic and impact mitigation systems. Within this work, different TPMS configurations were investigated regarding their suitability for reducing BABT in soft and hard ballistic protection systems.

The presented work builds upon preliminary manufacturing investigations of miniaturized TPMS structures produced by additive manufacturing. In a preceding study, four TPMS geometries – Diamond, Gyroid, I-WP, and Primitive – were manufactured in multiple parameter configurations with varying cell size and relative density using high-resolution DLP stereolithography. The successful fabrication of these structures demonstrated the feasibility of producing highly detailed miniature lattice systems for protective applications (see Figure 1).

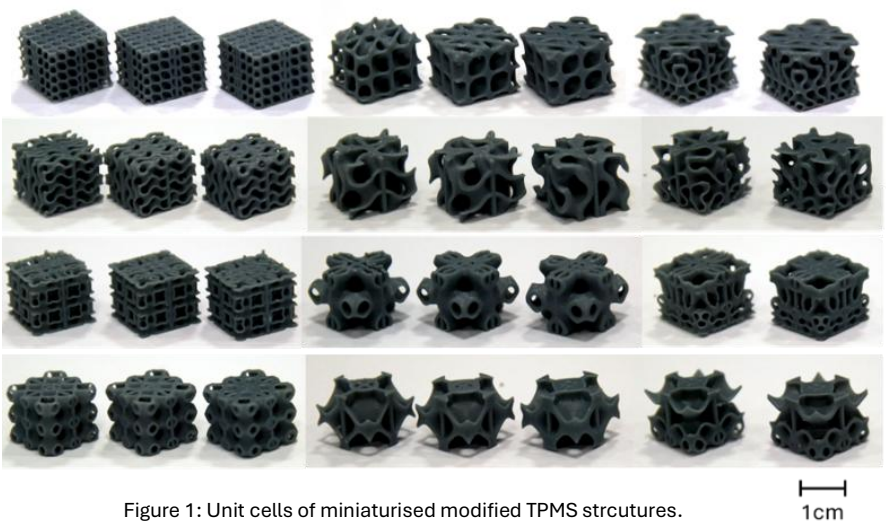

Figure 1: Unit cells of miniaturised modified TPMS strcutures.

Based on these findings, selected TPMS configurations were subjected to quasi-static compression tests to identify structures with favourable deformation and energy absorption characteristics (see Figure 2). The quasi-static investigations revealed significant differences between the investigated topologies. Structures with isotropic sheet-based architectures, especially Gyroid and I-WP configurations, showed stable deformation behaviour and improved energy absorption compared to more localized collapsing structures. Additional reinforcement concepts using integrated cross-structures were also investigated to improve manufacturability and structural stability.

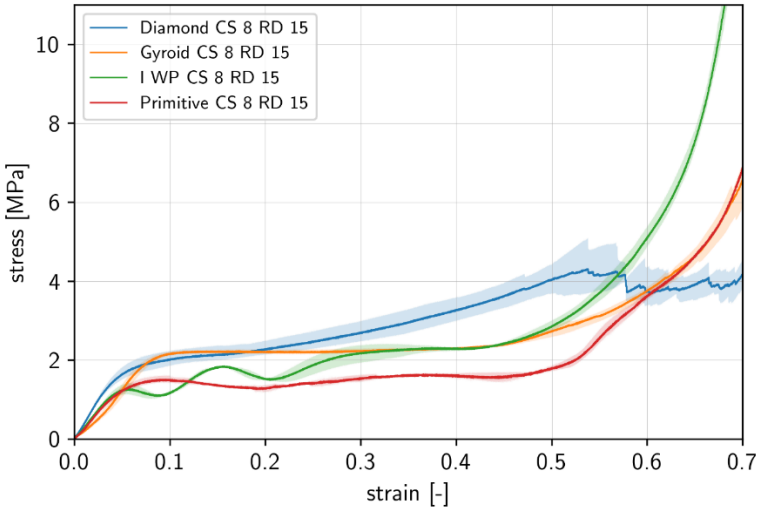

Figure 2: Comparison of the quasi-static stress strain diagrams of different TPMS structures. CS: cell size; RD: relative density

The most promising TPMS structures were subsequently integrated into ballistic protection assemblies and evaluated in ballistic experiments following VPAM-based testing procedures. Both soft ballistic (VPAM 3) and hard ballistic (VPAM 6) protection systems were investigated. The ballistic tests focused on the resulting deformation depth in the backing material as a measure for the severity of BABT. High-speed imaging and computed tomography were additionally used to analyse the deformation and failure mechanisms of the protective systems and the integrated TPMS structures.

The experimental investigations demonstrated that TPMS structures can significantly influence the deformation behaviour of ballistic protection systems. In soft ballistic configurations, several TPMS specimens were destroyed during impact and fragmented parts penetrated into the backing material, indicating insufficient structural integrity for this application scenario. In contrast, the hard ballistic configurations showed promising results (see Figure 3). The integration of selected TPMS structures reduced the penetration depth into the backing material by up to 39% compared to reference configurations without TPMS inserts. The results indicate that TPMS structures can contribute to a more efficient redistribution and absorption of impact energy during ballistic loading.

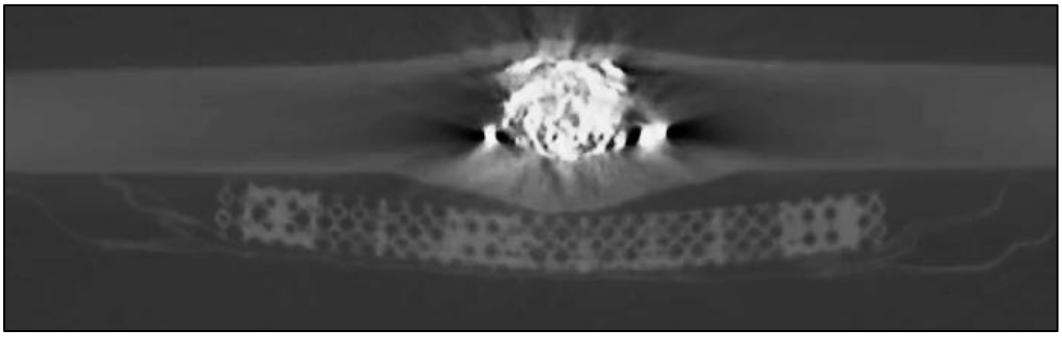

Figure 3: CT scan of a hard ballistic plate with attached TPMS plate (bottom) to reduce BABT after hit.

The study highlights the considerable potential of additively manufactured TPMS structures for future lightweight armour systems. Especially in combination with hard ballistic protection systems, TPMS-based energy absorbers may contribute to reducing blunt trauma while maintaining low areal density and structural adaptability. Future investigations should therefore focus on optimized material systems, graded TPMS architectures, dynamic characterization under high strain rates, and numerical simulation approaches for the targeted design of BABT mitigation structures.

References

[1] Bass, C.R. et al., *Injury Risk in Behind Armor Blunt Thoracic Trauma*, Journal of Trauma, 2008.

[2] Feng G. et al., *Mechanical properties and deformation behavior of functionally graded TPMS structures under static and dynamic loading*, International Journal of Impact Engineering, 2023.

Light-Weight Armour for Defence & Security
LWAG 2026

Effect of consolidation pressure on the protection capability of Dyneema

Sanna Andersson, Patrik Appelgren, Patrik Lundberg*

Swedish Defence Research Agency, FOI, Olof Arrhenius väg 3, SE-137 94 Norra Sorunda, Sweden

---

Extended Abstract

Introduction

To investigate whether increased consolidation pressure during the manufacture of fibre-composite plates made of UHMWPE (Ultra High Molecular Weight Polyethylene) will improve their ballistic performances, plates pressed at normal and at elevated pressure were produced. The UHMWPE used was Dyneema HB210 from Avient. Each plate consisted of 74 layers of HB210 and had final dimensions of 167×167×10 mm. Because UHMWPE surfaces are difficult to bond directly, the outermost layer of each plate was covered with a glass-fibre fabric to facilitate adhesive bonding.

The Dyneema plates pressed at normal pressure were manufactured by a composite company using standard methods, while the other plates were consolidated by the isostatic pressing specialist Quintus. Due to industrial confidentiality, the precise processing parameters are not publicly available. However, the plates pressed at normal pressure were manufactured by heating the stacked HB210 layers to approximately 100 °C while applying ~20 bar of uniaxial pressure for roughly 10 minutes and then subsequently increase the temperature to about 125 °C and the pressure to 150–200 bar for an additional ~30 min. The high-pressure consolidation was performed at the Quintus Application Centre in Västerås using a Quintus Flexform press (model QFC0.7×1.8-1400). The manufacturing cycle included preheating and degassing of the stacked HB210 foils and then consolidation at 1400 bar pressure for 2.75 hrs at a nominal temperature of 130 °C.

Two types of targets were manufactured, one ceramic/Dyneema composite target and one made of a 10 mm Dyneema plate only. The ceramic target consisted of a 7.1 mm silicon carbide tile (Hexaloy SA, Saint-Gobain), bonded onto the 10 mm Dyneema plate using epoxy adhesive (Collano RS 6400). The ceramic tiles and the Dyneema plates had outer dimensions of 101×101 mm and 167×167 mm, respectively, resulting in an areal density of 33 kg/m² for the assembled target (calculated over the area of the ceramic).

Ballistic testing and material characterisation

The influence of consolidation pressure on the ballistic performance of the ceramic/Dyneema target was evaluated through a series of ballistic tests using an AP surrogate projectile developed by FOI. To enable comparison with published literature data, additional tests were conducted on Dyneema plates alone, impacted by standardised fragment-simulating projectiles (1.1 g FSP). Both the plates pressed at normal pressure and at 1400 bar were tested. In parallel with the ballistic experiments, FOI examined how the fibre architecture and the thickness of individual fibre layers were affected by the consolidation pressure, with the aim of identifying microstructural mechanisms responsible for possible differences in ballistic performance.

For the test of the ceramic/Dyneema targets, an in-house AP-projectile made of cemented carbide was used. The projectile was 25 mm long and had a diameter of 5,6 mm and was fitted with a 55° conical tip, see Figure 1. The projectile was launched using a plastic sabot (Duratron) fired through a smoothbore 7.62 mm barrel. To eliminate projectile yaw, the muzzle was placed 15 mm from the ceramic target, i.e., the projectile impacts the target while still guided by the bore. The projectile velocity was measured by filming the movement through a horizontal slit in the barrel close to the muzzle using a high-speed camera model FASTCAM Nova S16, see Figure 2.

* Corresponding author. Tel.: +46 709 277 154
E-mail address: Patrik.lundberg@foi.se

For the tests of the Dyneema plates alone, fragment simulating projectiles (FSP) of mass 1.1 g were used. The FSP with skirt was launched from a 5.56×45 mm barrel with 1:7” twist. The distance between muzzle and target was 2 m and the velocity was measured using an optic screen, HPI B472, placed with its centre 0.5 m from the target. The target was aligned using laser and a mirror to ensure 0° obliquity. The FSP was filmed using a high-speed camera model FASTCAM Nova S16 to monitor the yaw at impact.

(a) (b) (c)

Figure 1. FOI:s test projectile (a) and when mounted in a plastic sabot of Duratron (b). The projectile length was 25 mm, the diameter 5.6 mm and the pointed 55° tip. The fragment simulating projectile FSP of mass 1.1 g (c).

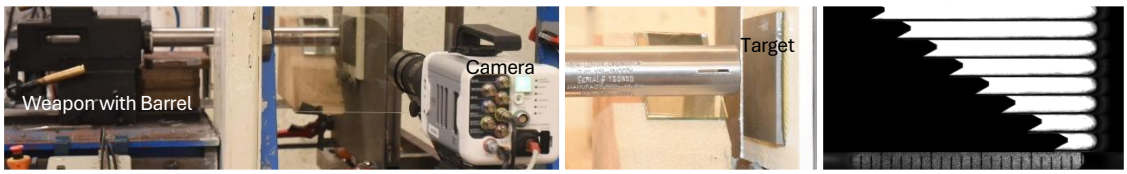

(a) (b) (c)

Figure 2: Test setup with the weapon with barrel and high-speed camera for the velocity measurement (a). The barrel with a slit (b) and examples of a pictures from the film for velocity measurement (c).

Measurement of the ballistic limit

The ballistic limit velocities corresponding to 50% and 5% probability of perforation (v50 and v5) were determined according to the Army criterion. Under this definition, a perforation is recorded if the target exhibits any through-passage that allows visible light to pass. A test is also classified as a perforation if the projectile has become lodged within the target but remains visible from the rear face. In the present experiments, the penetration channels were usually well defined, although often closed due to partial melting or charring of the composite material. Therefore, each plate was inspected visually to determine the outcome. The ballistic tests were conducted in accordance with the procedures in AEP-2920 [1], with adjustments to impact velocity to ensure a mixed zone of partial penetrations (PP) and complete penetrations (CP) within an appropriate velocity range. AEP-2920 prescribes a statistical evaluation method based on maximum likelihood estimation (MLE). Using this approach, the mean value μ and standard deviation σ of the assumed normal distribution describing the transition from low to high perforation probability are estimated. The mean value μ corresponds to the ballistic limit velocity. The method also yields confidence intervals for the estimated limit. To achieve a sufficiently narrow confidence interval, as well as enough mixed PP/CP outcomes to reliably determine the standard deviation, practical experience shows that a minimum of 20 shots is typically required.

Material characterisation

To assess the influence of consolidation pressure, the microstructure of the Dyneema plates were examined. However, preparing the Dyneema for microstructural examination proved to be challenging, as the material is difficult to section and polish in a manner suitable for analysis using optical microscopy or scanning electron microscopy (SEM). An initial attempt was made to generate a brittle fracture surface by cooling specimens in liquid nitrogen and mechanically breaking them. Despite the fact that the glass-transition temperatures of UHMWPE and the binder used (thermoplastic polyurethane) are around –150 °C and –50 °C, respectively, and that liquid nitrogen reaches –196 °C, a brittle fracture surface could not be achieved. As a result, the specimens were instead cut and mechanically polished, and a subset were additionally “etched” using ethanol to enhance contrast. Figure 3 presents two representative microstructural images obtained using this method. A layered structure can be distinguished, although the individual UHMWPE fibres themselves cannot be resolved.

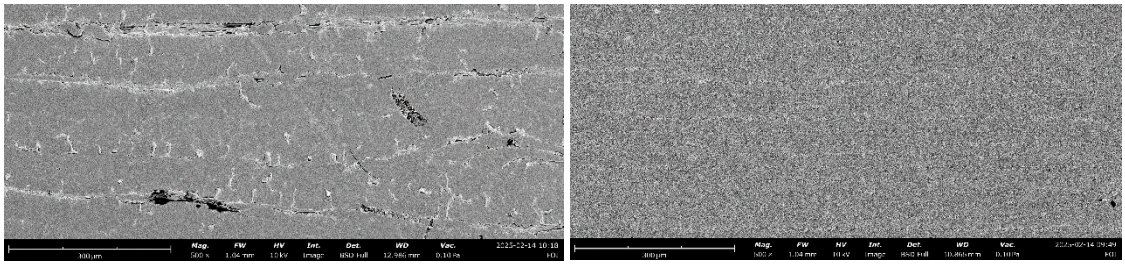

(a) (b)

Figure 3. Representative cross-sections of Dyneema HB210 consolidated at normal pressure (a) and at 1400 bar (b).

Results for AP against ceramic/Dyneema targets

In total, 16 shots were fired against the ceramic target with Dyneema pressed at normal pressure and 19 shots against the ceramic target with the Dyneema pressed at 1400 bar. The v50 and v5 was evaluated for both materials, see Table 1 and Figure 4.

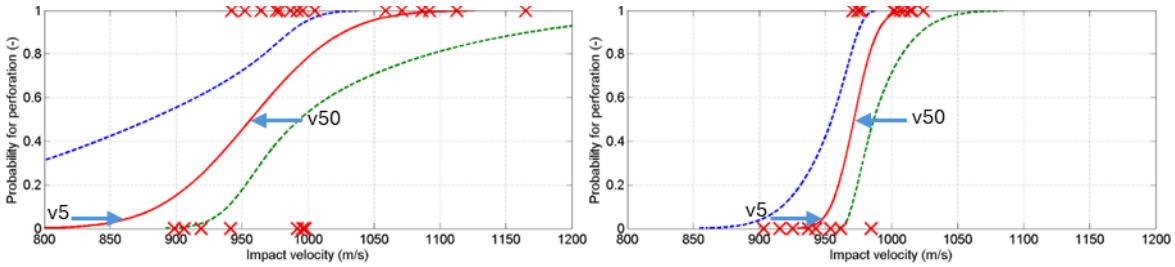

Figure 4. Probability for perforation for FOI test-projectile as function of impact velocity for ceramic/Dyneema manufactured at normal pressure (a) and at 1400 bar (b).

Table 1. Evaluated v50 and v5 from ballistic tests with FOI test projectile.

Projectile	Ceramic/Dyneema target	v50	v5
FOI test projectile (length 25 mm, diameter 5,6 mm)	HB210 (normal pressure)	956 m/s	866 m/s
FOI test projectile (length 25 mm, diameter 5,6 mm)	HB210 (1400 bar)	972 m/s	949 m/s

Results for 1.1 g FSP against Dyneema targets

In total 23 shots were fired against the Dyneema plate targets pressed at normal pressure and 19 shots against the one pressed at 1400 bar. The v50 and v5 was evaluated for both materials, see Table 2 and Figure 5.

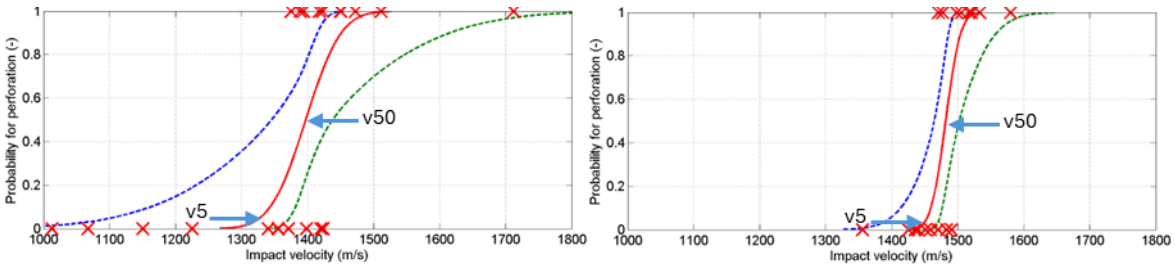

Figure 5. Probability for perforation for FSP versus impact velocity for normal pressed (a), and for pressed at 1400 bar (b).

Table 2. Evaluated v50 and v5 from ballistic tests with 1.1 g FSP.

Projectile	Dyneema target	v50	v5
Fragment (FSP) 1,1 g	HB210 (normal pressure)	1397 m/s	1328 m/s
Fragment (FSP) 1,1 g	HB210 (1400 bar)	1482 m/s	1453 m/s

Layer thickness as a function of consolidation pressure

Figure 6(a) shows a single sheet of Dyneema HB210, revealing that each sheet consists of four orthogonally oriented layers of so called unidirectional (UD) tape. The average thickness of the HB210 sheet is 0.190 mm, implying that each individual UD layer is approximately 50 µm thick. A magnified image of a fibre bundle, highlighted in red in Figure 6(a) is shown in (b). This image suggests that the diameter of the individual UHMWPE fibres is less than 1 µm. Figure 6(c) summarises the evaluated layer thicknesses in Figure 3, as function of consolidation pressure. Because the individual fibres could not be resolved in the micrographs shown in Figure 3, it is not possible to conclusively determine which specific structural features the measured thickness values represent. Nevertheless, the data indicate that the layer thicknesses do not change appreciably with increasing consolidation pressure.

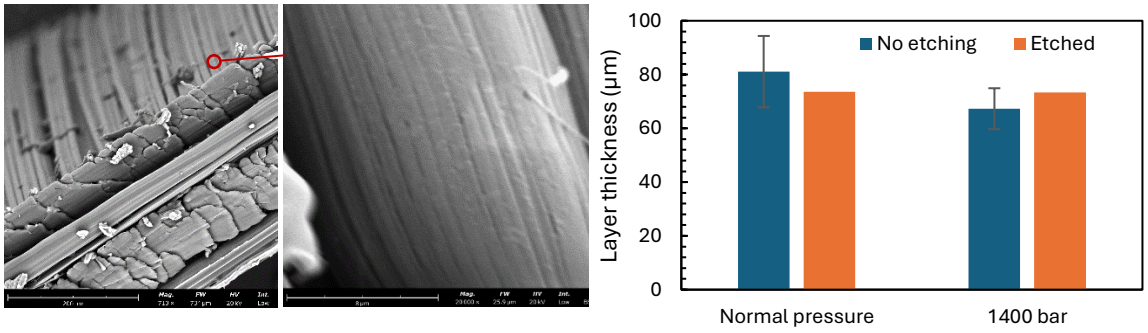

(a) (b) (c)

Figure 6. HB210-foil with four orthogonal UD-layers (a). Close view of a fibre bundle where individual UHMWPE fibres are visible (b) estimated layer thickness as function of pressure (c).

Discussion

Both the tests with the FOI test projectiles fired against the ceramic/Dyneema targets and the fragment-impact tests on the Dyneema plates demonstrate that ballistic performance improves with increasing consolidation pressure, as show previous by others, e.g., [2,3]. At a 50% probability of perforation, i.e., v50, the ballistic limit increased by approximately 2% for the ceramic/Dyneema configuration and 6% for the Dyneema targets when the consolidation pressure was raised from 150–200 bar to 1400 bar. At the more stringent 5% perforation probability, i.e., v5, the corresponding improvements were 10% and 9%, respectively. In addition to increasing the ballistic limit, the transition from low to high perforation probability became noticeably sharper, and the associated confidence intervals narrowed. The observation that v50 increases by only 2%, while v5 increases by 10% for the ceramic/Dyneema targets, together with the sharper probability transition, suggests that pressing at 1400 bar primarily makes the material more homogeneous. If the plates had also become substantially stronger or stiffer, for example through an increased fibre-to-matrix ratio, one would expect a more pronounced increase in v50 as well.

Thus, some effect on the overall strength of the Dyneema plates of the consolidation pressure may be seen in the fragment tests, where v50 increased by 6%. Although the dataset is limited, the soft steel fragments perforating the 1400 bar plates were, on average, 4% shorter than those perforating the normal pressed plates. This indicates a higher resisting force in the Dyneema plates pressed at 1400 bar compared to the one pressed at normal pressure. A possible explanation proposed in [3], is that this is due to the reduced void content and improved interlayer bonding in the Dyneema pressed at 1400 bar.

Conclusions

The results of this study indicate that the ballistic performance at low probabilities of perforation (v5) for ceramic body armour plates can be improved by approximately 10% when the Dyneema backing is consolidated at pressures higher than those typically used in current industrial practice. At the same time, the protective performance becomes more predictable, as evidenced by the sharper transition from low to high perforation probability. These improvements arise from the increased material homogeneity achieved at elevated consolidation pressures, i.e., reduced void content and improved interlayer bonding. While manufacturing techniques are primarily the responsibility of armour producers, it remains in the interest of end users to influence technological development toward more weight-efficient protection systems. By specifying stricter requirements for the quality and consistency of key material components, users can achieve measurable benefits. A 10% improvement in v5 corresponds, for a given threat, to an increase in protection equivalent to reducing the required stand-off distance by up to 100 meters. To achieve improvements beyond those demonstrated here, further optimisation of the UHMWPE-tape is likely required, specifically, increasing the fibre volume fraction relative to the thermoplastic matrix.

References

[1] NATO - AEP-2920, Procedures for the evaluation and classification of personal armour bullet and fragmentation threats. 16 September 2016.
[2] T. R. Lässig, et. al., Effect of consolidation pressure on the impact behaviour of UHMWPE composites. Composites Part B: Engineering 147, pp. 47-55, 2018.
[3] M. van der Kamp et. al., Development and performance of an UHMWPE rifle helmet shell. Avient Protective Materials. 16th Personal Armour Systems Symposium (PASS 2023), Dresden, Germany, September 2023.

File naming

Extended abstract: Sanna Andersson et al_LWAG2026_extended abstract.doc

Light-Weight Armour for Defence & Security
LWAG 2026

Use of high-performance fibre materials and optimized production techniques for more tailor-made lightweight personal protective equipment

Tom Thorvaldsen[a]*, Anders Wien[b], Kristin Karlsen[c]

[a]*Norwegian Defence Research Establishment (FFI), Insittuttveien 20, 2007 Kjeller, Norway*
[b]*NFM Technology AS, Glynitveien 15, N-1400 Ski, Norway*
[c] *Norwegian Defence Material Agency (FMA), Rødskiferveien 20, N-1352 Oslo, Norway*

Extended abstract

Modern warfare is continuously developing, and ballistic protection systems and concepts must be adapted and adjusted accordingly to meet these requirements. For personal protective equipment (PPE) for ballistic protection of military personnel, a main goal is to develop more light-weight components and modular systems, also considering protection against emerging threats. As part of this development, new light-weight materials, such as ultra-high molecular weight polyethylene (UHMWPE) fibres, are applied. Combining such high-performance modern materials with new and optimized production techniques is believed to result in products with lower weight and similar (or hopefully improved) ballistic performance compared with current products on the market. Moreover, more optimized production methods are also believed to reduce the material waste, as well as the overall production footprint.

In this presentation, we show some of the main results from a recently ended (in August 2025) five-years national research and development program. The overall objective of the program has been to develop next generation personal ballistic protection equipment that meets tomorrow's requirements and threats. To meet this goal, research within different areas has been conducted, as illustrated in Figure 1. The main focus has been on exploring new ways of employing state-of-the-art high-performance fibre materials, in combination with filament winding and high-pressure consolidation.

The goal of the materials research has been to establish a high-performance material system that can be used for filament-winding of ballistic components and products. The new material system should have the same or better ballistic performance, compared with existing systems. Moreover, it has been important to reduce the weight of the final product, to reduce the amount of waste material during production, as well as look into the long-term properties and aging of such materials.

Different material systems have been considered, in particular, ultra-high molecular weight polyethene (UHMWPE) fibres in combination with resin systems. With the use of high temperature and pressure during consolidation, the work has aimed at reducing the matrix content in the composite to a minimum and to obtain a hexagonal packing of the high-performance fibres. A significant amount of work has been done on a commercial UHMWPE fibre impregnated with high-density polyethylene (HDPE) particles of resin. The resin particle impregnated UHMWPE fibres have been provided by the company Fibroline [1]. During consolidation, the HDPE particles are melting and provide the bonding between the fibres. Also, other material systems have been characterized and tested out.

* Corresponding author. Tel.: +47 481 28 323
E-mail address: tom.thorvaldsen@ffi.no

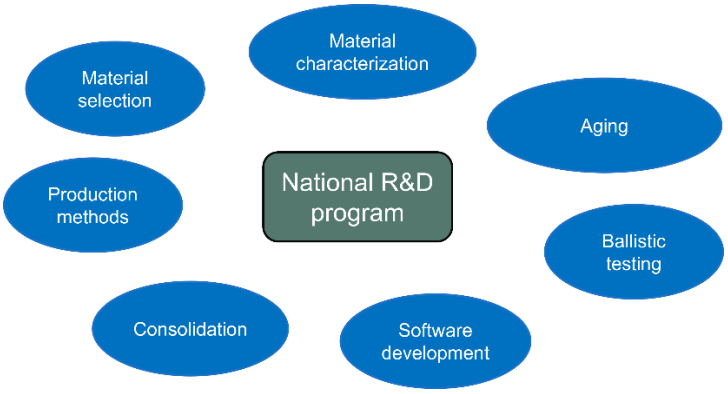

Figure 1: Research areas of the national research and development program.

The different high-performance fibres have been filament-wound on a flat plate mandrel, see Figure *2* for an example of the material system provided by Fibroline. Thereafter, the material system (including the mandrel) is cured and consolidated using NFM's production process for high-end personal protective equipment, called FREC2. The FREC2 technology includes consolidation under high isostatic pressure, combined with elevated temperature for optimal curing of the resin system. The pressure levels are much higher than what is used in conventional pressing of ballistic panels, and this is found to give better ballistic performance compared with similar products where lower pressure levels are applied. In the program, work has been done on optimizing the process parameters of the FREC2 process during consolidation of the protective prototype structures for the new materials developed. The temperature and pressure level during the different steps of the curing cycle will influence the properties of the final structure, and in particular, the ballistic properties. Moreover, more optimized temperature and pressure loading during consolidation will avoid damaging the fibres (in particular), as the fibre properties will degrade if too high temperatures are applied.

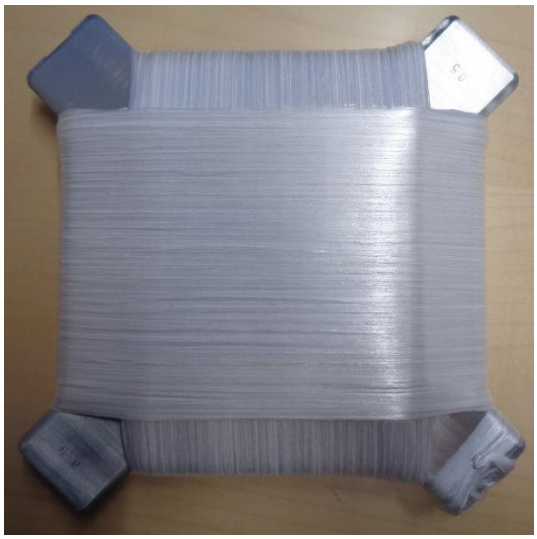

Figure 2: Filament-wound panel of the UHMWPE fibre with HDPE particles provided by Fibroline, prior to consolidation.

For characterization of the produced filament-wound flat panels, as well as the fibres themselves, a test campaign has been conducted [2, 3, 4, 5, 6]. The test plan includes a short-beam strength test, flexural testing, tensile testing, differential scanning calorimetry, Fourier-transform infrared spectroscopy and thermogravimetric analysis, as well as optical microscopy and scanning electron microscopy. Some ballistic testing has also been performed. The tests have been conducted for a set of reference systems (used in today's products at NFM) and the new material systems developed in the program, to be able to compare the material properties and their performance. As an overall conclusion from this test/characterization campaign, the production parameters, i.e. the temperature and pressure profiles during consolidation, have impact on the mechanical properties of the produced test panels. Moreover, the consolidation parameters will also have an effect on the ballistic performance.

Work has also been done in the program for optimizing the consolidation time for different products and increasing the overall production capacity. A new temperature logging unit has been developed to have better control on the temperature during consolidation – both for temperature monitoring of the process and inside the products themselves. A better control of the temperature allows denser stacking of the protective products during each consolidation cycle. The work on obtaining better understanding and optimalization of the production parameters have tripled the production capacity at NFM. Higher production capacity is beneficial for NFM, but also for the Norwegian Armed forces related to preparedness and better access to ballistic protective equipment, if needed in a crisis or war situation.

FFI has many years of experience on research and development of axisymmetric filament-wound composite structures, such as pressure vessels and rocket motors. In this program, new software tools, methods and production set-ups have been investigated and developed at FFI for also including filament-winding of non-axisymmetric complex structures. Examples of non-axisymmetric structures relevant for soldier systems are helmet shells and protective plates.

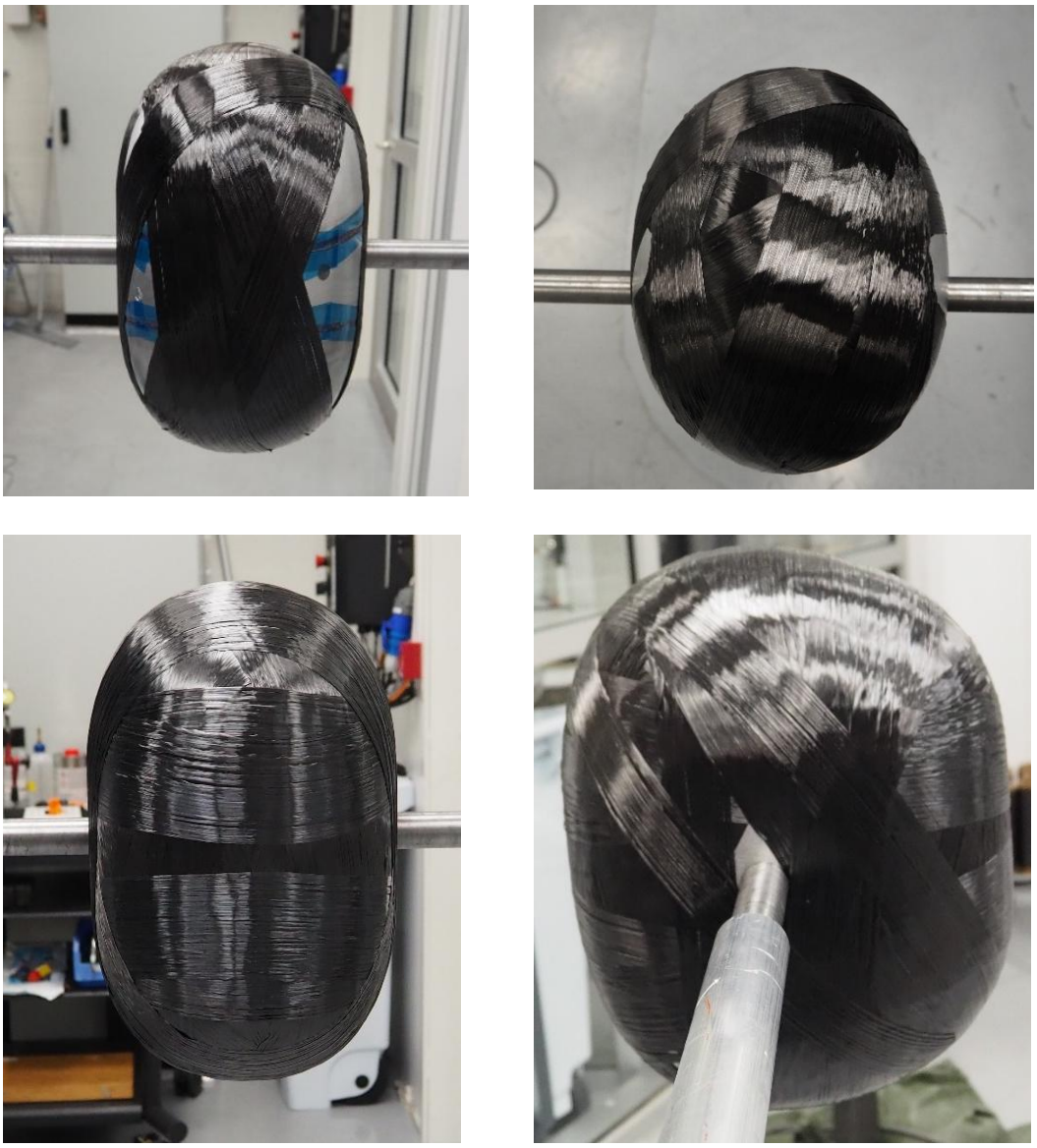

Figure 3: Snap shots of the filament-winding of a helmet structure using a high-performance carbon fibre prepreg material.

Current commercial software tools for filament winding (only) support axisymmetric structures. The new tools developed at FFI include the use of a robotic arm as part of the filament-winding set-up [7]. The robot increases the number of degrees of freedom, which again allows more complex structures to be produced. Software tools

for the movements of a robotic arm have been developed for filament winding of a helmet structure [8]. The mandrel used was 3D printed at FFI. Using this mandrel, two helmet shells can be filament-wound at the same time and then cut apart after curing/consolidation. Several attempts have been made on optimizing the winding angles and the winding pattern to obtain a helmet shell with close to the same shell thickness for the whole structure, as well as with good structural mechanical integrity and good ballistic performance. Figure 3: Snap shots of the filament-winding of a helmet structure using a high-performance carbon fibre prepreg material.

shows snapshots from one of the processes of filament-winding a helmet shell using a high-quality carbon fibre prepreg material. In this case an aerospace-quality carbon fibre prepreg material was used. This is not the most relevant material for ballistic applications, but this still demonstrates the overall process, which will be very similar to winding helmet structures using, e.g., UHMWPE based materials.

The end-result of the filament winding of the carbon fibre helmet, after curing and cutting, is displayed in the left part of Figure 4. Thickness measurements have been made, as shown in the right part of Figure 4, showing that there is some variation, which is not optimal. The production time is also too high for this to be a cost-effective production process. Nevertheless, new competence has been built on producing more complex composite structures using filament winding and high-performance fibre materials, which is highly relevant for the next steps of development.

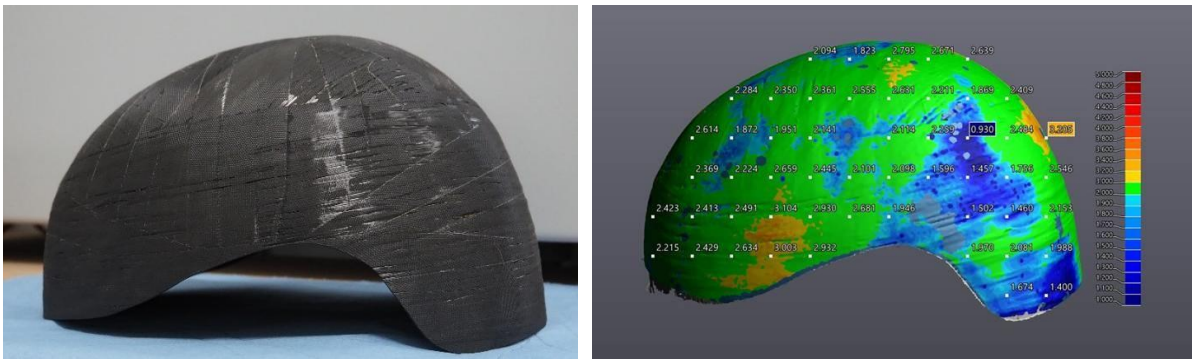

Figure 4: Carbon fibre helmet shell. Left: The helmet shell after curing and cutting. Right: Thickness measurements of the helmet shell.

In addition to the more specific goals of developing ballistic products, the program has also aimed at further developing the more fundamental understanding and knowledge of ballistic protective materials. One important area for the use and maintenance of the ballistic products, is the aging of the materials used in protective systems and the ballistic performance of the equipment over time. Today, the products' lifetime is limited, i.e. the producers typically guarantee 10 years of use before the protective products should be scrapped and replaced. Based on experience from testing after 10 years of in-field use, the products still have the same performance and could be used for more years. Better understanding of material degradation and possible defects due to tear and wear and in-field use, will help deciding what products/components should be scrapped and what products/components could get a life extension.

An aging study on a commercially available ballistic system has been performed in the program [9, 10]. Different test specimens have been produced using NFM's production technology. The test specimens were thereafter put in a climate chambre and exposed to accelerated tests (humidity and temperature). **Feil! Fant ikke referansekilden.** shows the stacking of the test specimens in the climate chambre at FFI. The two sets of test specimens were exposed to different conditions. The first set was exposed to temperature and humidity cycling according to the NIJ 0101.06 hard armour conditioning protocol [11]. Test specimens were taken out from the climate chambre at different stages of the cycling process and tested ballistically. For the second set, the testing was more focused on the ballistic properties after exposure to hot climate conditions (also this set of test specimens were tested ballistically).

As an overall conclusion from this study on accelerated aging of materials, including both sets of test specimens with the different exposure, the applied loads do not significantly degrade the materials, meaning that the protective products can be used for a longer period than the current 10 years.

Figure 5: Accelerated testing, i.e. temperature and humidity cycling, of representative test specimens for personal ballistic protection.

As an overall conclusion, the national research and development program has resulted in new knowledge in the area of next generation personal protective products, as well as better understanding on how to maintain the current systems used by the Norwegian Armed Forces. The program has also identified improvements and new research activities in different areas. First of all, new knowledge has been obtained on materials to be used for filament winding of ballistic products. Future work will look into tape materials, with the same geometry (and stickiness) as the prepregs typically used in axi-symmetric winding applications (such as carbon fibre prepregs). Moreover, the production process at NFM has been improved and more optimized for each material system used in current and future products. Also, the production capacity has been significantly increased due to better understanding of the temperature distribution during consolidation. Finally, major steps have been taken in the development of tools and solutions for more optimal production of helmet shells using filament winding.

The authors would like to acknowledge colleagues at FFI and NFM for their work and contribution to this national research and development program; Bernt B. Johnsen, Tommy Saga, Amalie Grønvold, Tale F. Tungesvik, Sandeep Singh Klair, Dennis B. Rahbek, Geir Skjolden, Bendik A. Sagsveen, Eirik Kristiansen, Terje Glomsaker, Toivo Horvei, Marcin Lewicki, Øyvind S. Søgaard, Terje Mork, Karl Petter Elvestad, Marius Hagen, Jarosław Żynda and Susanne Thomesen.

References

[1] Fibroline, [Online]. Available: https://www.fibroline.com/.

[2] B. Johnsen, T. Thorvaldsen, T. Horvei, T. Glomsaker, M. Lewicki and D. Rahbek, “Novel developments of personal protective equipment made of ultra-high molecular weight polyethylene – materials, production processes and test methods,” Norwegian Defence Reasearch Establishment (FFI), FFI report 21/02424, Exempt from public disclosure, 2021.

[3] A. Grønvold, T. F. Tungesvik, T. Saga, B. B. Johnsen, S. S. Klair, T. Thorvaldsen, T. Glomsaker and T. Horvei, “Filament winding of UHMWPE panels – an investigation of methods, fibre types and matrix systems,” Norwegian Defence Reserach Establishment (FFI), FFI report 24/00482, Exempt from public disclosure, 2024.

[4] A. Grønvold, B. B. Johnsen, T. Saga, T. Thorvaldsen, A. Wien and M. Lewicki, “Filament winding of UHMWPE panels – the effect of uniaxial versus isostatic pressure during consolidation,” Norwegian Defence Research Establishment (FFI), FFI report G-25/034, Exempt from public disclosure, 2025.

[5] A. Grønvold, B. B. Johnsen, T. Saga, T. Thorvaldsen, A. Wien, S. Thomesen, J. Żynda, M. Lewicki and T. Horvei, “High-pressure consolidation of UHWMPE panels – effect of temperature and production method,” Norwegian Defence Reserach Establishment (FFI), FFI report 26/00787, Exempt from public disclosure, 2026.

[6] A. Grønvold, “Characterisation of UHMWPE-based materials by DSC and FT-IR,” Norwegian Defence Research Establishment (FFI), FFI report 25/01543, Exempt from public disclosure, 2025.

[7] T. Thorvaldsen, A. Grønvold, T. F. Tungesvik, T. Saga, B. A. Sagsveen, G. Skjolden, B. B. Johnsen, E. Kristiansen and S. S. Klair, “Robot arm based set-up for filament winding of composite components for personal ballistic protection,” Norwegian Defence Research Establishment (FFI), FFI report 23/00730, Exempt from public disclosure, 2023.

[8] T. Saga, T. Thorvaldsen, A. Grønvold and S. S. Klair, “Filament winding patterns for complex non-axisymmetric geometries - considerations and modelling tools,” Norwegian Defence Research Establishment (FFI). FFI report 25/01529, Exempt from public disclosure, 2025.

[9] B. B. Johnsen, A. Grønvold, M. Lewicki, A. Wien and T. Thorvaldsen, “Accelerated ageing of consolidated UHMWPE materials – effects on mechanical and ballistic performance,” in *5th Workshop on ageing effects in protective systems, components*, Saint-Louis, France, 20-21 May 2025.

[10] B. B. Johnsen, A. Grønvold, M. Lewicki, A. Wien and T. Thorvaldsen, “Accelerated ageing of consolidated UHMWPE materials – effects on mechanical and ballistic performance,” Norwegian Defence Research Establishment (FFI), FFI report 26/00610, Exempt from public disclosure, 2026.

[11] U.S. Department of Justice, “Ballistic Resistance of Body Armor - NIJ Standard-0101.06,” 2008.

Light-Weight Armour for Defence & Security
LWAG 2026

Experimental and Numerical Investigation of Ballistic Impact Response in Multilayer Metallic Systems Using FE–SPH Analyses with Various Damage Criteria

Hande Vural[a], Yunus Emre Ozsoy[a], Tuncay Yalçinkaya[a]*

[a]*Department of Aerospace Engineering, Middle East Technical University, 06800 Ankara, Türkiye*

Extended Abstract

Designing protective structures that are both ballistically effective and as lightweight and thin as possible remains a major challenge in armor engineering. Multilayer configurations offer a promising approach in this respect, since they not only provide the potential to improve ballistic performance by combining different material properties within a single system, but also offer practical advantages in service, such as the easier replacement of a damaged layer after impact. In particular, combining materials with different mechanical characteristics can enhance ballistic resistance by benefiting from their complementary contributions in hardness, strength, and energy absorption.

To investigate this problem, ballistic impact experiments are first performed for selected Al6061-T6 and Ti-6Al-4V target configurations. In this context, 500 × 500 mm² plates are tested with a 7.62 × 51 mm AP projectile, and each shot is recorded using a high-speed camera to determine the residual velocity, which is calculated using the open-source Tracker software. In parallel, quasi-static displacement-controlled tensile tests are conducted to characterize the mechanical response of these materials. For Ti-6Al-4V, smooth tensile specimens are used, whereas for Al6061-T6 different specimen geometries are considered. During the tensile tests, high-speed images are processed by digital image correlation (DIC) using the open-source NCORR software to obtain deformation fields and the corresponding force–displacement curves. For both materials, the JC plasticity parameters A, B, and n are identified from the smooth-specimen force–displacement curves, while the strain-rate and temperature-dependent parameters are taken from the literature [1,2]. These parameters are then validated in Abaqus through numerical tensile-test simulations. The CL and other single-parameter damage models are calibrated using the same smooth-specimen force–displacement data by accumulating the incremental damage terms up to the experimentally observed fracture point, from which the critical damage parameters are obtained. To expand the material set, Al7075-T651, Weldox 700E, and Armox 500T are also considered, and their constitutive parameters and material models are calibrated and validated using available tensile-test data [3–5].

The numerical analyses are performed in Abaqus/Explicit. The MJC plasticity model is used for Al7075-T651 and Weldox 700E, whereas the JC plasticity model is adopted for Al6061-T6, Ti-6Al-4V, and Armox 500T. The plasticity models are introduced through VUHARD, while the damage models are implemented through VUSDFLD. For the ballistic impact FE model, mesh convergence studies are carried out for three different projectile nose shapes. Since the blunt projectile exhibits the highest sensitivity to mesh size, a common mesh configuration is selected for all projectile types. Contact algorithms and friction coefficients are then determined through comparisons with the experimental impact results. All contacts are defined using a penalty formulation; friction is considered between the projectile and the plate, whereas no friction is introduced between the target layers. For the SPH analyses, the strain threshold and bulk viscosity parameters are also selected by comparison with the experiments, and the energy balance is monitored for all cases. For Al7075-T651, Weldox 700E, and Armox 500T, the ballistic impact FE models are further assessed and validated, as presented in our previous studies [6–8], through comparison with experimental data reported in the literature [9–11]. The validated material models are then used in monolithic and multilayer targets with different stacking sequences under equal-weight and equal-thickness conditions, as summarized in Table 1.

* Corresponding author. Tel.: +90-312-210-4258
E-mail address: yalcinka@metu.edu.tr

Table 1: Target configurations analysed in this study and their corresponding total weight and total thickness values.

Configuration	Total Weight (kg)	Total Thickness (mm)
Al6061-T6 (Single / Double)	5/10	7.5/15
Al7075-T651 (Single / Double)	5/10	7.5/15
Ti-6Al-4V (Single / Double)	5.5/11	5/10
Weldox 700E/ Armox 500T (Single / Double) (SW)	5.5/11	2.8/5.6
Weldox 700E/ Armox 500T (Single / Double) (ST)	9.8/19.6	5/10
Al6061-T6/ Al7075-T651 - Ti-6Al-4V (Front / Back)	10.5	15
Weldox 700E/ Armox 500T - Al6061-T6 (SW)	10.5	10.3
Weldox 700E/ Armox 500T - Al6061-T6 (ST)	14.8	15

Figure 1 presents the experimental, FE, and SPH residual velocity–impact velocity curves for single and double-layer Al6061-T6 and Ti-6Al-4V targets. In the single-layer cases, the FE model provides very good agreement with the experiments for both materials, whereas the SPH analyses tend to predict lower ballistic limits. In the double-layer configuration, the FE model continues to predict the Al6061-T6 response accurately, but for Ti-6Al-4V it underestimates the ballistic resistance compared to the experiments. For both materials, the SPH results are generally less accurate than the FE results in the double-layer cases and show larger deviations from the experimental behavior.

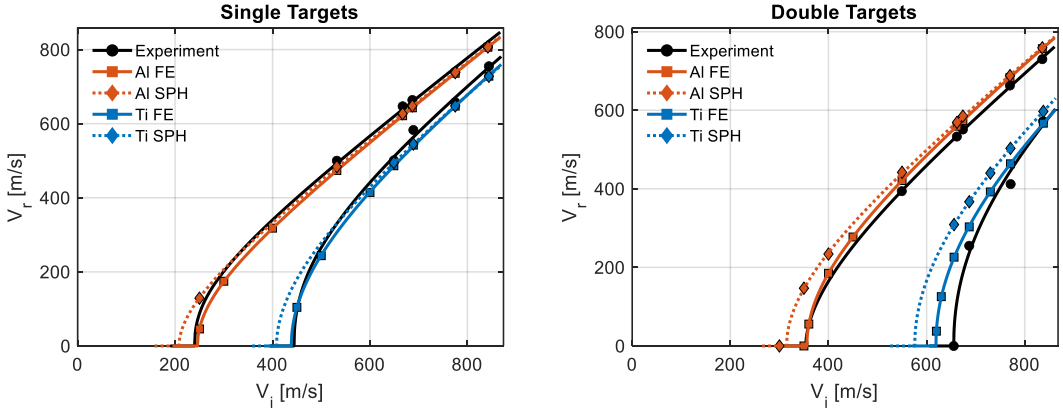

Figure 1: Experimental, FE, and SPH residual velocity–impact velocity curves for single and double Al6061-T6 and Ti-6Al-4V.

Figure 2 shows that FE and SPH predictions are in relatively good agreement with the experiments when Al6061-T6 is used as the front plate. However, when Ti-6Al-4V is placed in the front layer, both numerical approaches deviate significantly from the experimental response. This difference is thought to be related to the rigid projectile assumption used in the simulations. In multilayer targets, projectile deformability may strongly affect the interaction between the two layers, especially because the separation of the jacket and core after perforation of the first layer can modify the effective mass and impact condition on the second layer. The results indicate that this effect is more pronounced for titanium-front configurations than for aluminum-front configurations.

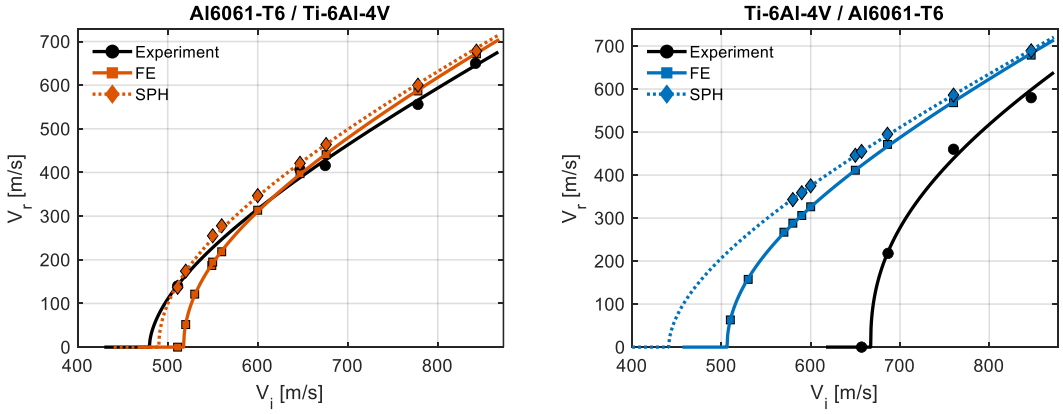

Figure 2: Experimental, FE, and SPH residual velocity–impact velocity curves for the hybrid target configurations.

Figure 3 compares the ballistic limit values predicted by different uncoupled damage models for aluminum and titanium targets under ogival and blunt projectile impact conditions. For the ogival case, the predicted values are compared with the experimental ballistic limits, whereas for the blunt case, the comparison is made with the average FE-based ballistic limit values, since no experimental data are available. The results indicate that the predictions are more consistent in the ogival case, while the blunt case shows a wider scatter and stronger sensitivity to the selected damage model. Among the investigated models, Freudenthal and Le Roy (LR) models appear to be less suitable for ballistic impact applications, as they deviate more significantly from the reference values, particularly under blunt impact conditions. It is also observed that aluminum exhibits a stronger sensitivity to damage model selection, whereas titanium shows a comparatively more stable response. The present results will also be compared with directly Lode-dependent damage models, such as the Modified Mohr–Coulomb (MMC) and Hosford–Coulomb (HC) models, in order to further evaluate the predictive capabilities of different damage formulations.

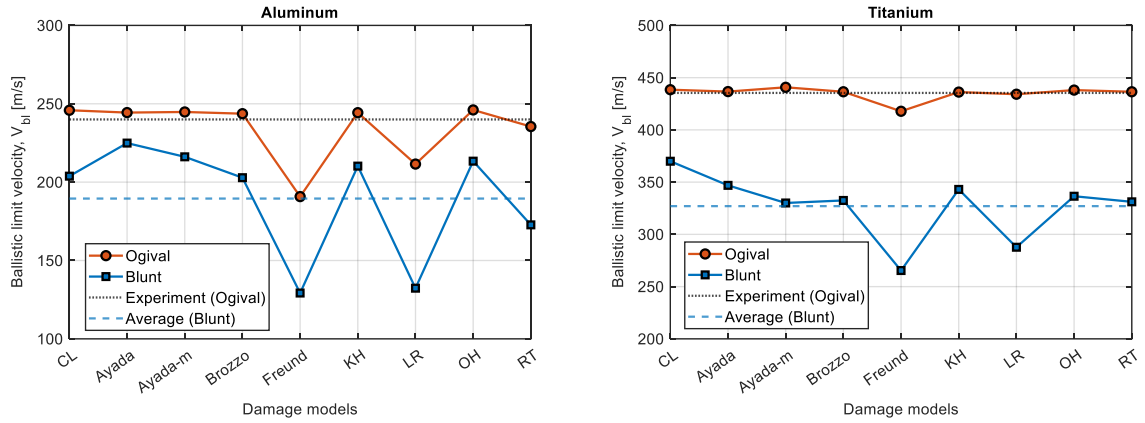

Figure 3: Comparison of ballistic limit velocity values predicted by different uncoupled damage models for aluminum and titanium targets under ogival and blunt projectile impact conditions.

To extend the study beyond the experimentally tested materials, additional analyses are conducted for different metallic target configurations. As shown in Figure 4, two aluminum alloys are investigated in single and double-layer targets, as well as in hybrid arrangements with titanium placed at the front or back. The results show that the Al7075-T651 single-layer target provides nearly the same ballistic resistance as the Al6061-T6 double-layer target, indicating a more weight-efficient solution. A similar trend is also observed in the hybrid configurations. Although Al7075-T651 is more sensitive to stacking sequence than Al6061-T6, the configuration with Al7075-T651 in the front and Ti-6Al-4V in the back shows the highest energy absorption among the considered hybrid cases. Overall, replacing Al6061-T6 with Al7075-T651 appears advantageous in terms of ballistic efficiency and structural weight.

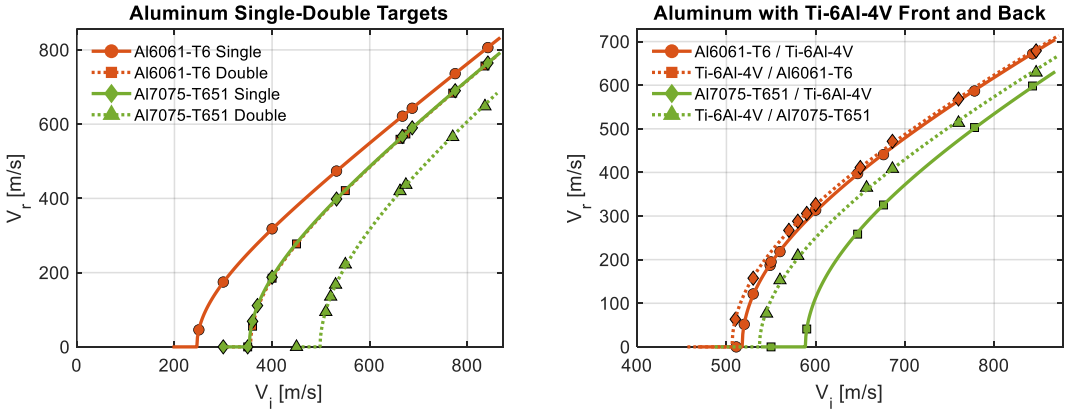

Figure 4: Residual velocity–impact velocity curves for aluminum targets in single- double and hybrid configurations.

Figure 5 compares the residual velocity–impact velocity responses of Ti-6Al-4V, Weldox 700E, and Armox 500T under same-weight and same-thickness conditions for both single and double-layer targets. Under same-weight conditions, Ti-6Al-4V shows a favorable ballistic response in both configurations. Armox 500T exhibits a resistance

close to that of titanium and may also offer a practical advantage due to its lower total thickness. Under same-thickness conditions, however, Armox 500T becomes clearly more resistant than the other materials. One of the most notable observations is the comparatively low ballistic resistance of Weldox 700E, which remains significantly below that of both Ti-6Al-4V and Armox 500T under both same-weight and same-thickness conditions.

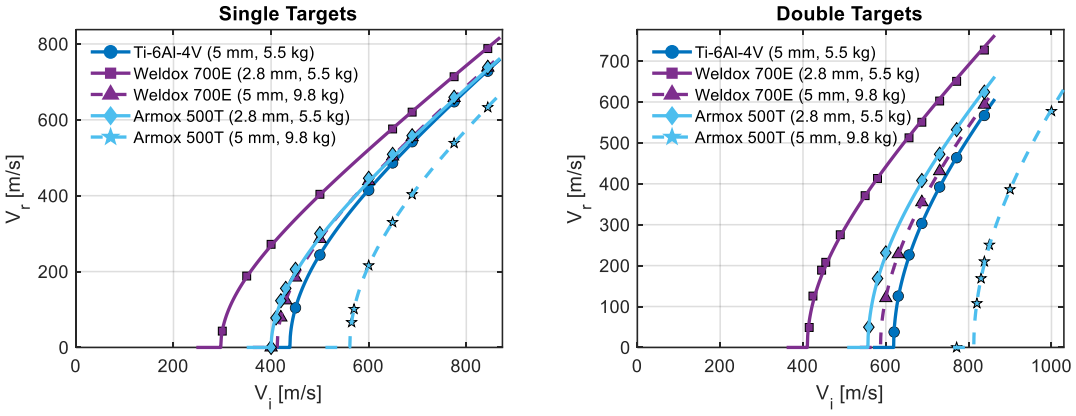

Figure 5: Residual velocity–impact velocity curves for same-weight and same-thickness single and double targets.

Overall, the results demonstrate that the ballistic response of multilayer metallic systems is highly sensitive to material combination, stacking sequence, and design constraint. The numerical analyses show that FE modeling provides a reliable predictive framework, while deviations in some hybrid cases highlight the importance of projectile representation and multi-layer interaction. Al7075-T651, Ti-6Al-4V, and Armox 500T emerge as promising materials for lightweight, impact-resistant structures.

References

[1] Daoud, M., Jomaa, W., Chatelain, J. F., & Bouzid, A. (2015). A machining-based methodology to identify material constitutive law for finite element simulation. The International Journal of Advanced Manufacturing Technology, 77(9), 2019-2033.

[2] Wu, S., Zhou, C., Shi, Y., Hu, A., & Xiao, X. (2023). Plasticity, ductile fracture and ballistic impact behavior of Ti-6Al-4V Alloy. International Journal of Impact Engineering, 174, 104493.

[3] Popławski, A., Kędzierski, P., & Morka, A. (2020). Identification of Armox 500T steel failure properties in the modeling of perforation problems. Materials & Design, 190, 108536.

[4] Dey, S. A., Børvik, T., Hopperstad, O. S., Leinum, J. R., & Langseth, M. (2004). The effect of target strength on the perforation of steel plates using three different projectile nose shapes. International Journal of Impact Engineering, 30(8-9), 1005-1038.

[5] Børvik, T., Hopperstad, O. S., & Pedersen, K. O. (2010). Quasi-brittle fracture during structural impact of AA7075-T651 aluminium plates. International journal of impact engineering, 37(5), 537-551.

[6] Göçmen, Y., Erdogan, C., & Yalçinkaya, T. (2023). A numerical ballistic performance investigation of Armox 500T steel through ductile damage models. Engineering Fracture Mechanics, 292, 109658.

[7] Vural, H., Tekbaş, S., Gökdemir, N., & Yalçinkaya, T. (2025). A numerical study of the ballistic performance of multi-layered targets through uncoupled damage models. Procedia Structural Integrity, 68, 573-580.

[8] Ozsoy, Y., Vural, H., & Yalçinkaya, T. Comparison of FE and SPH analyses for predicting the ballistic impact response of Weldox 700E, to be submitted.

[9] Iqbal, M. A., Senthil, K., Sharma, P., & Gupta, N. K. (2016). An investigation of the constitutive behavior of Armox 500T steel and armor piercing incendiary projectile material. International Journal of Impact Engineering, 96, 146-164.

[10] Dey, S., Børvik, T., Teng, X., Wierzbicki, T., & Hopperstad, O. S. (2007). On the ballistic resistance of double-layered steel plates: An experimental and numerical investigation. International journal of solids and structures, 44(20), 6701-6723.

[11] Forrestal, M. J., Børvik, T., & Warren, T. L. (2010). Perforation of 7075-T651 aluminum armor plates with 7.62 mm APM2 bullets. Experimental Mechanics, 50(8), 1245-1251.

Acknowledgment

The authors would like to thank Fatma Taşgın for her valuable assistance with the ballistic impact experiments.

Light-Weight Armour for Defence & Security
LWAG 2026

DIC determination of localised loading on blast loaded plates from coarse soils

R. Waddoups[a,b]*, S.D. Clarke[a,b], R.J. Curry[a], T. Lodge[a,b], A. Hibbert[a,b]

[a] *University of Sheffield, School of Mechanical, Aerospace and Civil Engineering, Sir Frederick Mappin Building, Sheffield, S1 3JD, UK*
[b] *Blastech Ltd., The Innovation Centre, 217 Portobello, S1 4DP, UK*

Abstract

Buried charges pose a serious threat to nearby people and structures. An increased understanding of the loading from buried charges allows for the design of improved protective measures. To this end, results from buried blast testing in uniform sand, well-graded sandy gravel and uniform gravel were compared to establish the effect that large discrete particles have on the delivery of loading across a plate. All tests were conducted with fully saturated soils. The data indicates that the inclusion of large individual particles within the soil matrix leads to localised increases in loading, however the overall peak displacement was similar across soil types. Inspecting the development of velocity uptake across the plate demonstrated markedly different loading behaviours between the uniform sand and the soils containing coarser gravel particles. For lightweight armour systems this distribution of loading could have a profound impact on the protective capacities of the system.

Introduction

The threat from buried charges (landmines, or explosive remnants of war (ERW)) is pervasive in regions of present and past conflict across the world. “At least 6,279 casualties of landmines and ERW were recorded” in 2024, across “52 countries and areas”, 90% of which were civilians [1]. Loading from these buried charges can be devastating for structures in the vicinity. It is well established that buried charge loading varies considerably according to the geotechnical properties of the soil in which it is situated [2,3], with testing previously conducted across scales. It was previously suggested that localisations of specific impulse were introduced from testing with well-graded soils (such as the STANAG sandy gravel according to AEP-55 [4]) due to discrete particles striking a measurement surface with high individual momentum [5,6].

Methodology

The current work has utilised high-speed digital image correlation (DIC) at 210,000 frames per second to determine the deformation of 4 mm thick S275 mild steel plates under buried charge loading. The setup uses 78 g PE4 charges for a quarter-scale version of the methodology described in AEP-55 [4]. This geometric setup was utilised to recreate the same loading conditions as used previously when recording pressure-time histories at discrete locations with Hopkinson pressure bars housed in a rigid plate [7]. The deformation of the plate, and the uptake of velocity across the recorded plate surface, was used to establish a high-fidelity spatial distribution of the loading.

Two Photron SA-Z high-speed video (HSV) cameras, with matching 50mm lenses, were positioned on a support structure suspended above the loaded plate, which was clamped between two 20mm thick mild steel clamp frames with an exposed circular area of 315mm diameter. The clamp frame bore on an effectively rigid reaction frame via a 50mm thick mild steel ‘adapter plate’, which allows for a reduction in the scale of testing from previous work with 995mm square plates [8] to the 450mm square plates used in this work. This setup is shown in Figure 1.

The plates were sand-blasted and a white spray paint applied, overlaid by a black speckle pattern for the DIC process. Before testing, the system was calibrated using approximately 30 pairs of images of a known calibration target board in various orientations. Images were recorded at a resolution of 384 x 160 pixels during the period of

* Corresponding author.
E-mail address: rwaddoups1@sheffield.ac.uk

loading, covering a field of view (FOV) of approximately 230 x 100mm. The plate was illuminated using two GS Vitec MX LED lights.

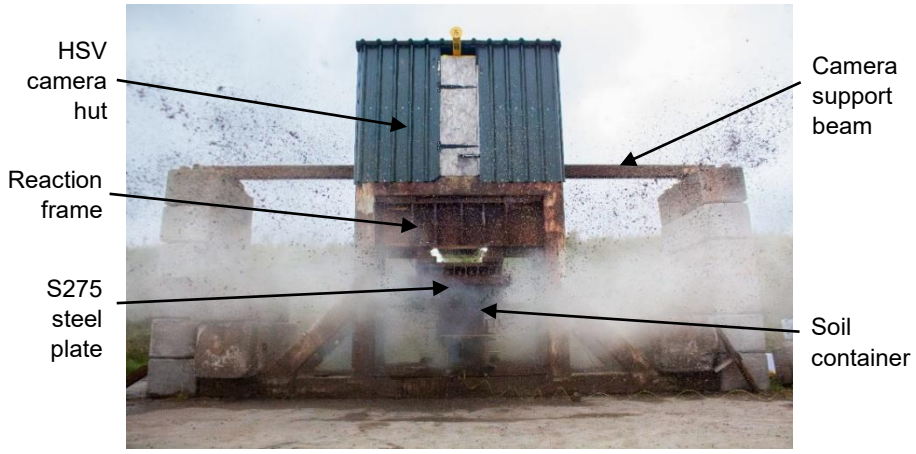

Figure 1: Experimental apparatus during a test

3:1 cylindrical charges (57mm diameter, 19mm height) in 3D-printed open-topped cases were positioned at a depth of burial of 28mm and a stand-off distance of 140mm from the soil surface to the plate, as shown in Figure 2(a). Soil type was varied between uniform Leighton Buzzard (LB) sand, 'Stanag' sandy gravel (an approximation of that specified by AEP-55 [4]), and uniform 'pea' gravel, each fully saturated via a bottom-up saturation technique [9]. Charge excavation and burial in each soil type is shown in Figure 3, after which the overburden was replaced, soil saturated, and the soil container placed in position on the test apparatus.

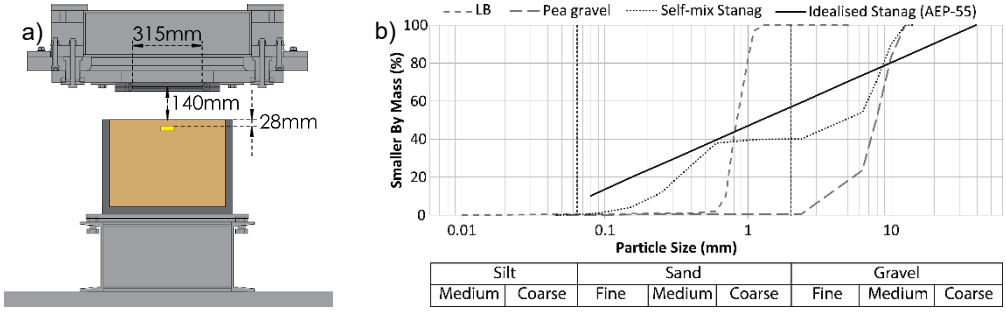

Figure 2: (a) Charge, soil and plate geometry diagram; (b) particle size distributions of soils used in this work

Figure 3: Charge burial in: (a) Uniform LB sand, (b) 'Stanag' sandy gravel, (c) uniform pea gravel

Results and Discussion

A surface of plate displacement data can be derived from the DIC process, as shown in Figure 4. From this, time-histories can be extracted at individual points, or full-field data can be examined.

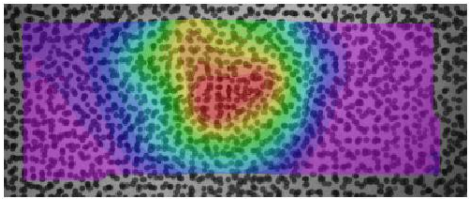

Figure 4: Camera FOV with displacement data surface overlaid

Plate displacement

Taken along the central axis of the measured points, Figure 5 shows the plate displacement from one test in each soil type, with data extracted at 0.1ms intervals. From this, it can be seen that each of the soils resulted in similar deflection behaviour, but with some localised bulging in the plate for the Stanag and gravel tests.

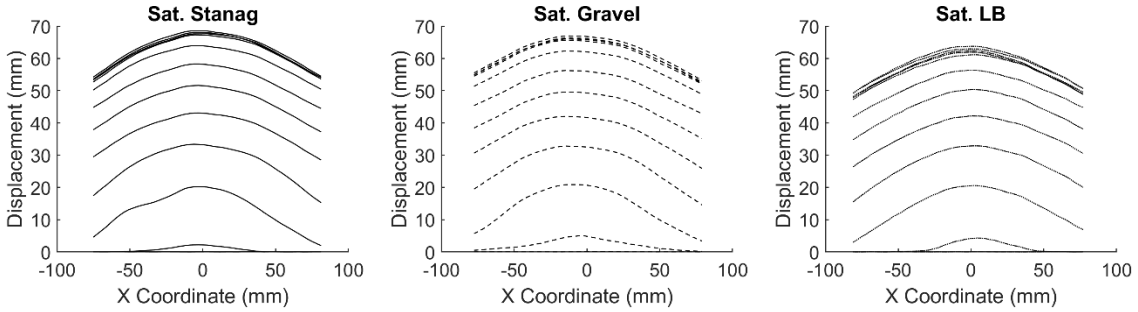

Figure 5: Plate deflection line-slices along X axis

Plate velocity

From the DIC-determined plate displacement, velocity was determined as the derivative with respect to time. As plate thickness and material were maintained between all tests, and given that specific impulse can be determined as the momentum per unit area under impulsive conditions [10-12], plate velocity can be used to characterise the loading impinging on the plate. Figure 6(a) shows the development of velocity for each of the tests, wherein it can be seen that the uniform LB resulted in a reasonably uniform distribution of velocity, which propagated radially from a centrally loaded point. In contrast, the plates exposed to soils containing larger gravel particles underwent non-uniform loading with discrete areas of increased velocity occurring at different times during the loading period.

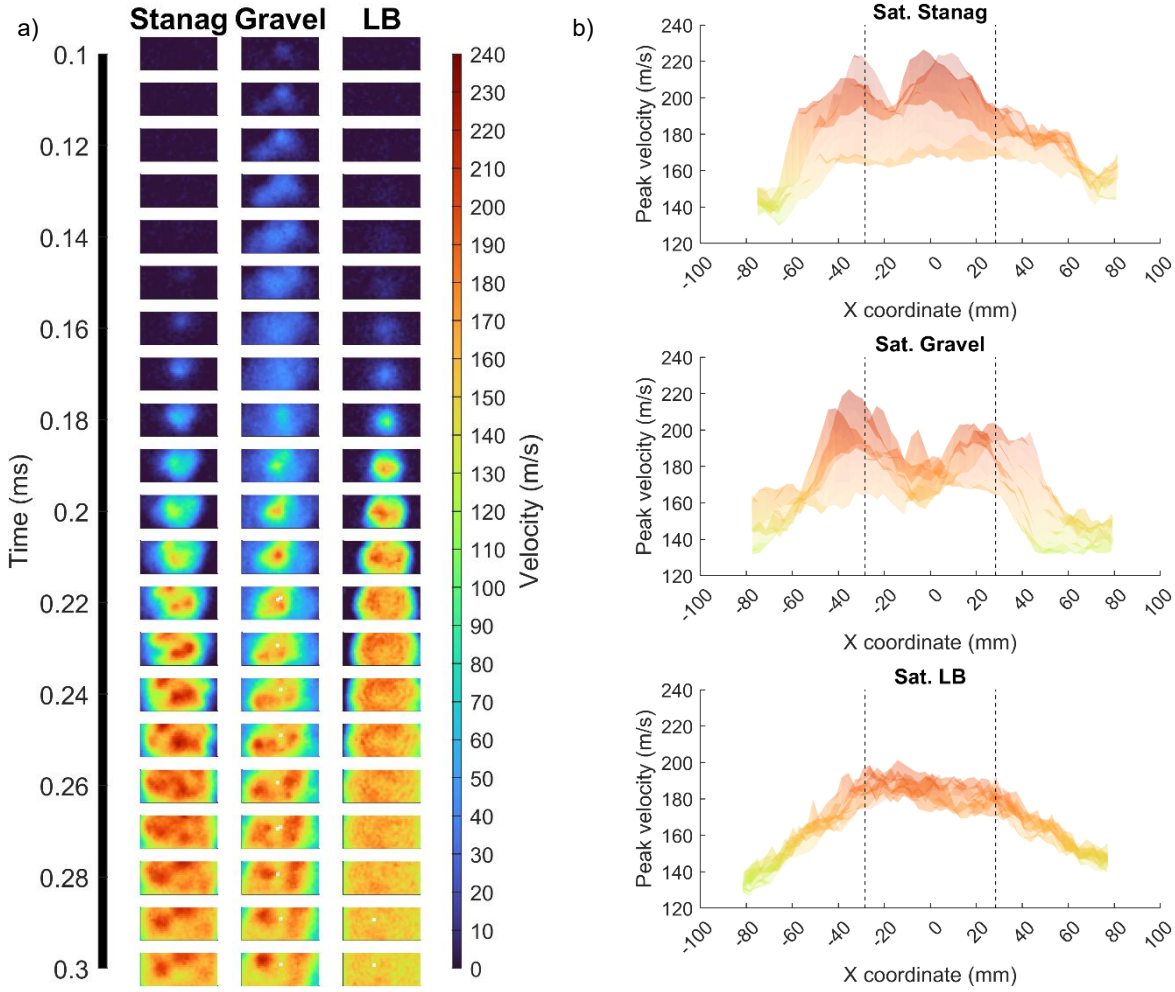

Figure 6: (a) Development of velocity across the plate surface for each test; (b) Peak plate velocity across the surface

Figure 6(b) shows the peak velocity across the measured area of the plate surface for the three soils (surface plots viewed side-on), demonstrating the non-uniformity of the loading sustained by structures exposed to blasts from charges buried in coarse soils containing large particles. It can be seen that the uniform LB sand resulted in a relatively uniform loading across the region directly above the charge (with the charge diameter indicated by the dashed lines), with reductions in loading at positions away from this zone. Small, localised variations in the LB data are anticipated to result primarily from noise in the image-based processing method. On the other hand, large peaks and troughs in velocity can be seen in the Stanag and gravel data of around 20% of the velocity magnitude. Discrete strikes from gravel particles (with a D_{50} of 8mm in this work) can be seen to contribute to significant localised increases in loading due to high-momentum individual impacts.

Conclusion

Buried charge blast testing has been undertaken at a quarter-scale of that prescribed by AEP-55 [4], using saturated soils of varying particle size distribution, to determine the effect of large discrete particles in a soil matrix on loading distribution. High-speed DIC was used to determine the displacement of mild steel plates under this loading, with the velocity distribution used to understand variations in loading between soil types. It was shown that buried charges in soils containing larger gravel particles resulted in more variable loading across the plate surface, with localised increases in velocity on the order of 20%. On the other hand, uniform sand resulted in a smooth distribution of loading across the plate. This has significant implications for the design of lightweight armour systems.

References

[1] International Campaign to Ban Landmines. (2025). Landmine Monitor 2025. www.the-monitor.org.

[2] Clarke, S. D., Fay, S. D., Warren, J. A., Tyas, A., Rigby, S. E., Reay, J. J., Livesey, R., & Elgy, I. (2015). Geotechnical causes for variations in output measured from shallow buried charges. International Journal of Impact Engineering, 86, 274–283. https://doi.org/10.1016/j.ijimpeng.2015.08.009

[3] Clarke, S. D., Fay, S. D., Warren, J. A., Tyas, A., Rigby, S. E., Reay, J. J., Livesey, R., & Elgy, I. (2017). Predicting the role of geotechnical parameters on the output from shallow buried explosives. International Journal of Impact Engineering, 102, 117–128. https://doi.org/10.1016/j.ijimpeng.2016.12.006

[4] NATO. (2011). AEP-55, Volume 2 (Edition 2). PROCEDURES FOR EVALUATING THE PROTECTION LEVEL OF ARMOURED VEHICLES - MINE THREAT.

[5] Rigby, S. E., Fay, S. D., Tyas, A., Clarke, S. D., Reay, J. J., Warren, J. A., Gant, M., & Elgy, I. (2018). Influence of particle size distribution on the blast pressure profile from explosives buried in saturated soils. Shock Waves, 28(3), 613–626. https://doi.org/10.1007/s00193-017-0727-7

[6] Waddoups, R., Clarke, S., Tyas, A., Rigby, S., Gant, M., & Elgy, I. (2023). An Approach to Quantifying the Influence of Particle Size Distribution on Buried Blast Loading. Eng, 4(1), 319–340. https://doi.org/10.3390/eng4010020

[7] Clarke, S., Rigby, S., Fay, S., Barr, A., Tyas, A., Gant, M., & Elgy, I. (2020). Characterisation of buried blast loading. Proceedings of the Royal Society A: Mathematical, Physical and Engineering Sciences, 476(2236). https://doi.org/10.1098/rspa.2019.0791

[8] Elgy, I. D., Clarke, S. D., Fuller, B. J., Barr, A. D., Armstrong, D. W., Gant, M. T. A., Keirl, J. J., Porter, G. C. E., Softly, I. D., & Tyas, A. (2021). Deformation of Armox 440T plates subject to buried explosive charge detonations: A benchmark for appliqué systems. International Journal of Impact Engineering, 150. https://doi.org/10.1016/j.ijimpeng.2021.103819

[9] Clarke, S. D., Fay, S. D., Tyas, A., Warren, J., Rigby, S., Elgy, I., & Livesey, R. (2014, September). Repeatability of buried charge testing. Proceedings of the 23rd International Symposium on Military Aspects of Blast and Shock. http://eprints.whiterose.ac.uk/80754/

[10] Tetlow, L., Rigby, S. E., Langdon, G. S., Curry, R. J., & Pezzola, G. (2026). Experimental characterisation of near-field blast loading using digital image correlation on thin plates. *International Journal of Impact Engineering*, *213*. https://doi.org/10.1016/j.ijimpeng.2026.105671

[11] Curry, R. J., Langdon, G. S., & Tyas, A. (2025). Steel Plates Subjected to Localised Blast Loading: Transient Measurements Using Ultra-High-Speed Camera Technology. Strain, 61(6). https://doi.org/10.1111/str.70019

[12] Rigby, S. E., Tyas, A., Curry, R. J., & Langdon, G. S. (2019). Experimental Measurement of Specific Impulse Distribution and Transient Deformation of Plates Subjected to Near-Field Explosive Blasts. Experimental Mechanics, 59(2), 163–178. https://doi.org/10.1007/s11340-018-00438-3

Light-Weight Armour for Defence & Security
LWAG 2026

Introduction of the Bundeswehr “Competence Centre for Ballistic Body Armour”

WEISSE, Marina[a]1, Dr. GROBERT, Steffen[b], Dr. BERTHELSEN, Rolf[c]

[a]*Bundeswehr Innovation Centre InnoZBw, Wartenberger Str. 25, Erding, 85435, Germany*
[b]*Bundeswehr Office for Defence Planning, Oberspreestr. 61, Berlin, 12439, Germany*
[c]*Bundeswehr Technical Center for Weapons and Ammunition WTD 91, Schiessplatz,Meppen, 49716, Germany*

Extended Abstract

Introduction

The global security situation is changing radically and rapidly, and threat scenarios are evolving. These challenges necessitate immediate action for focused and comprehensive technological development and innovation, both generally and specifically in the field of ballistic personal protection. In response to increasing challenges and the need for interdisciplinary research, in 2025 the Bundeswehr has established a new, cross-cutting research group – the Competence Centre for Ballistic Body Armour (German abbrev: KompSt BKS). The KompSt BKS has been embedded within the Bundeswehr Innovation Lab as a part of the Bundeswehr Innovation Centre [1]. Further members are the Technical Centre for Weapons and Ammunition, and the Bundeswehr Office for Defence Planning, that provides scientific and organizational advisory support.

Innovation Centre Infrastructure and Functions

The Bundeswehr Innovation Centre serves as a central hub situated between internal user requirements and external innovation partners. On one side, it connects users, requirement owners, international partners, and Bundeswehr universities. On the other, it links with industry, start-ups, and R&D. In the centre, three main functions operate: Marketplace (central point of contact, operational picture, and multinational network), Technology Development & Validation (coordinating research with in-house labs, including ballistic body protection), and Innovation Scouting (technology campaigns to jointly test, validate, and find solutions) (Figure *1*) [2]. Located at the former Erding air base—rapidly transformed into an innovation hub with a test area including obstacle course and open areas, which are highly relevant for example for comparing wearing tests. On-site, multiple labs support these functions: the Soldier Innovation Lab which includes the Research Groups for Personal Armour, Soldier Systems and Ergonomics; an Unmanned Systems & Robotics Lab and the Advanced Manufacturing Lab. This physical presence ensures that technology must be experienced hands-on, with real users in real environments, compressing the cycle from promise to proof.

* Corresponding author. Tel.: +49 8122 9590 2301
E-mail address: marinaweisse@bundeswehr.org

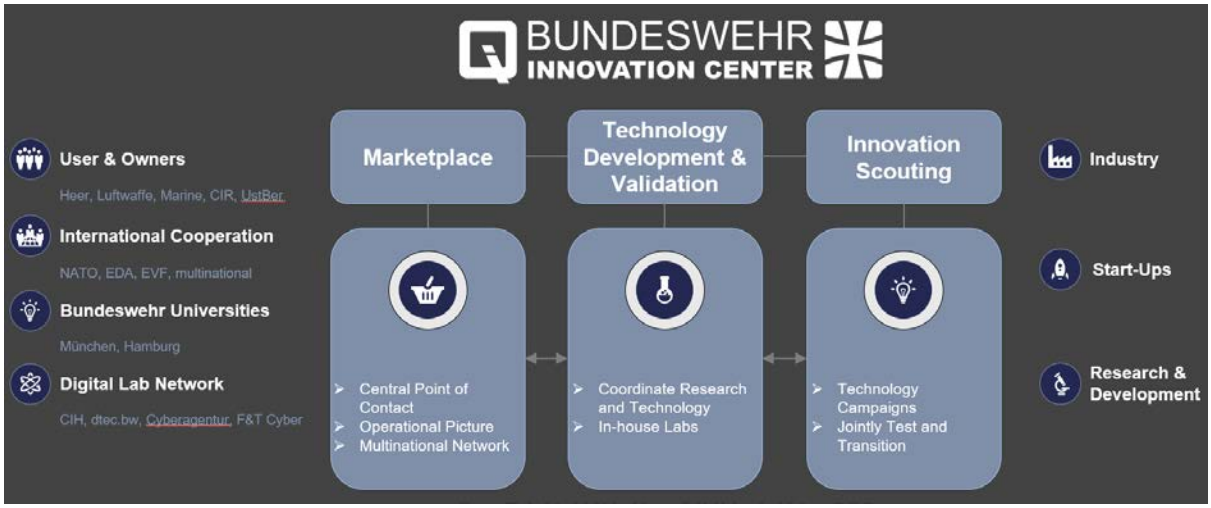

Figure 1: Bundeswehr Innovation Center: Main functions

Challenges and Context

Current ballistic protection systems face significant operational constraints. From the perspective of military personnel, existing systems are often heavy, bulky, limit mobility, contribute to overheating and discomfort, and alter natural movement biomechanics, which may increase the risk of injury [3]. Furthermore, lessons from ongoing conflicts highlight that injury patterns are changing due to a war primarily conducted with drones. An increase in injuries to the extremities in addition to those on the torso and vital organs [4], as well as fragmentation and blast as the primary causes of casualties, are observed. However, many systems remain optimized for traditional ballistic rifle threats [5]. The concept of integrated survivability emphasizes that while a system may reduce injury probability from impact, it may also increase vulnerability to detection or engagement if not balanced correctly [3].

Objectives and Methods of the Competence Centre for Ballistic Body Armour (KompSt BKS)

The KompSt BKS consolidates key capabilities for ensuring and further developing the protection of soldiers. Therefore, the primary objective is to include the coordination and execution of interdisciplinary defence technology research. The group and its research focus on the following areas and aim to demonstrate the skills required for the following tasks:

• Coordination and execution of interdisciplinary defence technology research in the fields of ballistics, materials engineering, and biomechanics for short-term dynamic processes
• Development and updating of independent testing guidelines
• Analysis of threat scenarios using operational evaluations to derive requirements for ballistic body armour
• Conducting ballistic tests and scientific investigations on ballistic body armour components with continuous, short-term availability

Results and Expected Outcomes

Early internal assessments indicate improved cross-unit coordination, reduced redundancy in planning processes, and increased collaborative activity in research strategy. As part of the 1st scientific workshop on Ballistic Body Protection, organized by the KompSt BKS in March of this year, the expert discussions on current threat scenarios and innovative approaches to addressing future challenges regarding necessary protection levels, simultaneously with high requirements for mobility and modularity as well as realistic testing methods of protective equipment, showed that the field of Ballistic Body Protection must be addressed even more strongly within the framework of Defence Technology Research and Technology. The integration of KompSt BKS within the Innovation Centre enables the armed forces to adapt to new ideas and technologies and offers an innovation ecosystem of civil-military research cooperation. The KompSt BKS provides advisory functions for end users to support strategic armament decisions regarding ballistic body protection.

Conclusion and Outlook

The introduction of KompSt BKS represents a strategic investment in an interoperable research environment. As the group matures, its contributions are expected to enhance translational efficiency and strengthen interdisciplinary discovery. Expected outcomes include the development of injury risk analysis tools for behind armour blunt trauma (BABT) of head and body using measurement technology and finite element methods.
Furthermore, in response to changing contact definitions involving artillery or FPVs, fragments or glide bombs, as well as the increased need for a high range of motion, prioritization of research topics will change towards: more flexible soft armour for the most vulnerable surfaces and fragment arrival angles; lighter body protection modules for head and body, right-sized dimensions for light weight helmets and vests, based on actual body measurements and shapes which were systematically recorded through serial measurements of German soldiers [6], and with realistic and modular fragment performance; test methods that reflect in a more realistic way what actually impacts the human body on the battlefield.

References

[1] R. d. Bundeswehr, “www.bundeswehr.de,” Redaktion der Bundeswehr, 2026. [Online]. Available: https://www.bundeswehr.de/de/auftrag/ressourcen/bildung-forschung-bundeswehr/innovationslandschaft. [Accessed 22 04 2026].

[2] R. d. Bundeswehr, “www.bundeswehr.de,” Redaktion der Bundeswehr, 2026. [Online]. Available: https://www.bundeswehr.de/de/organisation/ausruestung-baainbw/struktur/innozbw. [Accessed 22 04 2026].

[3] G. o. Canada, “www.canada.ca,” Government of Canada, 03 12 2024. [Online]. Available: https://www.canada.ca/en/department-national-defence/programs/defence-ideas/element/competitive-projects/challenges/lightweight-ballistic-protection.html. [Accessed 22 04 2026].

[4] M. Tomelzik and U. Henning, “https://ynside.extranet-bw.de/,” Bundesministerium der Verteidigung, 27 04 2026. [Online]. Available: https://ynside.extranet-bw.de/de/organisation/unterstuetzungsbereich/aktuelles-aus-dem-unterstuetzungsbereich/kriegsverletzungen-fokus-chirurgie-6096196. [Accessed 05 05 2026].

[5] J. Ganor, “www.bodyarmornews.com,” BodyArmorNews.com, [Online]. Available: https://www.bodyarmornews.com/the-body-armor-of-the-war-in-ukraine-iii-personal-and-squad-level-armor-adaptations-and-lessons-learned/?web=1. [Accessed 22 04 2026].

[6] N. Kubsch, “www.bundeswehr.de,” 03 02 2022. [Online]. Available: https://www.bundeswehr.de/de/organisation/marine/aktuelles/3d-bodyscan-fuer-bekleidung-und-ausruestung-5338304.

FORSVARSBYGG

Vi bygger forsvarsevne hver dag

NTNU

Norwegian University of Science and Technology

Forsvarsbygg, Norwegian Defence Estates Agency is a governmental organ under the Ministry of Defence. We develop, build and operate property for the defence sector.

Postboks 405 sentrum
0103 OSLO
Telephone: +47 468 70 400